Determination of Cap Model Parameters using Numerical Optimization Method for Powder Compaction

Cong Lu
Marquette University

DETERMINATION OF CAP MODEL PARAMETERS
USING NUMERICAL OPTIMIZATION METHOD
FOR POWDER COMPACTION

by

Cong Lu

A Dissertation submitted to the Faculty of the Graduate School,
Marquette University,
in Partial Fulfillment of the Requirements for
the Degree of Doctor of Philosophy

Milwaukee, Wisconsin

August 2010

ABSTRACT
DETERMINATION OF CAP MODEL PARAMETERS
USING NUMERICAL OPTIMIZATION METHOD
FOR POWDER COMPACTION

Cong Lu

Marquette University, 2010

Many advantages are inherent to the successful powder metallurgy (P/M) process especially in high volume manufacturing. The strength/density distribution of the compacted product is crucial to overall success. The finite element analysis (FEA) method has become an effective way to numerically simulate strength/density distribution in a P/M compact. The modified Drucker-Prager cap (DPC) model has been shown to be a suitable constitutive relationship for metal powder compaction simulation. The calibration of the modified DPC model involves a procedure known as a triaxial compression test. Equipment for completing a triaxial compression test on metal powders is neither readily available nor standardized in the P/M industry. A robust calibration procedure that requires only simple experimental tests would increase the usability of the simulation procedure. This research created a universal cost/time-effective calibration method to accurately determine all parameters of a modified DPC model by using a combination of numerical simulation methods, numerical optimization methods and common material testing techniques. The use of the triaxial compression test is eliminated and the new method relies only upon conventional compaction equipment, standard geometry and readily available metallographic techniques. The DPC parameters were determined by applying the proposed method on ferrous powders. The predicted DPC parameters were verified on a compressed product with complex geometry.

ACKNOWLEDGMENTS

Cong Lu

This dissertation can not be completed without the support of many people. My first gratitude must go to my academic advisor, Dr. James Rice. His vision, advice, and encouragement allow me to achieve my doctorial degree. I would also show my sincere thanks to my committee, Dr. Kyuil Kim, Dr. Raymond Fournelle, Dr. Joseph Domblesky, and Dr. Vikram Cariapa for their guidance. Special thanks go to the Department of Mechanical Engineering, and Graduate School, Marquette University for their support. I would also like to acknowledge my wife, Shuang Jia, our children, Cynthia and Benjamin, and my parents, Huijiang Lu and Xiue Liu, for their love, understanding, and support. Nothing in a simple paragraph can express my love for you.

TABLE OF CONTENTS

LIST OF TABLES

LIST OF FIGURES

Chapter 1   INTRODUCTION

1.1   Introduction

The process of metal powder consolidation under pressure and subsequent heat treatment to bond the consolidated particles together is known as powder metallurgy (P/M). One particularly common form of the P/M process for producing structural parts is known as press and sintering. In the press and sinter process, powders are uniaxially compressed by punches in a closed die to produce a net or near net shaped product. After the compact is ejected from the die, it is subsequently sintered at a temperature sufficient to produce diffusion bonding among the compressed particles.

Many advantages are inherent to the successful P/M process especially in high volume manufacturing. The elimination of machining steps, the elimination of scrap, the ability to hold repeatable tolerances, and the ability to blend unique material compositions are but a few. These advantages have been utilized by the automotive industry, which consumes approximately 70% of the ferrous P/M powder products.

The advantages unique to P/M are seen only when the process is well understood. Knowledge of the powder characteristics, consolidation process and tooling design as well as sintering mechanisms is necessary to insure success. Engineering models for these areas are needed as producers push for enhanced performance, increased design complexity and economic advantages. In particular, the prediction of the strength

distribution (density) of the compacted product is crucial to overall success. Achieving a desired uniform density throughout a powder compact is desirable in order to eliminate distortions that may otherwise occur during sintering and secondary operations, such as drilling, grinding, repressing, and heat treatments. Uniform density also promotes uniformity in the mechanical properties of the finished part. In the press and sinter process, uniform density can never be completely achieved due to the friction associated with the die and punches. Designed manipulation of the die and punches however, can result in uniform density gradients within a compact, resulting in predictable behavior during sintering.

The finite element analysis (FEA) method has become an effective way to numerically simulate the strength (density) distribution in a P/M compact. Stress-strain relationships have been postulated to account for the various stages of the uniaxial compaction process (powder rearrangement, powder consolidation and bulk deformation) that depend upon the properties of the powder as well as the friction associated with the die and punches. The modified Drucker-Prager cap (DPC) model has been shown to be a suitable constitutive relationship for metal powder compaction simulation by FEA.

The DPC relationship models densification, hardening, as well as interparticle friction during the compaction process. Eight DPC parameters must be identified for any powder, die combination. Several of these parameters require difficult and costly experimental apparatus and procedures not readily available to industry. The ability for wide spread use of engineering design simulation with constitutive models, such as the DPC, would

help enhance the competitiveness of the P/M industry by predicting the internal structure of green parts, consequently improving the part quality.

1.2 Problem Statement

Simulating the powder densification process during P/M compaction via FEA is difficult due to the complexity associated with the underlying constitutive models. The Drucker-Prager cap model has been shown to model all stages of the compaction process but must be calibrated for each material system under investigation. The calibration involves a procedure known as a triaxial compression test. Equipment for completing a triaxial test on metal powders is neither readily available nor standardized. A robust calibration procedure that requires only simple experimental tests would increase the usability of the simulation procedure. Difficulties in the current DPC calibration process can be summarized as:

1. Of the eight material parameters used in the DPC cap model, the shape parameter R, and the transition parameter α, are found through completion of a triaxial compression test. Due to the inability and cost of facilities to provide such a test, these parameters are unknown for the vast majority of materials.

2. The P/M process provides a flexible environment for utilizing specially blended material systems. Prediction of material behavior during consolidation should be accomplished prior to the design of tooling systems or subsequent sintering process design. The complexity of current calibration procedures makes this impossible.

3. No standard procedure or apparatus for calibration has been defined. All model parameter calibration to date has been for laboratory use. Industrial models utilize only relative information for depicting density distributions.

In summary, while the DPC model may be used to accurately simulate the powder compaction process, it must be calibrated for each material system that is to be predicted. Few materials to date have been documented due to the extensive experimental procedures that are needed. The practicality of using FEA for prediction of the density distribution of a compacted powder product has not seen extensive industrial use. A procedure for the rapid calibration of the DPC model will provide P/M engineers reliable design information that has a clear economic impact.

1.3 Research Goals

The purpose of this research is to create a universal cost/time-effective method to accurately determine all parameters of a modified Drucker-Prager cap model by using a combination of numerical optimization methods and common material testing techniques. The calibration of the DPC model should rely only upon conventional compaction equipment, standard geometry and readily available metallographic techniques. The use of the triaxial test will be eliminated. The calibration should be only a function of material properties and should be transferable to other compaction geometries.

1.4 Organization of Thesis

The entire thesis contains 5 chapters. Each chapter focuses on one topic. In this chapter (Chapter 1), the research was outlined. In Chapter 2, the basic background knowledge of constitutive models for porous material and parameter calibration techniques for the cap model will be discussed, such as the modified Drucker-Prager cap model, current standard methods to determine the cap parameters, and numerical optimization algorithms. Chapter 3 will describe the details of the proposed method to determine the parameters and will demonstrate the proposed method with ferrous powders. In Chapter 4 the independency of the predicted parameters to the geometry will validated. At the end of this thesis, Chapter 5 will present conclusions, contributions, and future work.

Chapter 2   BACKGROUND REVIEW

2.1   Metal Powder Compaction

2.1.1   Powder Metallurgy Overview

Powder Metallurgy (P/M) is an ideal process to manufacture many complex mechanical components. This process can produce net or near-net shape parts with complicated geometries that are difficult to produce by conventional machining approaches. Powder composed of a variety of metal and non-metal constituents is consolidated in a die under pressure. The powder particles are bonded together by mechanical interlocking and cold welding then are removed from the die. The compression force experienced by the powder during the forming process will dictate the green density, which is the density of compact and controls the amount of shrinkage the powder compact will undergo during the further process. The process continues with the application of heat to provide a mechanism for diffusion of the powder particles into an interconnected matrix.

Often, one powder compaction process replaces two or more conventional machining processes. This advantage reduces set-up time, inventory and manufacturing costs. Some typical P/M products (produced by powder compaction) are shown below.

Figure 1 P/M Products

Powder metallurgy component industry (P/M) is a relatively young industry

(approximately 60 years old). Since the 1980's, P/M has matured and has been growing

fast. The industry has demonstrated that often P/M parts have the capacity to meet the

needs of manufacturers at much lower cost, compared with castings, forgings, and

machined parts. Bernard Williams, editor director of International Powder Metallurgy

Directory (IPMD), presented the P/M industry as a global industry exceeding $20 billion

in sales annually

(http://www.ipmd.net/editorial/?sid=ZalnQq8w1zwZDlUjBNEjw1sKbIVZoRZE,

Website Retrieved on Jan. 14, 2005,).

According to an updated report from Business Communications Company, Inc. RGB-

041Y Powder Metallurgy (www.bccresearch.com/advmat/GB041Y.html, Website

Retrieved on Jan. 29, 2005,), the North American P/M parts market was estimated at 993

million pounds, worth $5.4 billion in 2003 and is forecast to reach nearly 1.3 billion

pounds, worth about $7.7 billion in 2008. The data from Metal Powder Industries

Federation (MPIF) also shows the production of ferrous powders almost doubled from

1992 to 2004.

Table 1 North American Metal Powders and P/M Parts Shipments

	2003		2008		AAGR% (based on Lbs.) 2003-2008
	Million Lbs.	Million Dollars	Million Lbs.	Million Dollars	
Metal Powders	1,138.84	2,435.14	1,446.0	3,425.26	5.0
P/M Parts	993.38	5,440.53	1,263.07	7,646.15	5.0
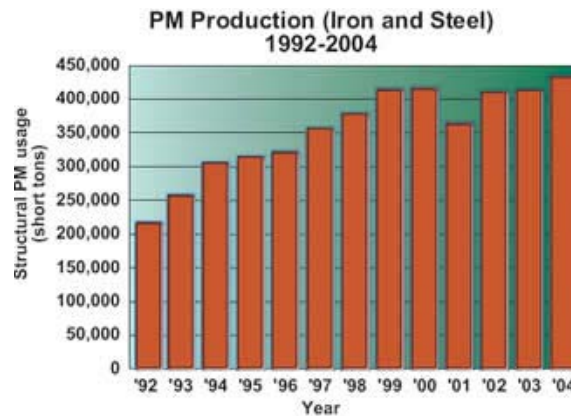
Figure 2 P/M Production from 1992 to 2004

The automotive industry is an important customer of P/M accounting for roughly

70% of all P/M parts sales. A typical U.S. automobile contains about 39 lb. of P/M parts

(http://www.ipmd.net/editorial/?sid=ZalnQq8w1zwZDlUjBNEjw1sKbIVZoRZE,

Website Retrieved on Jan. 14, 2005). The P/M industry is positioned to focus technology

on narrowing the gap between P/M parts and those made from solid material, which

features a greater density/strength, more isotropic material properties, and a higher fatigue resistance.

2.1.2   P/M Processes

The P/M process can be cataloged into three steps: blending, compaction, and sintering. Sometimes, secondary processing such as sizing for tolerance may also be needed.

Blending precisely weighed base powders, lubricants, and alloys to a desired specification, results in a homogenous blend of powder material that can be compacted into part shapes. Filling a die cavity with a predetermined amount of blended powder, then compressing the material between two or more punches is known as traditional closed die compaction. This setup yields a green compact that is relatively fragile with powder particles that have been distorted as they have been compressed. Sintering is the process of using "high-temperature" furnaces to bond the metal particles together under the protection of a controlled atmosphere. Typical sintering temperatures for most ferrous and non-ferrous alloys vary from 1450°F to 2100°F. Sintering transforms the compacted mechanical bonds between the powder particles into metallurgical solid-grain bonds. It is the sintering that provides the green part the primary metallurgical properties. Also, during sintering, distortion in the compressed compact is relieved, as the part is held for some time at a temperature sufficient to allow diffusion activity among the particles. Areas of the compact with non-uniform density often become distorted during the

sintering operation. This is caused by the variation of the capillary force and the solid-grain bounding force due to densification. The capillary force is isotropically orientated therefore causes uniform shrinkage and holds grains together to preserve the component shape in the early stage of sintering. The capillary force decreases as voids become extinct. Thereafter, the solid-grain bonding provides compact rigidity/strength and resists distortion.

Secondary processes may be performed after sintering if the functional requirement of the parts demands them. These secondary processes include closed die sizing, CNC machining, turning, heat treating, stream treating, oil or resin impregnation, vibratory deburring, and plating, etc.

2.1.3 Powder Compaction

Metal powder compaction is one of the most cost effective processes of P/M manufacturing. The conventional compaction method is uniaxial pressing, which is carried out by a mechanical method, a hydraulic method, or a combination of the two. This type of conventional compaction plays an important role in industry due to the low cost it offers. Using a set of tools, which typically have an initial cost less than $20,000, millions of near-net shape products can be produced.

In engineering applications, one of requirements is to achieve a uniform powder density with no internal crack formation in green compacts. This requirement is also critical for

stable dimensional change during the sintering process. Any non-uniform density gradients and cracks during compaction need to be minimized or eliminated. This is one of fundamentals to allow an unacceptable level of distortion and shrinkage of the green compacts in further procedures.

Conventional uniaxial compaction is performed with forces applied along one axis. The procedure for powder compaction includes powder filling, pressing, and ejection. The following graph illustrates the tool motion during a compaction cycle. Current press technology can provide up to 10 separate axial motion controls to produce compacts with significant geometric complexity (Groover 2001). Multiple motions allow a variation of compression force and compression ratio and deliver a finer control of densification to obtain a more uniform compact density.
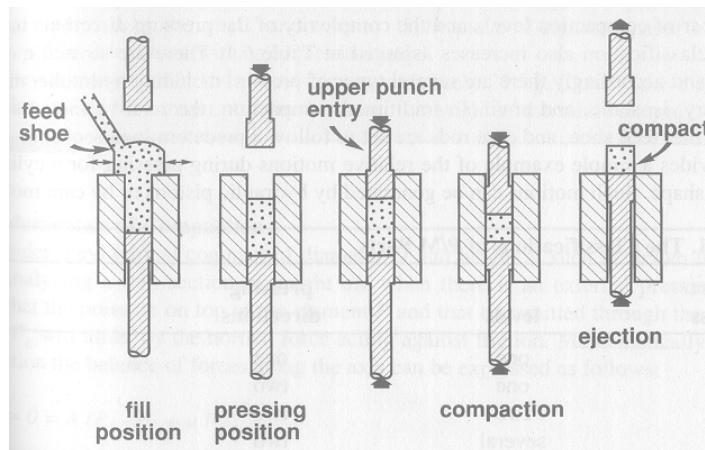
Figure 3 Compaction Cycle

The process with pressure applied from both the top and bottom punches is termed double-action pressing, while the process with pressure applied from one punch is called single-action pressing. The work piece after pressing is called a green compact. In a

similar manner, the density of the compact is termed the green density, which is much

greater than the initial density of the loose powder in the die. The strength of the green

compact must be adequate for handling but is much less than will be achieved after

sintering. Double-action pressing produces a more symmetric density distribution about

the part center than single-action pressing due to the balanced frictional forces on the

compact (German 1997).
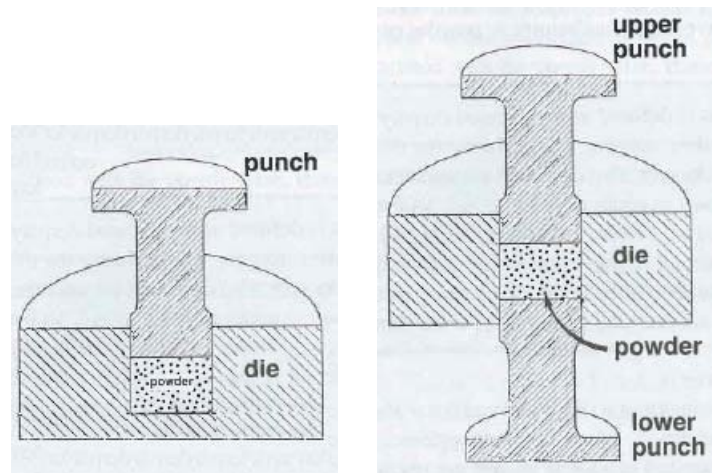
Figure 4 Single-action Pressing vs. Dual-action Pressing

After compaction, the final part must be ejected from the die. The force pushing the

compact out of the die is called the ejection force. Lubrication added to the initial powder

helps decrease the ejection force. Without lubrication, the elastic energy stored in the

compact due to compression will push the part against the die wall and cause significant

friction during ejection. The friction force impacts densification of powders at surfaces of

compacts and could cause a steep density change locally. Many kinds of lubricants are

used in powder compaction, such as graphite, ethylene bis stearamide (EBS), and wax,

etc. The most widely used lubricants are those based on stearic acid which consists of

CH_3-$(CH_2)_{16}$-CO_2H. Lubricants reduce the density of a green compact and must be

removed prior to sintering. In practice, a balance of lubricant is used which reduces die wall friction, minimizes radial load, and maximizes green properties.

Metals commonly used in the powder forming process include iron, steel, nickel, copper, aluminum, and titanium. Refractory metals include tungsten, molybdenum and tantalum. Bronze, brass, stainless steel and nickel cobalt alloys.

2.1.4 Fundamental Equations of Powder Compaction

Consider a cylindrical compact of diameter D and height H drawn in the following figure, P is the pressure on the top, P_b is the pressure transmitted to the bottom, F_n is the normal force, u is the coefficient of friction between the powder and the die wall, A is the cross section area, F_f is the friction force, and z is the axial to radial pressure distribution, which actually changes with the compact density. Thus,

$$\sum F = 0 = A(P_b - P) + uF_n \qquad \text{Equation 1}$$

$$F_n = \pi z P D dH \qquad \text{Equation 2}$$

$$F_f = \pi u z P D dH \qquad \text{Equation 3}$$
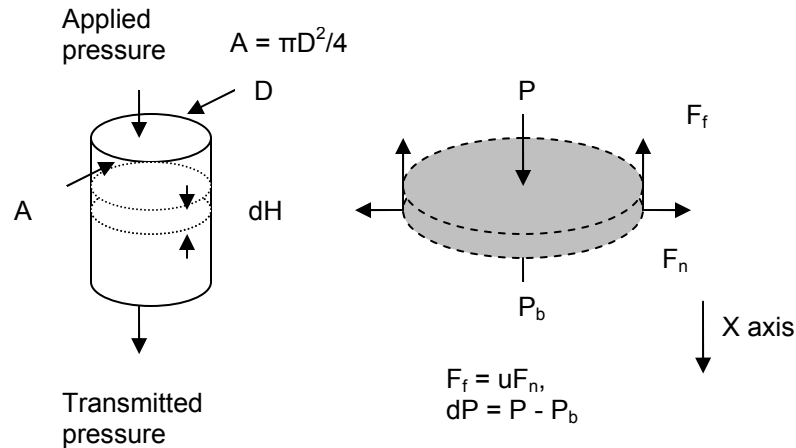
Figure 5 Illustration of a Cylindrical Compact

Substitute Equation 3 into Equation 1, $dP = P - P_b = -4uzPdH / D$, integration of the pressure term with respect to the height gives the pressure at any position x below the punch:

$$P_x = P \exp(- 4uzx / D) \qquad \text{Equation 4}$$

Equation 4 describes single action compaction. For double-action compaction, this equation is valid too, but the distance x is the distance to the nearest punch according to literature (German 1997). In either case, the pressure decreases with the ratio of the compact height to the diameter of punch.

The average compaction stress depends on the geometry (H/D), the axial to radial pressure distribution (z), and the friction coefficient between powders and die walls (u). The average compaction stress can be estimated as

$$\sigma = \begin{cases} P[1 - 2uz(H / D)] & \sin gle - action \\ P[1 - uz(H / D)] & double - action \end{cases} \qquad \text{Equation 5}$$

The ratio uzH/D is a gauge of die pressing. Better pressing performance is obtained when this ratio is small. Another important factor is the height to diameter ratio. Generally, when the height to diameter ratio exceeds 5, the compaction will be unsuccessful (German 1997).

2.1.5 Compaction Stages

It is common to describe compaction as a three-stage procedure (Heckel 1961; Donachie and Burr 1963; James 1977, Fischmeister and Arzt 1983). The first stage is "rearrangement" without plastic deformation under low pressure. The densification associated with this stage is a few percent for ductile powders with relatively smooth shapes (Fischmeister and Arzt 1983). Under an intermediate pressure, the next stage is "homogeneous deformation". In this stage, the overall densification is increased. Plastic deformation increases simultaneously with a diminishing amount of sliding (also called "non-radial particle motion") until friction, plastic deformation, and cold welding, lock the particles into a rigid arrangement. As the compaction pressure increases, the relative volume of particles undergoing plastic deformation increases. At low pressures, the powder plastic flow is localized to particle contacts, while at higher pressures the plastic flow spreads from the contacts into the entire particle. Further densification can be only caused by plastic deformation (Fischmeister et al. 1978). In the final stage, as the compact approaches full density, more and more powder contacts impinge under high pressure, making the powder harder to compress. At the end of this stage, the particle

shape can be considered approximately as a tetrakaidekahedron (German 1997,

Fischmeister et al. 1978). The onset of these 3 stages depends on the yielding

characteristics of the powder and the friction between the powder and the die walls

(Gethin et al. 1994). Thus, a constitutive model that is able to represent all 3 compaction

stages correctly will have advantages for numerically predicting the density distribution

of a powder compaction product.
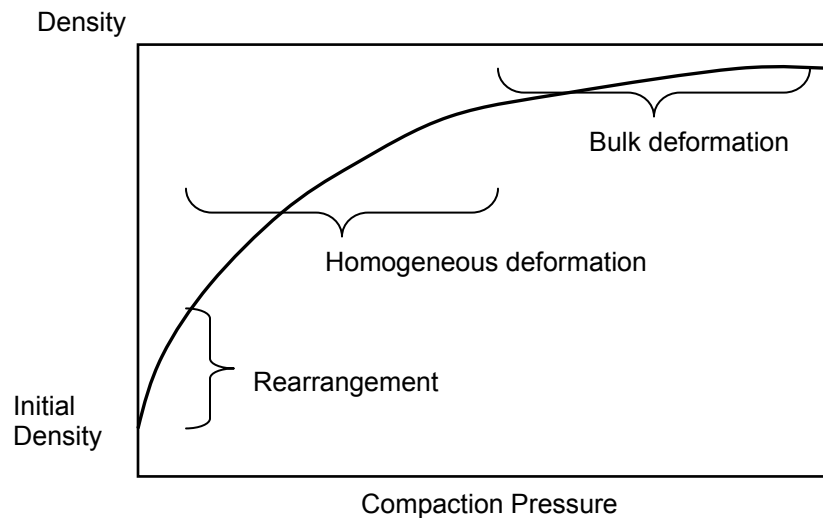
Figure 6 Stages of Compaction

2.1.6   Densification Behavior

The densification behavior of porous metal powders is the critical factor in the

numerical simulation of the powder compaction procedure. It depends upon a number of

powder characteristics such as response to plastic deformation, surface hardness, work

hardness, and adhesion of the particles. As can be seen in Figure 6, as density is increased

through packing of the particles, work hardening and plastic deformation of the compact

cause an exponential increase in the pressure for continued density increases. The three major process parameters that determine the density distribution can be classified as:

1. The means of force delivery onto the powder;

2. Mechanical constraints;

3. The rate of pressurization.

At the macro-mechanical modeling level, the use of soil mechanics models (i.e. the cap model) have gained considerable attention (Sandler and Rubin 1979, Crawford and Lindskog 1983; Aravas 1987; Chtourou et al. 2002). A cap model is developed as a multi-surface elastoplasticity model to present both powder densification and hardening behavior and requires a significant amount of experimental work to calibrate. By utilizing a constitutive law for metal powders with an appropriate calibration procedure, the finite element analysis method can be used as an effective design tool to numerically simulate the density distribution in green parts.

2.2   Constitutive Models

Two types of macro-mechanical model are generally used in the P/M industry to simulate densification behavior during the powder compaction process using the finite element analysis method: the "classical elastoplasticity model" ("Kuhn-Shima" model) and the "soil mechanics" (Drucker-Prager) model.

2.2.1   Classical Elastoplasticity Models

The first group of models (Kuhn and Downey 1971; Shima and Oyane 1976; Gurson 1977; Weber and Brown 1989, Fleck et al. 1992) were originally developed as an extension of the classical J_2-flow theory to the compressible powder range. The older models were shown not to be appropriate for modeling the early stage of compaction where the density is low (Brown and Abou-Chedid 1993). Most of the earlier models were developed on sintered powders. However, the loose powders behave more like a granular material. This resulted the need to modify the old models. Researchers (Koopman et al. 1992; Shima and Saleh 1993, Tszeng and Wu, 1995) modified the model to represent the shear behavior at low density levels by accommodating interpartical friction. The model have a general form,

$$f(\sigma,\rho,k) = A(\rho)\mathrm{I}_1^2 + B(\rho)J_2 - C(\rho)k^2 \qquad \text{Equation 6}$$

where, A, B, and C are functions of the actual medium density ρ, I_1 is the first invariant of the stress tensor, J_2 is the second invariant of the deviatoric stress tensor and k is a state variable representing the hardening effect.

2.2.2   Soil Mechanics Models

"Soil mechanics" models (Sandler and Rubin 1979, Crawford and Lindskog 1983; Aravas 1987) were originally used for rocks and soils. Researchers adopted a number of models for powder densification such as the Cam-clay model and the cap model. The cap model is one of the most popular "soil mechanics" models used in the P/M area (Watson and Wert 1993, Guillot et al. 1995; Kwon et al. 1997; Sun et al. 1999; Kim et al. 2000;

Lee and Kim 2002; Chtourou et al. 2002). Due to the feature of the multi-surface

elastoplasticity, a cap model presents the densification and hardening as well as inter-

particle friction. The description and numerical details of a cap model will be found in

section 2.2.3. This type of model has the flexibility to model all compaction stages and

has been adopted to simulate the compaction of ductile powders. However, the

experimental work is very significant in order to properly calibrate the model parameters

for a given material.

A comparison of the above two types of constitutive laws can be found in the

literature. Lee and Kim examined the following six models on Al powders (Lee and Kim

2002). In Figure 7, a) is the experiment result, b) is a proposed model result by Lee and

Kim, c) is Kuhn-Shima model, d) is Fleck-Gurson model, e) is Cam-clay model, and f) is

the Drucker-Prager cap model. Lee and Kim concluded that the Kuhn-Shima model

underestimates the density distribution in the lower density region, while the cap model

underestimates the experimental data in the higher density zone.
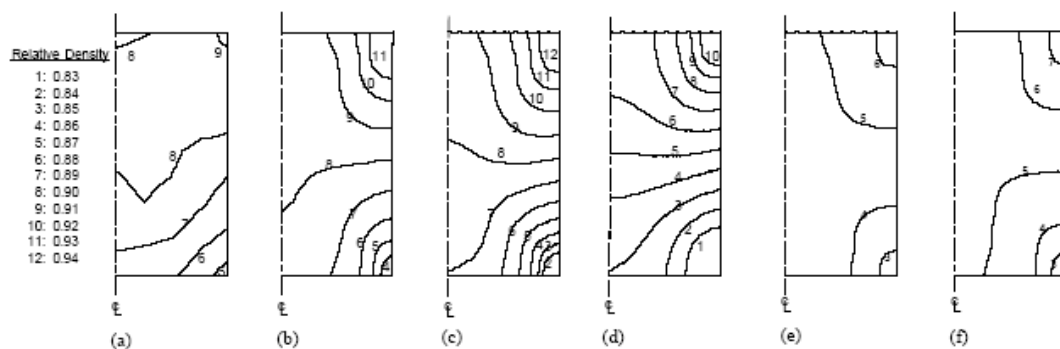
Figure 7 Comparison between experimental data and FEM calculations

The European consortium PM MODNET (PM MODNET 1999) compared the Cam-Clay model and the modified Drucker-Prager cap model with an atomized iron-based powder. An axi-symmetric hub shaped part was used, and the experimental data of density and tooling forces during die compaction were examined. PM MODNET concluded that the numerical simulation with the modified Drucker-Prager cap model showed a better performance in the prediction of the density, while the Cam-Clay model showed a better performance in the prediction of the tooling force.

Based upon the above background study, the modified Drucker-Prager cap model will be adopted in this research to predict the densification behavior of metal powders during compaction by using the finite element analysis method.

2.2.3 Modified Drucker-Prager Cap Model

Drucker and Prager formulated a plasticity model for granular materials in 1952 (Drucker and Prager, 1952). The modified Drucker-Prager cap model is an advancement of the original model by adding a cap shaped yield surface to the shear yield surface to present the initiation of plastic volumetric strains. Drucker et al. started to introduce the cap (Drucker et al., 1957) in 1957 and the work by Resende and Martin (Resende and Martin, 1985) finalized the formulation of the Drucker-Prager cap model where loadings can occur in both the shear failure surface and the cap.

A modified Drucker-Prager cap model (Figure 8) represents the behavior of a material undergoing permanent deformation (Bažant 1985, ABAQUS 2003). It consists of three parts: a linear shear failure surface showing increasing shear stress with increasing mean stress; a curved "cap" intersecting both the shear failure surface and the mean stress axis; and a transition surface allowing a smooth intersection between the cap and failure surfaces. The equations defining these three surfaces in the equivalent pressure stress– deviatoric stress plane (p-q plane) can be obtained as (Bažant 1985, ABAQUS 2003):

1. Shear failure surface F_s,

$$F_s = q - p \tan \beta - d = 0 \qquad \text{Equation 7}$$

   where q is the deviatoric stress measure, or Von Mises equivalent stress, p is hydrostatic pressure stress, d is the material cohesion, and β is the angle of friction.

2. Compression cap F_c,

$$F_c = \sqrt{(p - p_a)^2 + \left(\frac{Rq}{1 + \alpha - \alpha / \cos \beta}\right)^2} - R(d + p_a \tan \beta) = 0 \qquad \text{Equation 8}$$

   where R is the ratio of the horizontal axis of the elliptical cap to the vertical axis of the elliptical cap, α is a numerical parameter defining a smooth transition yield intersection between the cap and failure surfaces, and p_a is an evolution parameter for volumetric plastic, strain-driven hardening/softening of the cap.

3. Transition surface F_t,

$$F_t = \sqrt{(p - p_a)^2 + \left[q - \left(1 - \frac{\alpha}{\cos \beta}\right)(d + p_a \tan \beta)\right]^2} - \alpha(d + p_a \tan \beta) = 0 \qquad \text{Equation 9}$$
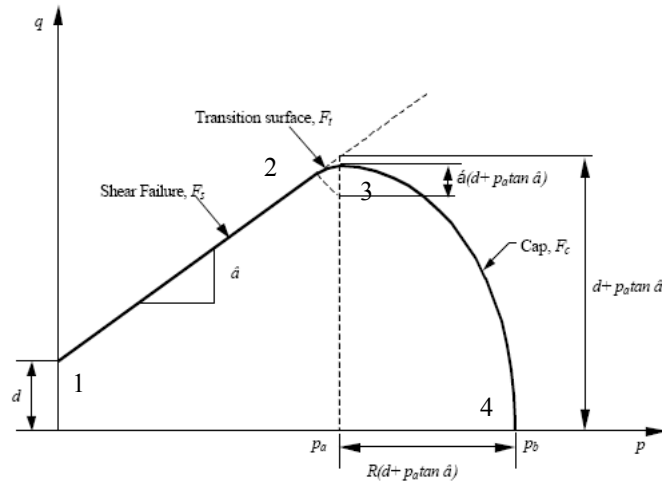
Figure 8 Modified Drucker-Prager Cap Model

These 3 surfaces can be used to model the 3 powder compaction stages. The linear

shear failure surface (from point 1 to point 2) represents the first stage of compaction,

rearrangement. In this stage, only elastic strain occurs in a low-pressure condition. The

intersection of the shear surface represents the material cohesion, and the slope of the

shear surface represents the friction angle of material. During the transition surface (from

point 2 to point 3), which is a circular arc and provides a smooth transition between the

shear failure surface and the cap surfaces, powder particles start to be compressed

together as voids in the powder collapse, and the onset of plastic strain begins. This

surface depicts the powders' deformation performance from the rearrangement stage into

the homogenous deformation stage as the pressure increases. More attentions have been

paid on the transition surface in computational geomechanics since the normal to the

surfaces at the transition may not be well defined (Simo et al., 1988).

The main plastic strain occurs in the cap shaped zone. At the end of the cap surface,

powders have been consolidated under high pressure, making the powder difficult to

compress. This is the 3rd stage of compaction, bulk deformation stage, which is occurring

between point 3 and point 4.

There are 8 material parameters involved in describing the Drucker-Prager cap model.

The details for each parameter will be discussed in the next section "Calibration of a cap

Model". A summary of these parameters is as follows:

E	Young's modulus
υ	Poisson's Ratio
d	Material cohesion
β	Angle of friction
R	Ratio of the horizontal axis of the elliptical cap to the vertical axis of the elliptical cap
$\varepsilon_{vol}^{pl}\|_0$	Initial volumetric inelastic-strain-driven hardening/softening
k	K is the ratio of the yield stress in triaxial tension to the yield stress in triaxial compression ($0.778 \leq K \leq 1$).
α	The parameter is a small number (typically 0.01 to 0.05) used to define a smooth transition yield intersection between the cap and failure surfaces.

For ferrous alloy powders, the plastic volumetric strain increases in compression with

increasing hydrostatic press, for instance, the pore volume shrinks. Figure 9 illustrates a

typical hardening low defining the relationship between the hydrostatic compression

yield stress p_b and the plastic volumetric strain ε_{vol}^{pl}. The evolution parameter p_a can be

related to p_b by

$$p_a = \frac{p_b - Rd}{1 + R\tan\beta} \qquad \text{Equation 10}$$

where p_b is related to axial stress σ_z by the following equation (Zipse 1997),

$$p_b = -\frac{(1 + R\tan\beta)\sigma_z}{1 + R\tan\beta\sqrt{1 + \left[\frac{2\left(\alpha - \frac{\alpha}{\cos\beta}\right)}{3R}\right]^2}} \qquad \text{Equation 11}$$
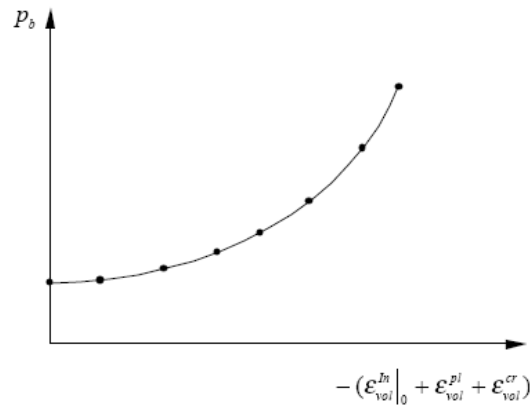
Figure 9 Hardening Law

Volumetric hardening is also defined by moving the cap along the hydrostatic axis in

Figure 9. When the axial compression force is increasing, the value of p_b is calculated.

The new p_b results the corresponding change of p_a and change the shape of the cap. This

will give a serious of cap surface during the compression simulation. Since the plastic

volumetric strain ε_{vol}^{pl} is related to the hydrostatic compression yield stress p_b by the

hardening law, these cap surfaces is correlated to the material hardening law. The

hardening law can related to two material constants W and D by the following

$$\varepsilon_{vol}^{pl} = W\left[1 - \exp\left(-Dp_b\right)\right]$$ Equation 12

The procedure how to obtain the hardening law is prescribed in section 2.3. As the

cap section proceeds, the ε_{vol}^{pl} increases leading in turn to an increase of P_b. The cap

moves to the right in Figure 8, increasing the extent of the elastic region inside the new

yield surface. Therefore, p and/or q must be increased to create a new cap section to

maintain the model.

2.3   Calibration of Cap Model

In order to create an appropriate Drucker-Prager cap model for a certain material,

eight parameters need to be calibrated. This requires significant experimental work. The

experimental methods can be summarized as follows (Simo et al. 1988; Zeuch et al. 2001,

Chtourou et al. 2002):

1. The powder medium elastic moduli are determined from resonant frequency

   measurements (Yu et al. 1992, Guillot et al. 1995).

2. A series of isostatic compression tests are carried out to determine the parameters

   of the model hardening law.

3. Additional triaxial and uniaxial compression tests are utilized for parameters of

   the cap model and of the failure surfaces (R and α).

The following chart illustrates a typical calibration procedure.

Shear failure
surface, d and β

Cap shape, R

Elastic modulus:
E and v

Hardening law

Test Techniques	Cap parameters
Resonant frequency	Elasticity
Hydrostatic compression	Hardening law
Uniaxial compression	Shear failure surface
Triaxial compression	Cap shape
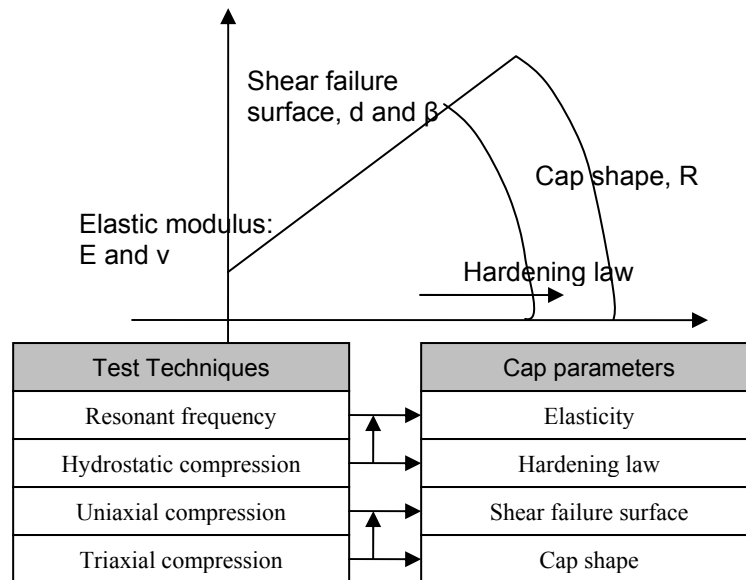
Figure 10 DPC Parameter Calibration Procedure

2.3.1 Elastic moduli (E, G and υ)

The free-free beam Sine wave excitation resonant frequency method (ASTM 2001) has been proven to be an accurate and effective tool to measure metal powder elastic properties. This method measures the fundamental flexural and torsional resonant frequencies of the specimens. The specimen is suspended by threads or wires and set to resonate by generating sinusoidal waves of a specific frequency using a frequency generator. Two phono-cartridges are attached to the threads to transmit and receive the vibration motion through the specimen. The frequency of a specific resonant mode can be determined on the oscilloscope screen by analyzing the Lissajou figures (Yu et al. 1992). The Lissajou figure is the combined trace of the input and output signals, acting

perpendicular to each other. Figure 11 is a typical setup of a free-free beam Sine wave excitation resonant frequency test and Figure 12 illustrates the position of a specimen bar suspended by threads.
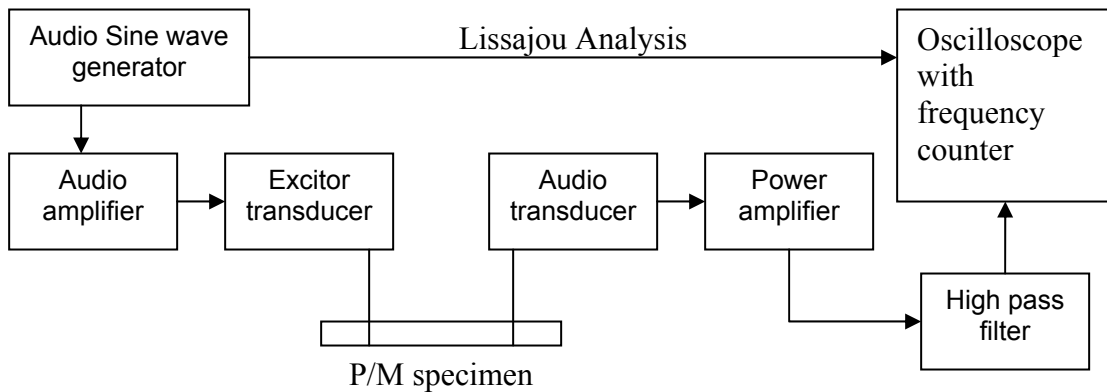
Figure 11 Setup of a free-free beam Sine wave excitation resonant test
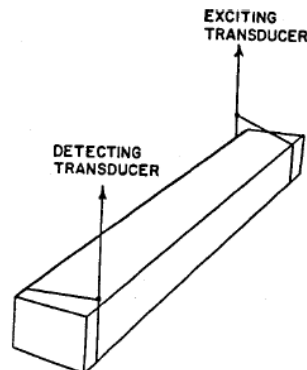
Figure 12 Specimen Positioned by Using Thread or Wire Suspension

An isostatic compression test is used to prepare specimens for the resonant frequency test since isostatic compression can produce compacts with quasi-constant densities. After isostatic compression, the specimen is machined into bars having appropriate dimensions for the resonant frequency test.

By using a relationship by Spinner and Tefft (Spinner and Tefft 1961), Young's (E) modulus, shear (G) modulus, and Poisson's ratio (υ) can be determined as a function of the compact density.

$$E = 0.9465 \frac{K_1 f_f^2 L^4 \rho}{t^2} \qquad \text{Equation 13}$$

$$G = 4 f_t^2 L^2 \rho K_2 \qquad \text{Equation 14}$$

$$\upsilon = \frac{E}{2G} - 1 \qquad \text{Equation 15}$$

where L is the length of the specimen, ρ is density, f_f is the fundamental flexural resonant frequency, f_t is the fundamental torsional resonant frequency. K_1 is the correction factor for the fundamental flexural mode to account for finite length, thickness of the specimen, and Poisson's ratio, K_2 is the shape factor for the fundamental torsional mode and depends on specimen thickness and width. K_1 and K_2 are given as follows:

$$K_1 = 1 + 6.585\left(1 + 0.0752\mu + 2.173\mu^2\right)\left(\frac{t}{L}\right)^2 - 0.868\left(\frac{t}{L}\right)^4 - \frac{8.34\left(1 + 0.2023\mu + 2.137\mu^2\right)\left(\frac{t}{L}\right)^4}{1 + 6.338\left(1 + 0.1408\mu + \mu^2\right)\left(\frac{t}{L}\right)^2}$$

Equation 16

$$K_2 = \frac{B}{1 + A} \qquad \text{Equation 17}$$

$$A = \frac{0.5062 - 0.8776\left(\frac{w}{t}\right) + 0.3504\left(\frac{w}{t}\right)^2 - 0.0078\left(\frac{w}{t}\right)^3}{12.03\left(\frac{w}{t}\right) + 9.892\left(\frac{w}{t}\right)^2} \qquad \text{Equation 18}$$

$$B = \frac{\left(\dfrac{w}{t}\right) + \left(\dfrac{t}{w}\right)}{4\left(\dfrac{t}{w}\right) - 2.52\left(\dfrac{t}{w}\right)^2 + 0.21\left(\dfrac{t}{w}\right)^6} \qquad \text{Equation 19}$$

where t is the thickness of the specimen, and w is the width of the specimen.

Yu et al. measured FN0208 and other iron alloy powders using the resonant frequency method and other methods (Yu et al. 1992). The calculated elastic moduli agreed within 3% deviation with the mechanical testing results (MPIF 1998) for the same powder type samples. Error analysis showed the error is less than 0.1% in the calculated Young's modulus and less than 1% in the calculated shear modulus. The following table shows measured shear moduli G for FN0208 specimens by the three test methods.

Table 2 Measured G by Yu et al.

Iron-Nickel MPIF Std.35	Alloy	Density g/ccm	Sine Wave Excitation G	Random Signal Excitation G	Impulse Excitation G
FN-0200-20	N0A	6.71	7.092	7.083	
FN-0200-25	N0B	7.41	9.476	9.494	
FN-0205-25	N5A	6.98	7.947	7.982	
		6.91			8.20
	N5B	7.11	8.559	8.557	
FN-0205-30	N5C	7.23	9.036	9.039	
FN-0205-35	N5D	7.46	9.697	9.694	
		7.37			9.73
FN-0208-35	N8A	6.89	7.785	7.330	
		7.03			7.924
	N8B	7.05	8.023	7.998	
		6.91			8.20

Using a similar measurement technique, Guillot et al determined E and G for 316L stainless steel powder (Guillot et al. 1995), and the result is shown in Figure 13.
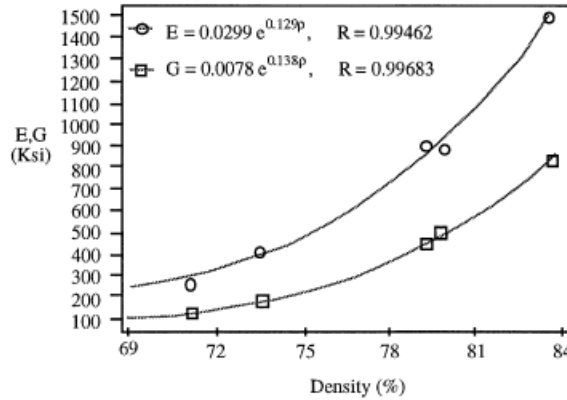
Figure 13 Young's Modulus and shear Modulus

2.3.2 Hardening Law

The hardening law corresponds to the relationship between the plastic volumetric strain ε_{vol}^{pl} and the stress tensor first invariant J_1. Since the elastic volumetric strain is much smaller than the plastic volumetric strain, the total volumetric strain ε_{vol} can be considered equal to the plastic volumetric strain, ε_{vol}^{pl}. A series of isostatic pressing experiments with different pressures can be used for this relationship. For each pressing, ε_{vol}^{pl} is computed from the initial powder density ρ_0 and the final compact density ρ using Equation 20.

$$\varepsilon_{vol} = \varepsilon_{vol}^{pl} = \ln\left(\frac{\rho}{\rho_0}\right) \qquad \text{Equation 20}$$

where, the densities ρ and ρ_0 are defined in MPIF standards respectively (MPIF 1986, MPIF 1992). The computed strain values can be plotted against J_1 corresponding to the isostatic pressure as in Figure 14 (Guillot et al. 1995). The material hardening law can be fitted using the format of Equation 12.
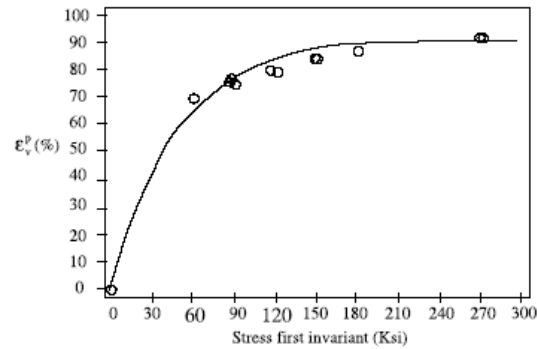
Figure 14 Hardening Law

2.3.3 Triaxial test

The triaxial compression test (ASTM 2003) is utilized to obtain the cap plasticity

parameters, including the cohesion, the friction angle, the cap shape parameter, and the

transition surface parameter (Meerman and Knaapen 1979; Aravas 1987; Riera and Prado

1994, Guillot et al. 1995; Haggbald et al. 1996, Chtourou et al. 2002). This test can

describe the *p-q* stress space for the cap surface using a number of different compact

relative densities by measuring the hydrostatic stress and volumetric strain. This will be

described in detail for each of parameters. The triaxial test was originally used by civil

engineers to investigate compaction behavior for rocks and soils. New apparatuses have

been developed to meet the particular needs for harder metal powders which are more

difficult to compress. The high pressure triaxial facility by Sinka et al. (Sinka et al. 2000)

has the ability to provide a 700 MPa confining pressure and 1100 MPa axial load. The

triaxial press by Doremus et al. (Doremus et al. 1995) can test a cylindrical sample up to

radial stress of 400 MPa and axial stress of 1125 MPa. The following figures show the

schematic diagram of a triaxial apparatus and a triaxial cell (Sinka et al. 2000).

Axial Displacement (Strain) and Load

Radial Displacement (Strain) and Pressure
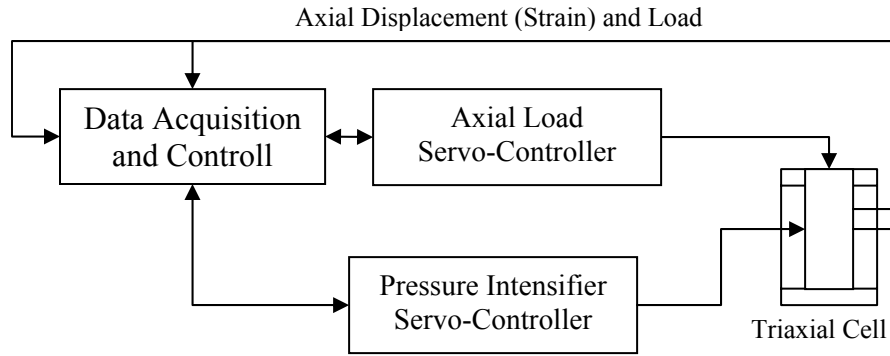
Figure 15 Schematic Diagram of Triaxial Apparatus
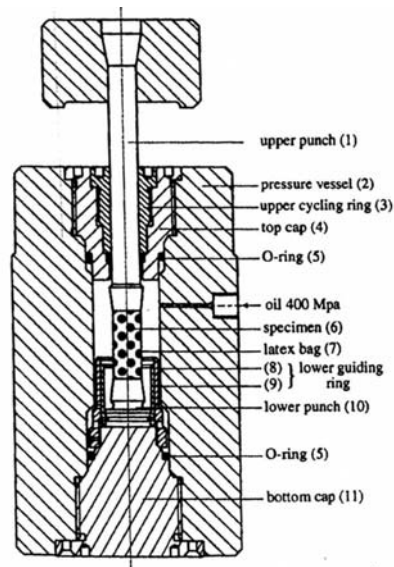
Figure 16 Details of Triaxial Cell

During triaxial compression, a specimen is encapsulated into a fixture consisting of

two punches and an elastomer sleeve. The arrangement is then subjected to an isostatic

fluid pressure. When a set pressure is reached, an additional axial pressure is applied

while the equipment control system maintains a constant fluid pressure. The axial load

slowly increases until fracture of the specimen occurs. During this process, the axial

pressure is recorded and the volumetric strain is measured. The following figure

illustrates the basic process of a triaxial test (Guillot et al. 1995, Chtourou et al. 2002).
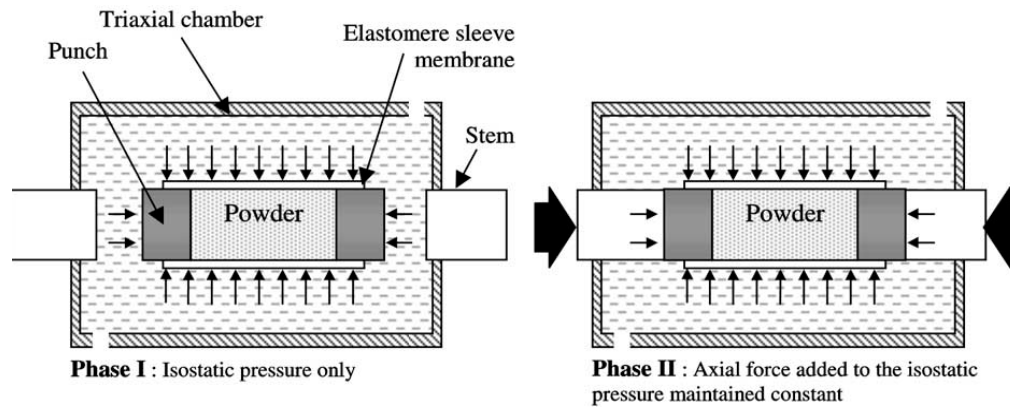
Figure 17 Triaxial Compression

The shear failure surface parameters (d and β) and the cap shape parameters (R and α)

can be determined by the triaxial test. The details of the measuring process will be

covered in section 2.3.7.

Although, technically, the triaxial test is an straight forward method for measuring the

cap plasticity parameters, the apparatus of the triaxial test is expensive and not readily

available, especially in powder metallurgy industry, due to the capacity to handle high

hydrostatic pressures for metal powders (Coube and Riedel 2000; He et al. 2001; Wagle

et al. 2003). This drawback significantly limits the usage of the triaxial method in

industry to determine the cap model parameters for different grades and combinations of

metal alloy powders. This in turn limits the practicality of predicting the density gradient

of a compact by using numerical simulation methods.

Researchers have investigated alternative methods for determine the cap parameters which eliminate the high confining pressure triaxial test. A combination of the Brazilian disc test (also called diametral compression test) and the compression test for the shear failure surface parameters, d and β, can be applied. However, the triaxial test is still known as the only experimental method to determine the cap shape parameters R and α.

2.3.4 Measurement of d and β by using triaxial test

In a modified Drucker-Prager cap model, the shear failure surface is linear and fixed for a particular material. This surface is defined as the point at which the volume strain curve totally reverses from compaction to dilatation and can be plotted as in Figure 8 in *p-q* space plane (or $\sigma_m - J_2^{'1/2}$ plane) (Aravas 1987; Aydin et al. 1996), where σ_m is the mean stress and $J_2^{'1/2}$ is the square root of the second invariant of the deviatoric stress, and corresponds to $\dfrac{(\sigma_1 + 2\sigma_3)}{3}$ and $\dfrac{(\sigma_1 - \sigma_3)}{\sqrt{3}}$ respectively. The slope of the line corresponds to tanβ, where β is the angle of internal friction. The linear shear failure surface intercepts the Y-axis at d, defining the cohesion of the powder material.

The shear failure surface parameters can be determined by a triaxial compression test. The process can be described as follows:

1. Starting with a hydrostatic state ($\sigma_1 = \sigma_2 = \sigma_3 = \sigma$). The hydrostatic pressure can be measured by a pressure cell and the deviatoric load can be measured by a load cell. Since areas of specimen surfaces are known, σ is able to calculated;

2. Two principal stresses are kept constant ($\sigma_2 = \sigma_3 = \sigma$), while an additional axial compression stress is applied in the third principal direction;

3. Measure stress σ_1 and $\sigma_2 = \sigma_3$, and deformations in the three orthogonal directions. Deformations are measured by linear variable displacement transducers (LVDTs);

4. Compute σ_m and $J_2'^{1/2}$ according to σ_1 and σ_3;

5. Keep $\sigma_2 = \sigma_3$ constant, increase σ_1 until a critical state is reached;

6. Plot the stress-strain curve. The intersection between the curve and the $J_2'^{1/2}$ axis is d and the slop of the curve is β.

In this way, the shear failure surface of 94% Alumina powder was obtained by Zeuch et al. (Zeuch et al. 2001). The results are displayed in the following figure.
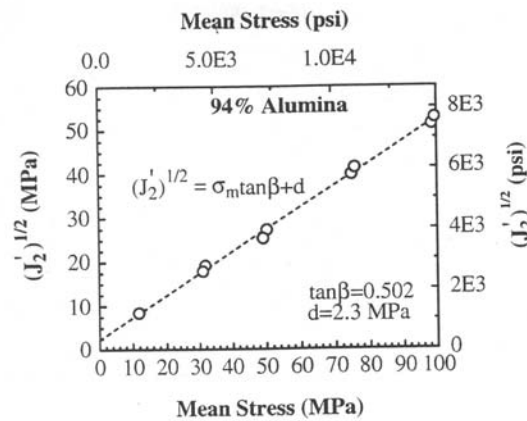
Figure 18 Shear Failure Surface by Triaxial test

As mentioned earlier, an alternative method using the combination of the Brazilian disc tests and the compression test to measure the green strength of the powder compacts has been used to obtain the shear failure surface parameters (Simo et al. 1988; Zipse 1997, Zeuch et al. 2001). This will be discussed in the following section.

2.3.5 Brazilian disc test

The split tensile strength is a measure of the ability of a material to resist a diametral compressive force placed on a cylindrical specimen with its axis placed horizontally between the platens of a test machine. The Brazilian disc test (also called diametral compression test) is commonly used to determine the tensile strength of brittle materials. For isotropic materials a simple relation based on specimen geometry and the applied load at failure is used to calculate the tensile strength (ASTM 2004),

$$\sigma_t = \frac{2P}{\pi LD} \qquad \text{Equation 21}$$

where, σ_t is the splitting tensile strength, P is the maximum applied load, L is the thickness of the specimen, and D is the diameter of the specimen.

The apparatus of the Brazilian disc test includes the loading device, bearing surfaces (false platens), spherical seating or rigid seating, and bearing strips. Figure 19 shows one typical test setup for a Brazilian disc test (ASTM 2004).
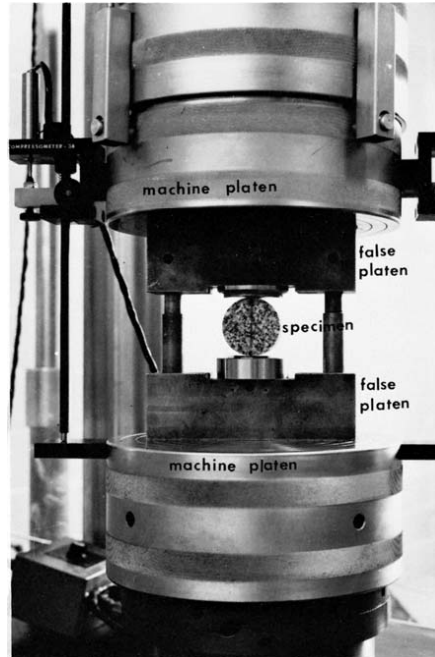
Figure 19 One of the Proposed Testing Setup for Splitting Tensile Strength

The basic procedure of a Brazilian disc test can be summarized as: marking, positioning, loading, and calculation. The marking process is to indicate the desired vertical orientation of the specimen by marking a diametral line on each end of the specimen. This process ensures the specimen is centered onto the spherically seated bearing surfaces. Also the marking process provides reference lines for thickness and diameter measurements. After positioning, the specimen will be subjected to a continuously increasing compressive load until failure occurs. The splitting tensile strength of the specimen will be calculated using Equation 21.

2.3.6 Determination of d and β by using Brazilian disc test

Since the shear failure surface of the modified Drucker-Prager cap model is a straight line in the *p-q* plane, the shear failure surface parameters d and β can be determined by a combination of a compression test and a Brazilian disc test. These two tests present different degrees of stress.

Defining σ_c and σ_t as the failure stresses, or ultimate compressive stress, obtained from the regular axial compression test and the Brazilian disc test, the corresponding values of p and q can be calculated (Simo et al. 1988; Timoshenko and Goodier 1987):

For the compression test, $\begin{cases} p = \sigma_c/3 \\ q = \sigma_c \end{cases}$ Equation 22

For the Brazilian disc test, $\begin{cases} p = 2\sigma_t/3 \\ q = \sqrt{13}\sigma_t \end{cases}$ Equation 23

Figure 20 illustrates the shear failure surface by using a Brazilian disc test and a uniaxial compression test.
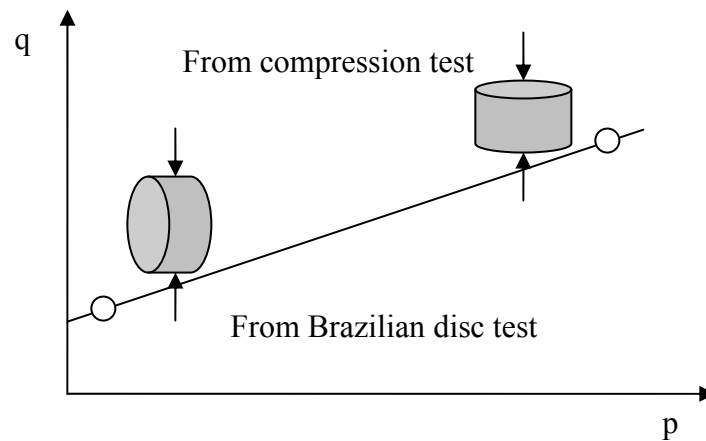
Figure 20 Shear Failure Surface by Brazilian disc test

2.3.7 Cap shape parameters (R and α)

According to literature (Aravas 1987; Chtourou et al. 2002; Guillot et al. 1995; Haggbald et al. 1996; Meerman and Knaapen 1979; Riera and Prado 1994), these two parameters, the cap eccentricity parameter R and the additional cap shape parameter α can only be determined by the triaxial test.

α defines a smooth transition surface (F_t in Figure 8) between the cap surface and shear failure surface. Normally, for a numerical simulation application, this parameter is chosen from a range between 0.01-0.05 (He et al. 2001; Wagle et al. 2003, ABAQUS 2003; Gunningham et al. 2004). But some evidences indicated the investigation of the value of α is necessary (Simo et al. 1985 and Zeuch et al. 2001).

A serious of hydrostatic compress tests and triaxial compression tests are required to determine R and α. It is important to select a set that represents the range of total volume strains that are attained during the hydrostatic compression tests and the triaxial deformation experiments. These values (X axis in Figure 22) are obtained by adding the volume strains from the hydrostatic compression experiments (X axis in Figure 21) to the strains accumulated during the triaxial tests. By repeating both hydrostatic compression tests and triaxial compression tests at specific volume strains, such as ε_v =0.40, 0.43 and 0.45, the corresponding $J_2'^{1/2}$ (the deviatoric stress q, which is defined by $\frac{(\sigma_1 - \sigma_3)}{\sqrt{3}}$) can be determined from σ_1 and σ_3. The results of the hydrostatic compaction test are plotted as pressures versus volume strains, as shown in Figure 23, and the curve can be fitted in

the format of $P_b = A\ exp\ (B^*\ \varepsilon_v)$. Where, the parameter A and B are constant for certain material. The corresponding hydrostatic pressure, P_b, is measured during triaxial compression tests.

The procedure for the triaxial test can be described as follows:

1. Starting with a hydrostatic state ($\sigma_1 = \sigma_2 = \sigma_3 = \sigma$). The hydrostatic pressure can be measured by a pressure cell and the deviatoric load can be measured by a load cell. Since areas of specimen surfaces are known, σ is able to calculated;

2. Two principal stresses are kept constant ($\sigma_2 = \sigma_3 = \sigma$), and an additional axial compression stress is applied in the third principal direction;

7. Measure stress σ_1, σ, and deformations in the three orthogonal directions. Deformations are measured by linear variable displacement transducers (LVDTs);

3. Compute σ_m and $J_2'^{1/2}$ according to σ_1 and σ_3 (σ);

4. Keep $\sigma_2 = \sigma_3$ constant, increase and record σ_1 and record the corresponding volume strain until a critical state, which could be crackers, a target axial load, or a target deformation, is reached;

5. Repeat the process using different confining stresses and deviatoric loads;

6. σ_1, σ_2, and σ_3 are measured as well as the three principal logarithmic strains;

7. Volume strains are computed by adding volume strains from the hydrostatic compression experiments to the strains accumulated during the triaxial tests;

8. At each state of volume strain, the deviatoric stress q and the equivalent pressure stress p are calculated and plotted for the determination of R as it is shown in Fatigue 23 (Zeuch et al. 2001).
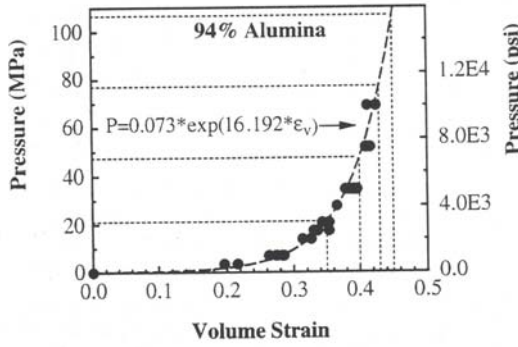
Figure 21 Pressure vs. Volume Strain (Hydrostatic)
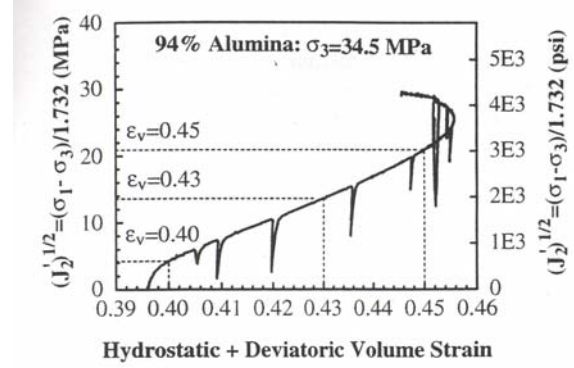
Figure 22 $(J'_2)^{1/2}$ vs. Strain (Triaxial)
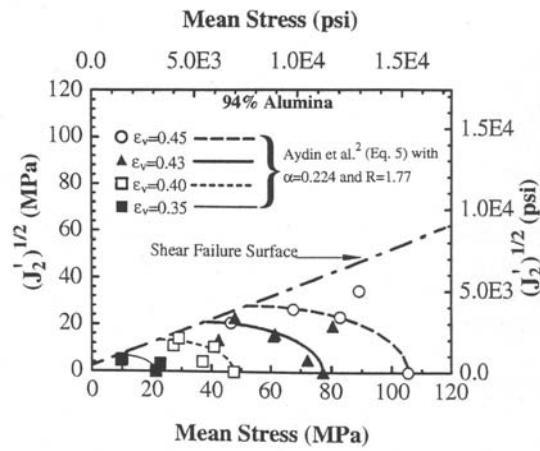
Figure 23 $(J'_2)^{1/2}$ vs. σ_m

The shape of the cap is then formulated according to the experimental data in terms of the cap shape parameter R and additional cap shape parameter α,

$$F_c = \left\{ (p - P_a)^2 + \left[\frac{Rq}{\left(1 + \alpha - \left(\dfrac{\alpha}{\cos \beta} \right) \right)} \right]^2 \right\}^{\frac{1}{2}} - R(d + P_a \tan \beta) = 0 \quad \text{Equation 24}$$

$$P_a = \frac{P_b - Rd}{(1 + R \tan \beta)} \qquad \text{Equation 25}$$

where, F_c is the function describing the elliptical cap, P_a is the cap evolution parameter, R and α are cap shape parameters.

In this method, Zeuch et al. found the cap eccentricity parameter R as 1.81 and the additional cap shape parameter α as 0.224 (Zeuch et al., 2001) for 94% alumina powders.

2.3.8 Additional parameter K

K is a material parameter defined as the ratio of the yield stress in triaxial tension to the yield stress in triaxial compression. This parameter controls the dependence of the yield surface on the value of the intermediate principal stress (shown in Figure 24, s1, s2, and s3 are principal stresses). The value of K falls in the range from 0.778 to 1.0 in order to ensure the yield surface remains convex. $K=1$ indicates the yield surface is the von Mises circle in the deviatoric principal stress plane. In this case, the yield stress in triaxial tension and compression are the same. $K=1$ is the default behavior in the FEM solver ABAQUS/Standard and the only option in FEM solver ABAQUS/Explicit (ABAQUS 2003). Most often, the value of K in a numerical simulation can be chosen as 1 (He et al. 2001; Wagle et al. 2003, ABAQUS 2003; Gunningham et al. 2004).
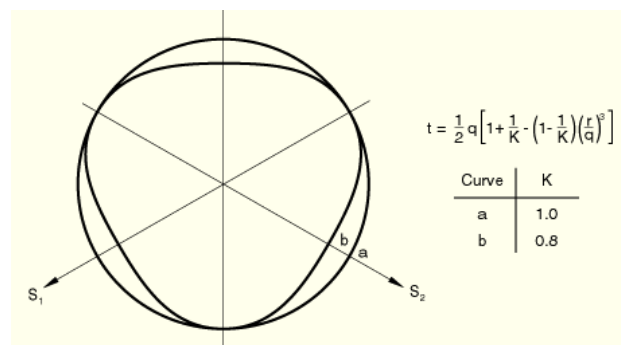
Figure 24 Yield Surfaces in Deviatoric Plane

Chapter 3   DETERMINATION OF CAP MODEL PARAMETERS USING A NUMERICAL OPTIMIZATION ALGORITHM

Currently, the triaxial compression test is the only method to determine the cap shape parameters for a modified Drucker-Prager cap model. As noted previously, it is difficult to do the triaxial test on ferrous powders. The first reason is that the hard iron powder requiress high confining pressure. The pressure to fulfill a triaxial test on iron-based powders can reach 45,000-60,000 psi (310-410 MPa) while aluminum powders requires 8000-20,000 psi (55-140 MPa) pressure. To perform such a high confining pressure test a special high pressure triaxial cell is required. Such facilities are unique and not commonly found in either industry or academic institutions. The high cost of the triaxial test equipment limits the ability to experiment with this method and has not be adopted by industry. These difficulties limit the practicality of accurately predicting the density gradient of compacts by using a numerical simulation.

Effort has been made to provide a practical method for determining the cap parameters without doing the triaxial test. Kwon et al. (Kwon et al. 2003) applied the Shima & Oyane yield surface(Shima and Oyane 1976) to substitute the cap surface of the cap model for the purpose of predicting internal crack formation during compaction. By this means, a pseudo cap model is created without the need for the cap parameter R and α since all material properties for a Shima & Oyane model can be determined by simple material tests. There is no transition surface between the shear surface and the cap surface.

It has been confirmed that the transition surface should be investigated more closely to construct the Drucker-Prager cap model (Simo et al., 1985). So this new model cannot represent the compression procedure properly due to the missing of transition surface.

Cunningham et al. generated an approximate equation based upon the cap surface equation and yield surface equation (Equation 7, 8) by assuming the friction force has a very small effect during powder compaction (Cunningham et al. 2004). Since friction is clearly a fundamental part of compaction and contributes to the differential in the density distribution in the green part, this model does not reflect the process properly.

Wagle et al. proposed a concept to determine the cap parameters using a backward method (Wagle et al. 2003). A series of triaxial tests are applied to different materials to create a prediction function for the cap shape parameters R and α. The basic idea of this method is to create a numerical model describing the relationship between the powder material properties, including R and α, and the distribution of green density using regression analysis. By measuring the distribution of green density, the cap parameters will be back calculated for a particular powder according to the determined relationship. This method requires a series of triaxial tests to obtain cap parameters for different metal powders in order to produce a universal regression model. Once again the triaxial test is needed for initial development.

In this research, a novel method to determine the cap parameters, R and α, using a combination of a numerical optimization method and common material tests will be developed.

3.1   Methodology

As discussed, there are 8 material parameters involved in a modified Drucker-Prager cap model. A summary of these parameters is listed below:

E   Young's modulus

υ   Poisson's Ratio

d   Material cohesion

β   Angle of friction

R   Ratio of the horizontal axis of the elliptical cap to the vertical axis of the elliptical cap

ε_{vol}^{pl} Initial volumetric inelastic-strain-driven hardening/softening

k   Ratio of the yield stress in triaxial tension to the yield stress in triaxial compression ($0.778 \leq K \leq 1$).

α   The parameter is a small number (typically 0.01 to 0.05) used to define a smooth transition yield intersection between the cap and failure surfaces.

In addition, the volumetric hardening law is necessary for creating a modified Drucker-Prager cap model.

The current method determines all of these parameters in the following ways:

1. E and υ can be determined by resonant frequency methods and are documented for many materials.

2. d and β is obtained by either a triaxial test, which is to be eliminated by the new method, or more typically from the combination of uniaxial compression and a Brazilian disc test.

3. The hardening law can be generated by a series of uniaxial compression tests.

4. $\varepsilon_{vol}^{pl}|_0$ can be chosen as a small number, such as 0.01, according to literature (He et al. 2001; Wagle et al. 2003, ABAQUS 2003; Gunningham et al. 2004;).

5. K can be chose as 1.0 based upon the literature (He et al. 2001; Wagle et al. 2003, ABAQUS 2003; Gunningham et al. 2004).

6. The cap parameters, R and α, will be only determined by iterative matching with a known geometric model and measured density distribution.

In the new method, the numerical simulation and the numerical optimization method, instead of a triaxial test, will be used to obtain the cap shape parameters R and α.

This method can be split into 3 sections: a FEA section, an experimental section, and a numerical optimization section. The key point of the new method is to determine the cap shape parameters R and α so that the density difference between the "real" measured density distribution map and a simulated "FEM" green density distribution map is minimized. This procedure will be implemented with simple geometry and standard

numerical optimization methods to obtain a set of R and α for the minimized density difference. Since R and α are material properties, the predict values can be utilized for arbitrary geometry and test simulations.

A uniaxial compression test will be carried out on a sample part in order to measure a green density distribution map. This measured density map will be considered as the result that is to be expected if the FEM simulation is correct. A series of numerical simulations will be done using the modified Drucker-Prager cap model to produce simulated density distribution maps with different sets of R and α value. This work can be classified as the FEA section. Comparing the actual density map with the simulated density distribution maps using some image comparison techniques, a function of the density difference will be generated indicating how close these two maps are. Applying numerical optimization methods, a set of R and α producing a minimum difference will be found. If this difference is acceptable, this set of R and α will be retrieved as the true value for the particular powders. Otherwise, the number of numerical simulations will be increased for a more accurate difference function.

In summary, the method developed in this research can be described as:

1. E and υ can be determined by resonant frequency methods or through the literature.
2. d and β will be obtained by a combination of uniaxial compression and a Brazilian disc test.
3. The hardening law can be generated by a series of uniaxial compression tests.

4. ε_{vol}^{pl} can be chosen as a small value, such as 0.01 according to literature.

5. K can be chose as 1.0 based upon literature.

6. A uniaxial compression test on a certain metal powder sample part with a simple geometry, such as a cylinder, will be completed.

7. The green density distribution map M_e over a cross-section of the sample will be measured by using volume fraction as determined by image analysis methods.

8. A series set of R and α values will be generated to produce simulated density distribution maps M_s.

9. Comparison of M_s and M_e will be made in order to obtain a function describing density difference.

10. Numerical optimization analysis will be performed to find the R_r and α_r value producing the minimum density difference.

11. If the difference is acceptable, the whole process stops, and the value of R_r and α_r will be obtained as the estimated material properties for this particular metal powder.

12. If the difference is not acceptable, predict new values for R and α by applying a numerical optimization method for a more accurate difference function.

13. Repeat step 8 to step 12 until the minimum difference is acceptable.

Figure 25 illustrates the flowchart of the new method. The FEA section, experimental section, and optimization section are outlined.
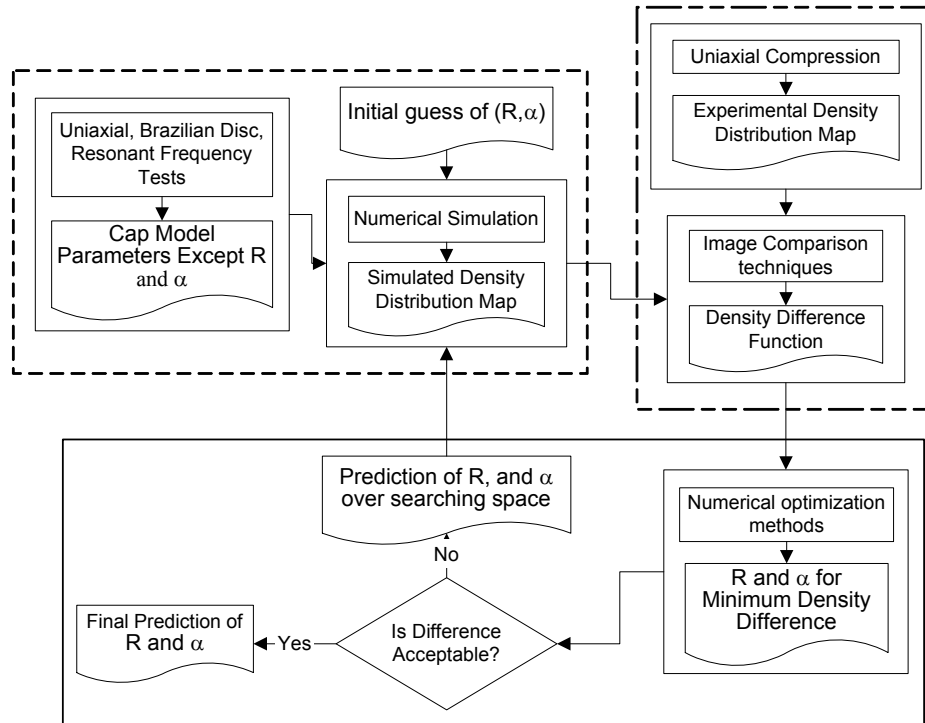
Figure 25 Flowchart of the Determination of R and α

This new method associates the numerical optimization algorithm with common material experimental tests to determine the cap shape parameters instead of doing an expensive triaxial test. Many advantages are apparent through utilization of this procedure. The triaxial test will not be involved, which means the cost of the process will sharply decrease and the practicality of using the Drucker-Prager cap model will be significantly increased. Also, this new method to determine R and α is programmable. This feature enables that the determination of R and α will be finished in a relatively short time. Thus, the cost and time will be lower again. This method is a universal process and can be applied to many types of particulate materials. Furthermore, this method can be expanded to determine other DPC parameters.

3.2   Sample Parts

Iron-based (FLC2-4808) ring samples produced by uniaxial compression have been adopted in this research. The sample has an outer diameter as 0.88 inches (2.24 cm) and inner diameter as 0.58 inches (1.47 cm). The initial height of the ring is 1.22 inches (3.1 cm), and the height after compaction is 0.61 inches (1.55 cm). The part is produced by die compression using a 50T mechanical/hydraulic double-action press. The specimen is pre-sintered at a temperature of 1350 ºF for 20 minutes in a Nitrogen atmosphere in order to burn lubricant out but without changing the density distribution. The filling density of the part is 3.2 g/cm^3, and the green density is roughly 6.8 g/cm^3. The following pictures show the dimensions and a 3D solid model of the specimen.
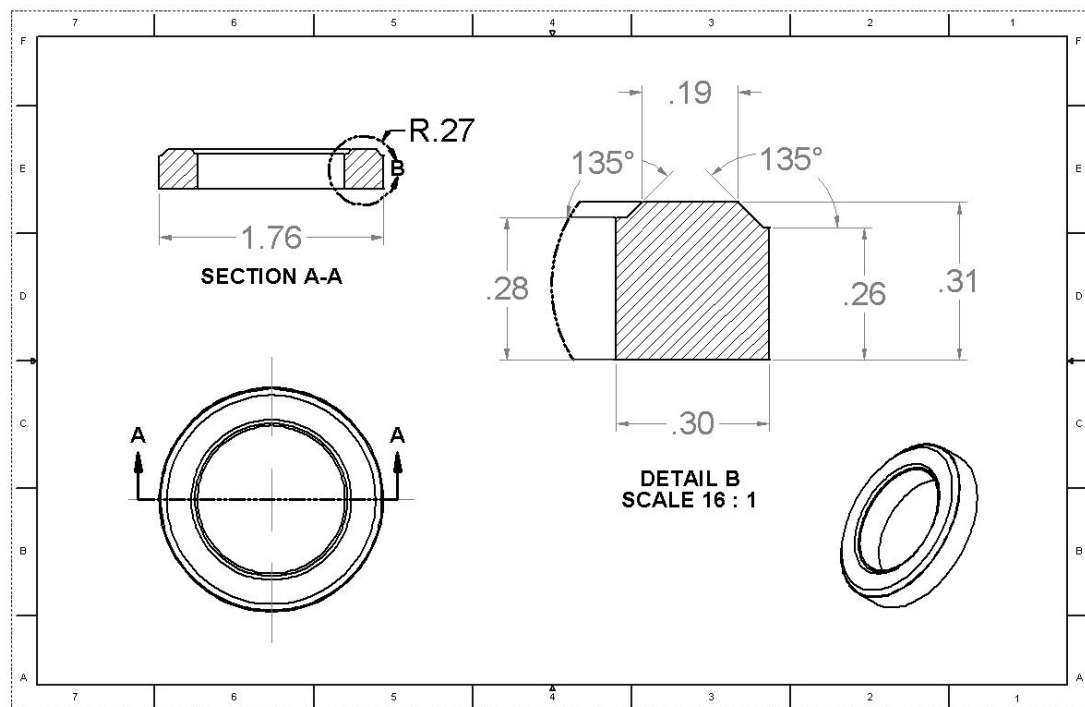
Figure 26 Dimensions of Specimen
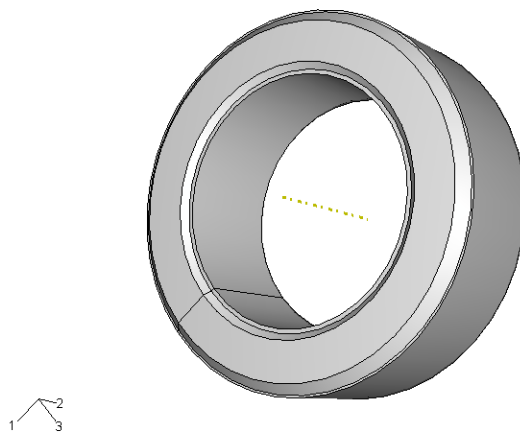
Figure 27 3D Solid Model of Specimen

3.3 Powder Characterization

3.3.1 Chemistry Components

FLC2-4808 is a common sinter hardenable powder that has been designed to eliminate post heat treating processes. The chemical compositions of this ferrous powder are C, Ni, Mo, Cu, and Fe. The percentage for each composition is listed below. The typical density ranges of FLC2-4808 powder vary from 6.6 to 7.2 g/cm^3 (MPIF 1998).

Table 3 Chemistry Components of FLC2-4808

Chemical Composition, % - Sinter Hardened Steel							
	Fe	C	Ni	Mo	Cu	Mn	Element
FLC2-4808	Balance	0.6	1.2	1.1	1.0	0.3	Minimum
	Balance	0.9	1.6	1.4	3.0	0.5	Maximum

3.3.2 Particle Shape

Although the particle shape provides useful information for packing, flow, and compressibility, it is difficult to quantify. Instead, the qualitative description is often utilized. The scanning electron microscope method (SEM) is among the most often applied methods to visualize the particle microstructural characterization. To take a SEM photo of powders, the sample powders were stuck evenly on the surface of a piece of double-face tape forming a thin layer of powder. Then the powders were put under a scanning electron microscope (JEOL JSM-35). A series of SEM photos were taken with the magnification varying from 300 times to 10 times. The magnification of the photo is shown at the left lower corner, while a standard scale was shown in the right lower corner. The SEM photos confirm the FLC2-4808 powders tend to show an irregular equiaxed shape. Two of these photos are shown below.
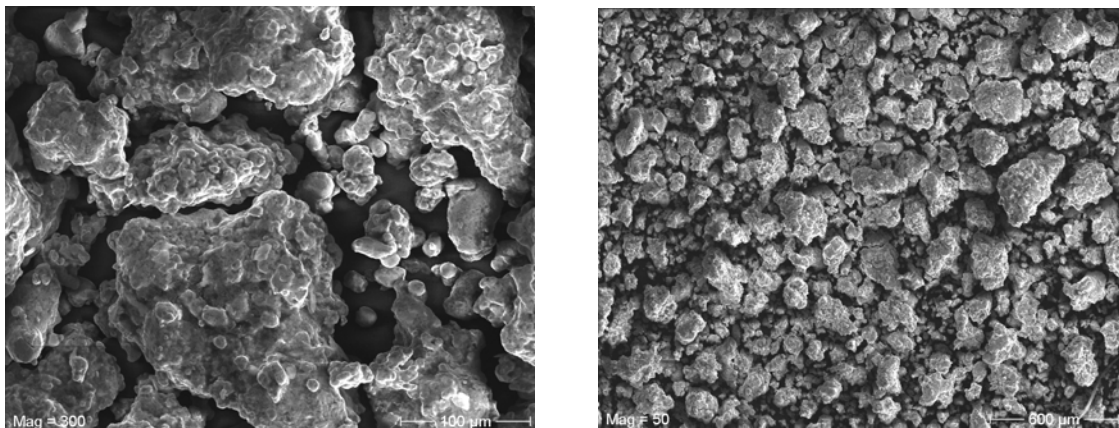
Figure 28 FLC-4808 powder SEM photos, 300X and 50X

3.3.3 Particle Surface Area

The most common method to determine specific surface area of porous compacts is BET (Brunauer-Emmett-Teller) analysis. BET theory defines a rule for the physical adsorption of gas molecules on a solid surface and was published by Stephen Brunauer, Paul Hugh Emmett, and Edward Teller in 1938 (Brunauer, Emmett and E. Teller 1938). Detailed procedure is defined in ASTM B922 - 02(2008), "Standard Test Method for Metal Powder Specific Surface Area by Physical Adsorption". Due to the lack of equipment, this experiment was not carried out.

3.3.4 Particle Size

The sieve analysis was carried out to determine the particle size distribution of FLC2-4808 powders. The sieve analysis is the most simple and effective method to measure the particle size and can be performed on any type of granular materials including sands, soil, manufactured powders, etc. It is implemented easily in a material test laboratory due to the simplicity of the instruments and the low cost. The standard screen size and openings can be found in metallurgy handbooks and standards (ASTM E11-01 2001). Some of the typical standard screens are shown below.

Figure 29 Sieve Sizing Analysis Screens

A sieve analysis began with a stack of screens with approximately 100 gram of powder loaded. Eight screens were used in this test. The largest screen opening was put on the top, and the smallest opening was on the bottom, so smaller particles would be able to go further down to the finer screen than the larger particles. The FLC2-4808 powder was vibrated manually in the sieve screen set for 10 minutes and then weighed. The weight of powders in each screen was recorded to calculate the percentage for each powder size. To achieve a precise measurement, this procedure was repeated three times, and the average results are calculated.

Table 4 Particle Size Distribution Data

Mesh size	Opening (μm)	Weight (g)			
		1st trail	2nd trail	3rd trail	Average
60	250	0	0	0	0
100	150	24.60	22.45	23.38	23.48
120	125	18.62	19.37	20.68	19.56
200	75	40.20	39.21	40.57	39.99
230	63	12.41	13.89	11.74	12.68
325	45	2.42	3.47	2.81	2.90
400	37	0.10	0.25	0.19	0.18
500	25	0.15	0.07	0.21	0.14
	total	98.50	98.71	99.58	98.93
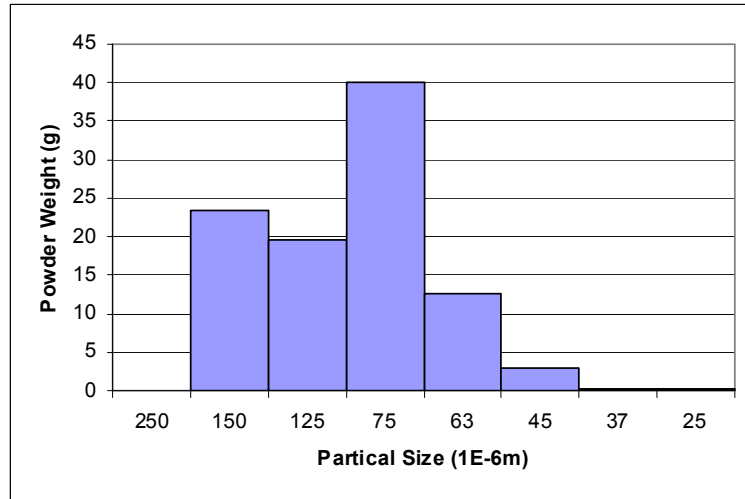
Figure 30 Histogram Plot of Powder Size Distribution

The above figure visualizes the percentages for each powder size. Normally, metal powders exhibit a bell shape curve (Gaussian or normal distribution) in this plot (German 1997), but the FLC2-4808 powder presents a distribution other than the normal distribution. Also, how particle size and shape affect R and α is not identified and has not been seen in literature.

3.4   Determination of Cap Parameters

The finite element analysis process in this research adopts ABAQUS built-in modified Drucker-Prager cap model as the failure criteria. ABAQUS provides various porous material models that can be used in powder compaction process simulation (ABAQUS 2003). This feature makes ABAQUS preferred over other commercial FEM software packages in the powder metallurgy area. As discussed in Chapter 2, eight material parameters need to be calibrated for this cap model. Among the eight parameters,

Young's modulus, Poisson's ratio, material cohesion, angle of friction, initial volumetric hardening/softening, and hardening law for iron powder can be obtained by simple material property tests. The equipment for these tests is easy to find in a common material laboratory. The major problem arises from the lack of ability to implement the triaxial test, which is the only way to obtain the other two parameters, cap eccentricity parameter R and transition parameter α. R defines the shape of the cap surface and gives the cap model the greatest impact. In this research, R and α will be determined over their searching space, which defines the maximum and minimum values of the parameters, by using an optimization method (details of searching space will be discussed in the following chapter).

Most of the above parameters do not stay constant with an increase of relative density during compaction, but for the finite element analysis purpose they are normally treated as constant (Kwon et al. 1997, He et al. 2001; Lee and Kim 2002, Wagle et al. 2003). The first reason to consider the parameters as constant is the lack of experimental data. After the functions describing the relation between the parameters and density are retrieved by empirical means, they would be implemented in FEA codes by some means. This is a promising area for further study.

Young's modulus, Poisson's ratio, material cohesion, angle of friction, initial volumetric inelastic-strain-driven hardening, K, and the hardening law for iron powder can be obtained from the literature and are detailed below.

Poisson's ratio of iron powders can be taken as 0.27 (MPIF 1998). Young's modulus of ferrous powders is a non-linear function of the compressed density, starting from 12 GPa at 3.2 g/cm^3 and increasing to 200 GPa at 7.2 g/cm^3 (Coube and Riedel 2000, ABAQUS 2003). Through curving fitting, the function can be written as

$$E = 0.7194e^{0.7641\rho} \qquad \text{Equation 26}$$

where, E is Young's modulus and ρ is the density.
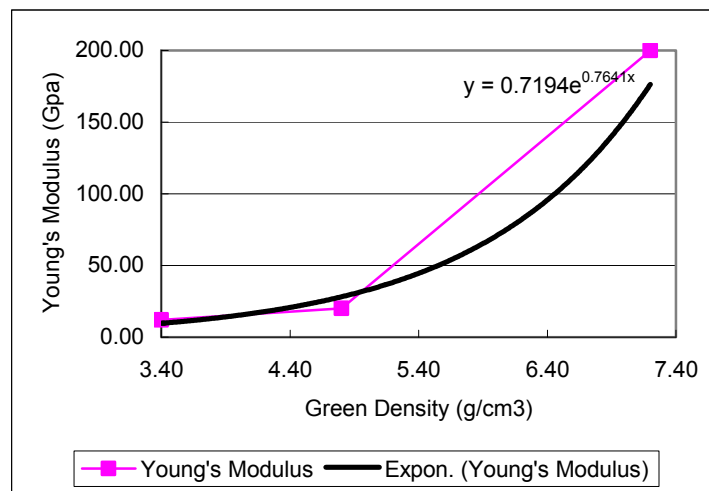
Figure 31 Young's Modulus

To reflect the effect of the density change on Young's modulus during compaction, the ABAQUS user-defined subroutine USDFLD() was applied. USDFLD() allows users the flexibility to write FORTRAN subroutines in order to define additional variables in a FEM model according to results from the previous calculation iteration. In this way, the function of Young's modulus in terms of the green density (Equation 26) was applied to numerical simulation models. The FORTRAN subroutine altering the Young's modulus according to the value of the green density during the computation is attached in Appendix A.

Research by Coube and Riedel showed that although the material cohesion and angle of friction increase along with the increase of density, the variation of these two material parameters has a negligible contribution to the final density distribution (Coube and Riedel 2000). A similar conclusion was given by He et. al. (He et al. 2001). In this research these two parameters are chosen as constant during the simulation. The value is 26.2 MPa and 77.1˚ respectively (Kwon et al. 1997, PM MODNET 1999, He et al. 2001, Wagle et al. 2003).

As described in the previous chapters, the initial inelastic strain driven hardening/softening should be a small number, normally $0.01 - 0.1$ (Chtourou et al. 2002, Coube and Riedel 2000, Lee and Kim 2002, ABAQUS 2003), since it makes a small contribution to the final result. K can be chosen as 1 according to literature (details see section 2.3.8).

A summary of the values of these parameters is listed below.

Table 5 Determination of Cap Model Parameters

Young's modulus	12 GPa at 3.2 g/cm^3, 200 GPa at 7.2 g/cm^3, see Figure 31.
Poisson's ratio	0.29
Material cohesion	26.2 MPa
Angle of friction	77.1˚
Initial volumetric inelastic-strain-hardening	0.01
K	1.0

A series of isostatic pressing experiments create the hardening law for porous

materials. In this research, the hardening law was borrowed from an experimental

equation generated by Coube and Riedel (Coube and Riedel 2000). This hardening law is

input in ABAQUS as piecewise linear functions. More experimental results would be

helpful.
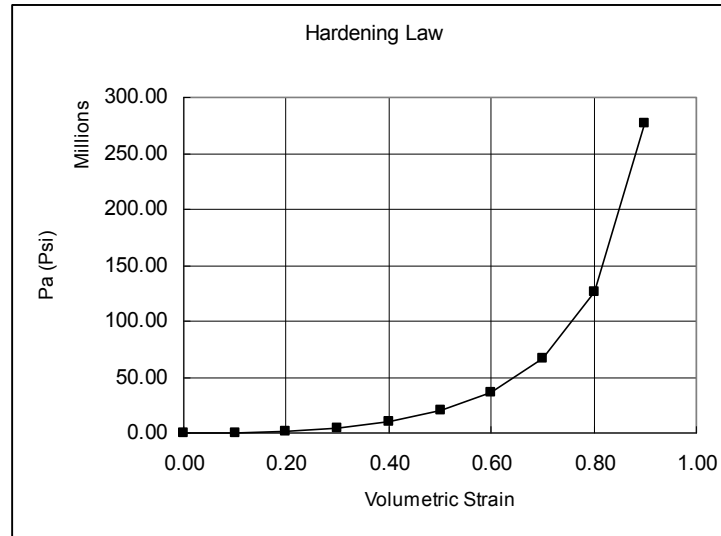
Figure 32 Hardening Law

Two DPC cap parameters were determined by the proposed numerical optimization

method. The initial value for R and α is 0.1 and 0.05 respectively. The determination of

these parameters will be covered in section 3.5.

3.5   Numerical Simulation Model

The ring shown in Figure 26 was modeled in ABAQUS pre-processor ABAQUS

CAE. Since the material of punches and dies are much stiffer than the porous ferrous

powders, they were modeled as rigid bodies. The element type for all parts of the

simulation model was 4-node-bilinear-axisymmetric-quadrilateral element (CAX4R). The use of the bilinear element helped to deliver a higher accuracy result than the use of a linear element. The quadrilateral element provided a continuous stress flow among the elements so that it not only produces a more accurate result, but also a better result visualization than triangle elements. 4-node-elements are used because they provided accurate FEA results with shorter computational time than 8-node-elements (based upon FEA experience, for a static non-linear problem, the run time is about tripled if 8-node elements are used).

"Tie" interactions between punches and the top and bottom of powders are defined to ensure the powders deform following the rigid tool bodies. Since friction forces contribute a lot to the density distribution during compaction, the friction forces between powders and tools were defined. In reality, the friction forces keep changing during compaction. This change is cause by many factors, for instance, part geometry, powder density, press speed, pressure. The friction coefficient varies typically from 0.08 to 0.2 according to literature (Coube and Riedel 2000). In this research, it was assumed that the friction would not change during the whole procedure, and the friction coefficient was selected as 0.17 (Kwon et al. 1997). It will be beneficial to gain better understand of the powder behavior during compaction to study the change of friction forces in detail. The FEA mesh of the sample ring is shown below.
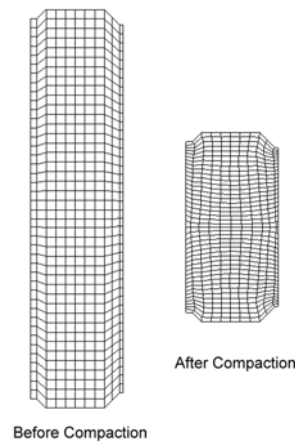
Figure 33 FEA Mesh of Sample

ABAQUS/Standard is a general-purpose finite element code, and was used as the computational module for the simulation. This research is a nonlinear (material nonlinearity) static analysis. Based upon the ABAQUS analysis user's manual, the static, general method is most suitable (ABAQUS 2003). Two kinds of matrix solver are available in ABAQUS: the direct method and the iterative method. The direct sparse solver uses a "multifront" technique that can reduce the computational time to solve the equations dramatically if the equation system has a sparse structure. Such a matrix structure typically arises when the physical model is made from several parts or branches that are connected together. The iterative method is good for a blocky structure, such as a single, solid 3D structure. Normally, it is more efficient, and requires less computational resource. The disadvantage is the convergence. Considering the scale of this research and the geometry of the sample, the direct method is used as the solver. Usually it is not necessary to specify the matrix storage and solution scheme (ABAQUS 2003). The only reason to select the storage method option is to improve computational efficiency. In this

research, the solver chose this option. The following screenshots shows settings. The
computation lasts about 20 seconds when R equals to 0.01 on a Pentium 4 1.8 GHz laptop
and increases to 20 minutes when R is 2.2 since a greater R requires more computations
(details see section 2.2.3).
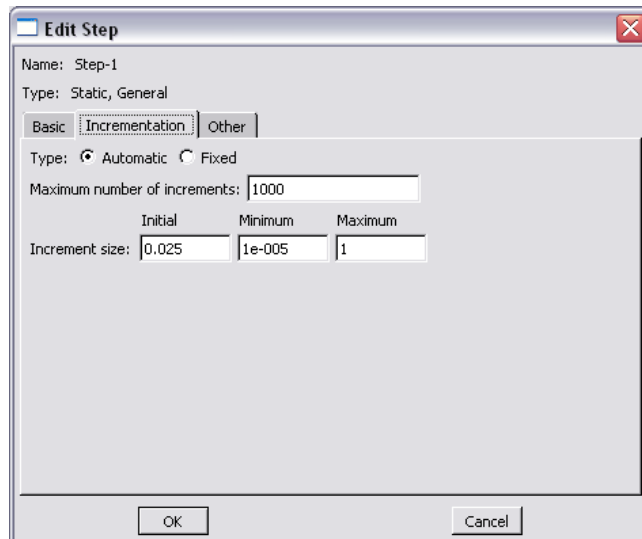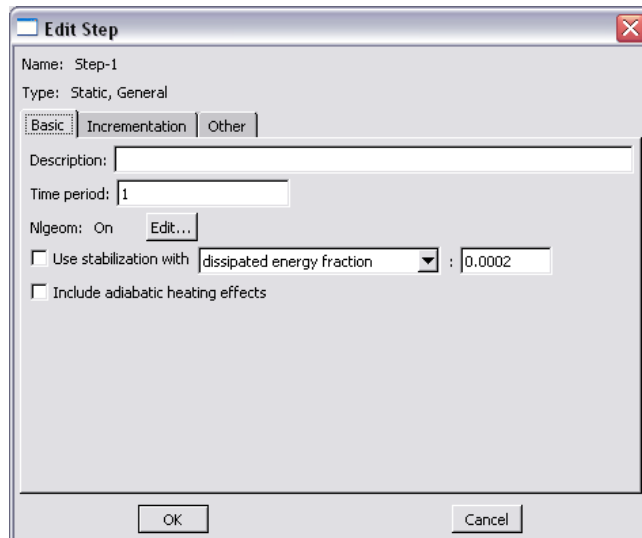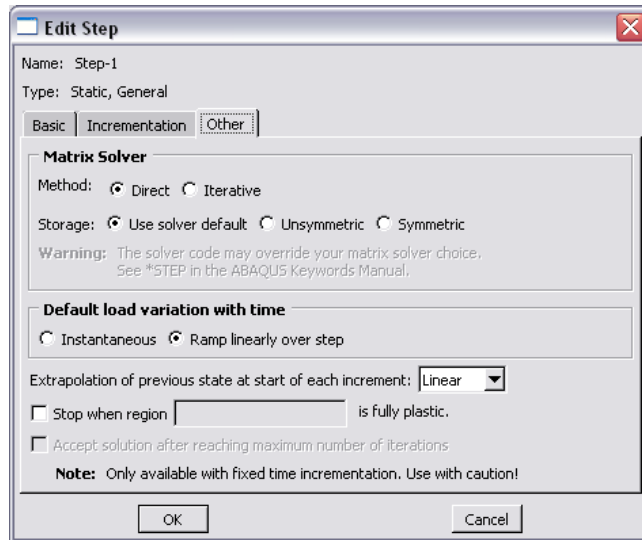
Figure 34 Screenshots of Step Settings

3.6   Simulated Density Distribution Map

ABAQUS computes the plastic strain, PEQC, distribution as one of its outputs
(ABAQUS 2003). The green density is related to the plastic strain by Equation 20.

$$\varepsilon_{vol} = \varepsilon_{vol}^{pl} = \ln\left(\frac{\rho}{\rho_0}\right) \qquad \text{Equation 20}$$

where, ρ_0 is the initial powder density and ρ is the compact density. In this manner, the

green density map can be determined after the plastic strain map is obtained. The

distribution map of the plastic strain, PEQC4 for the cap model, can be output in the

ABAQUS post-processor. The result can also be written into an ASCII output file for

further use.
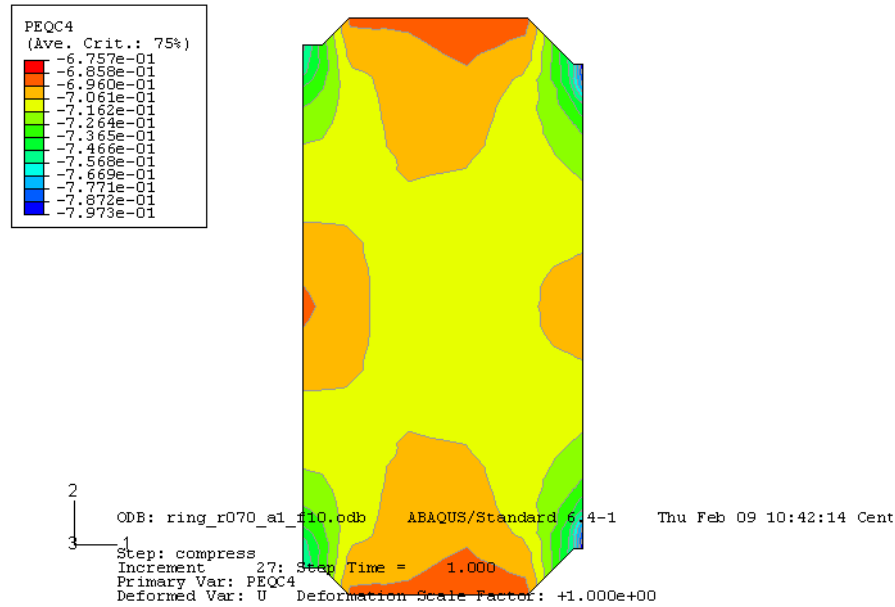
Figure 35 Simulated Plastic Strain Distribution Map

The above figure illustrates one of the simulated plastic strain distribution maps by ABAQUS (R=0.74, α=0.01). The strain value is taken as positive for density computation by convention. The greatest density value occurs at the upper right corner, while the smallest value occurs at the middle of the sample. After transforming plastic strain into density, this result gives the greatest density value as 7.2 g/cm^3, the smallest as 6.7 g/cm^3 and the overall density as about 6.9 g/cm^3. This result agrees with the density measured through bulk density methods (Archimedes principle).

The plastic strain information was read and processed by a MatLab program for the plot of the simulated density map. The program processed the elements inside a certain area. The reason will be discussed in section 3.7.2. The following picture illustrates the processed zone and one of the FEA density maps.
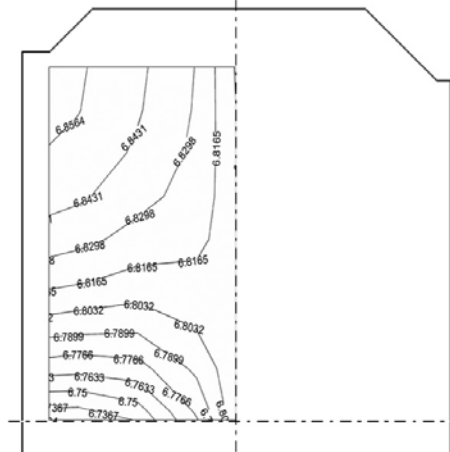
Figure 36 FEA Density Map

3.7 Actual Density Map Measurement

Various methods, image analysis, Vickers hardness, tomography method (Guillot et al., Kwon et al. 1997, 1995, Phillips and Lannutti, 1997, Burch, 2002, Kim et al., 2002, Sinka et al., 2004, Miguelez-Moran et. al. 2009), exist for local density measurement. Features of the above methods have been briefly summarized in the following table. Considering the existing equipment, the accuracy, and the cost, the image analysis technique was chosen.

Table 6 Brief Summary of Local Density Measurement Methods

Methods	Destructive	Cost	Common Artifacts
Image Analysis	Yes	Low	Artifacts due to sample preparation; Inconsistent contrast among photos
Hardness Method	Yes	Low	Artifacts due to sample preparation; pores may provide incorrect readings
X-ray CT	No	High	Beam hardening, aliasing, etc

The basic concept of the image analysis method is the local relative density is defined as the area of powder divided by the theoretically possible area, then the image analysis software program counts the voids and solids in a photo based upon the different colors that they have. In the following picture, the black areas are the voids, and the yellow areas are powders. The relative density is computed as the number of pixels of powder over the number of pixels in the whole area, and then the local density equals the relative density multiplied by the theoretical density of the material.
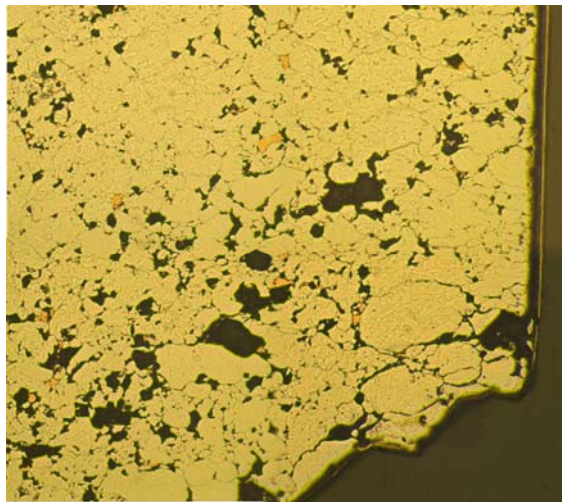
Figure 37 Picture at Specimen Corner

The density distribution map of a cross section of the sample parts was measured using image analysis. The optical equipment was an Olympus PME3 microscope and a 2 mega-pixel InSight CCD camera attached to the microscope. The CCD camera was connected to a personal computer to record the digital photos. The image analysis software utilized was SimplePCI.

SimplePCI is a high performance imaging software program designed to meet the needs for high-speed processing at a low cost, with ease of use and flexibility. It is produced by the Hamamatsu Corporation, which is famous for its optical products and image analysis systems.

Figure 38 Olympus PME3 and InSight CCD Camera

Figure 39 Setup for Digital Image Acquisition System

3.7.1 Specimen Preparation

To prepare the specimen, the P/M compact was cut by a LECO saw. Because the strength of a compact is less then that of a solid material, the edges of compact are fragile. In order to minimize damages of the fragile edges and corners caused by mounting and polishing, the specimen was edge enforced. The Buehler Epo-Thin epoxy solution, which is low viscosity, low shrinkage, and transparent, was utilized for mounting purpose. This step allows a convenience for further process and a protection to the sample. Then after the epoxy became solid, the polishing process was undertaken on the mounted specimen. During the polishing process, 0.1µm and 0.05µm Aluminum powders were used for 30 seconds each. The equipment utilized in the specimen preparation is pictured below.

Figure 40 LECO CM-15 Cut-off Machine

Figure 41 Buehler Handimet Grinder

Figure 42 Buehler Polisher and Polishing Powders

Edge enforcement and infiltration are available to protect fragile areas. The first method creates an electroless nickel coating on the surfaces of the specimen by a manner of electroplating. This avoids powders inside the coating from being taken away by polishing. For this purpose, the Buehler EdgeMet Kit was used to add a 0.001" thick coating of nickel. Plating was done at 180°F to190°F for 2 hours. The coating can be seen clearly in Figure 37 on the right vertical edge. The details of the process can be found in the instruction of the EdgeMet Kit.

Figure 43 Setup for Edge Enforcement

The second method evacuates the air inside the pores of the test sample and allows liquid epoxy to be sucked into the voids. This makes the voids strong enough for further processing. For this process, the specimen was put into a dessicator that was connected to a vacuum pump. A vacuum is created for a certain time in the dessicator until the air in the specimen pores is removed. The epoxy infiltrates the voids by capillary action once the vacuum is removed. The epoxy solution will then harden under room temperature and

pressure. This method is straightforward; but still has complexities. One of them involves

keeping an appropriate amount of space between the bottom of the sample and the

specimen mold in order to infiltrate the right amount of epoxy into the voids without

adding significant gringding and polishing work. Figure 44 shows the equipment for

infiltration.

Figure 44 Edge Infiltration Equipment

The edge enforcement method was utilized in this research since it provides a better

protection at fragile edges by using metal material against epoxy in the infiltration

method. Another reason not to adopt the infiltration method is its complexity.

3.7.2 Local Density Measurement

After specimen preparation, the specimen was ready to be examined for the density

measurement. Due to the near-symmetric geometry and loading conditions of the sample,

a quarter of the cross section was measured. This saved measurement time and

computational cost. A rectangular section in the upper left quadrant of the specimen from

which 75 digital photos were obtained was utilized for the comparison process. Each

photo has the dimension of 0.50mm x 0.65mm. To reduce potential errors caused by the

individual measurement, three samples were used. The average value for the same area

was calculated as the local density. One of the mounted samples is pictured below. The

black spots in the shining cross section are the pores.
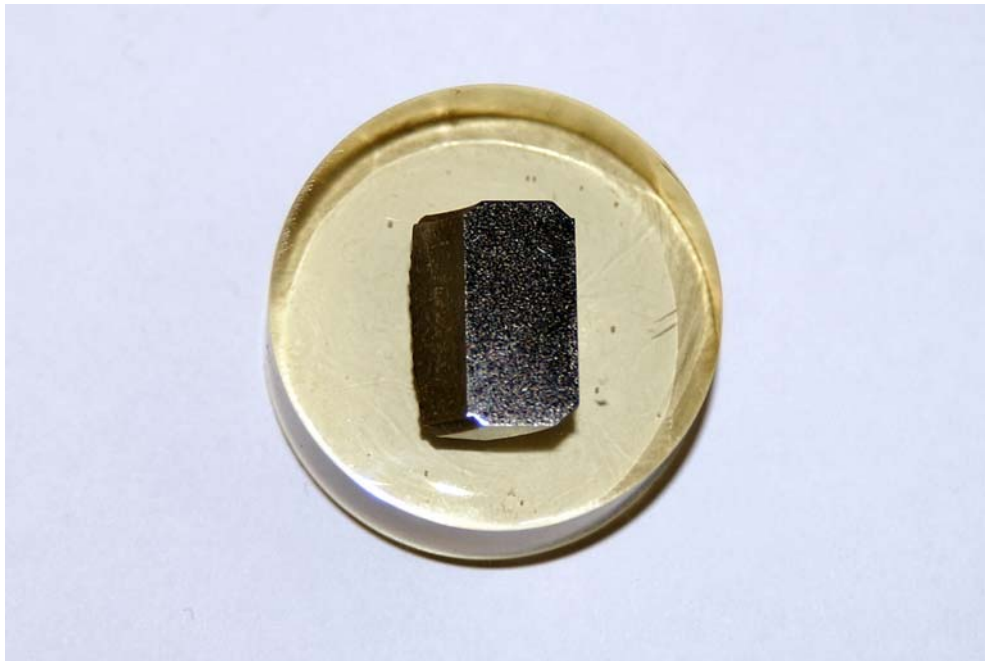
Figure 45 Mounted Specimen

One issue of the photo capture was that the contrast could change from photo to photo,

which means the photos display the same color differently. This is true when the

individual photo only covers a very small portion of the whole cross section of the specimen. A consistent contrast could not be achieved due to the considerable difference of distance and angle between the area under investigation and the light source. The reason why the contrast is critical is the contrast is recorded and applied by the image software to recover colors, and the density is calculated by the ratio of void and material, both of which are defined by different colors. Thus, if one object is imaged twice with different contrasts, to retrieve the same color, the contrast / white balance must to be adjusted. This is difficult and needs special skill since the change of the contrast is difficult to identify by untrained eyes. Another solution is to keep the contrast the same when pictures are captured. To do so, a white balance adjustment was done before each photo was taken. The purpose of this process is to adjust the contrast automatically to ensure the standard white color is able to be represented by the image process system. The process would not change the physical representation of the specimen. The auto white balance function is available in most image software.

The common way to describe colors in computer graphics applications is to define a color by the level of red, yellow, and blue (0-255) contained in the color. For instance, red is presented by (255, 0, 0), green is (0, 255, 255), and black is (255, 255, 255). SimplePCI utilizes this method too. To count the porosity of a sample, a threshold value defining the "void" in simplePCI is required in terms of the contrast of red, yellow, and blue. Based upon a series of trials, the configuration for red, yellow, and blue was set as (180, 255, 255) was applied to count the voids and material. This configuration produced

a satisfactory local density map. The raw image analysis data can be found in the appendix.

A MatLab program was generated to read the raw data in and to produce various regression models relating the local density to locations in terms of 2D coordinates. The core of this program is the regression algorithm. The MatLab function, nlinfit(), applied regression models to fit the raw data. The source code can be found in the appendix.

The standard format of the power and exponential model are not able to provide enough accuracy for fitting local densities because neither of them is able to provide enough terms of the independent variables for such a complex regression study. So in this research, the following standard formats of polynomial models were examined: 2nd order, 3rd order, 4th order, and 5th polynomial formulas. The following plots visualize the difference between the fitted data and the raw data from various regression models on one of the measurements. In the pictures, the X axis presents the photo numbers and the Y axis presents the local density. The sequence of the picture numbers is shown below. The curve in green is the original measured local densities, while the curve in blue is the fitted local densities.

	picture Column 1	…..	picture Column m
picture Row 1	picture #[1]	…	picture #[(m-1)*n + 1]
….	…	…	…
picture Row n	picture #[n]	…	picture #[m*n]

2nd poly

3rd poly

Figure 46 Density Plots for Polynomial Models at Various Locations

Obviously, the 4th order polynomial model produced a more accurate density variation than the 2nd and 3rd order polynomial models. The 5th order polynomial model was created for comparison. The model had 24 items but did not improve the accuracy significantly. So the 4th order polynomial model was used in this research to present the raw data. The standard format of the 4th polynomial equation is listed below,

Density = b1

$+ b2 * X + b3 * Y$

$+ b4 * X * Y + b5 * X \wedge 2 + b6 * Y \wedge 2$

$+ b7 * X \wedge 3 + b8 * Y \wedge 3 + b9 * X \wedge 2 * Y + b10 * X * Y \wedge 2$

$+ b11 * X \wedge 3 * Y + b12 * X \wedge 2 * Y \wedge 2 + b13 * X * Y \wedge 3$

$+ b14 * X \wedge 4 + b15 * Y \wedge 4$............   …Equation 27

where, X and Y are the coordinates of the center of the photos.

The following figure illustrates the local density distribution of a quarter of the specimen. This density map is considered as the actual (measured) density map in this research.
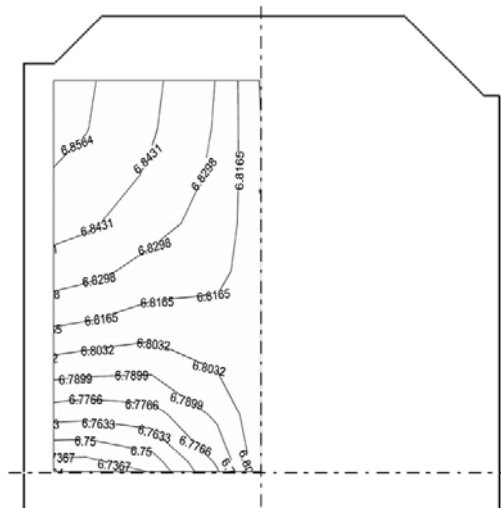
Figure 47 Measured Density Map

3.8   Search Space for R and α

The new method to determine R and α can be summarized into the following 2 steps: to determine the search space for R and α, and to select R and α to minimize the density difference between simulated and measured density maps.

The search space needs to be identified because the literature did not provide the information. The search space defines the lower and upper boundary of the parameters. The determination of the search space is one of the primary factors affecting the success of a constrained numerical optimization analysis. This factor needs to be verified carefully in order to ensure it covers every possible value of the parameter to be optimized. For parameter R, ABAQUS gives a very broad range for general powders and

He et. al. indicated R should be in the range of (0.07, 0.91) (He et al. 2001). In previous studies, parameter α varying from 0.01 to 0.05 was found to be common (He et al. 2001; Lee and Kim 2002, ABAQUS 2003; Wagle et al. 2003 , Gunningham et al. 2004) although arguments exist (Simo et al. 1985, Zeuch et al. 2001).

Setting α=0.01, a series of numerical simulations were made by applying different R values for ferrous powders using a cylindrical specimen. Other information about the FEA model is described in section 3.4. R was initiated as 0.01 (He et al. 2001, Lee and Kim 2002, ABAQUS 2003, Wagle et al. 2003 , Gunningham et al. 2004) and allows a larger coverage. With increases of R, the maximum (PEQC4 max) and minimum (PEQC4 min) value of plastic strain and the max real strain (PEMAG max) over the whole simulation model was investigated. The raw data of strains is listed in the following table, and simulated density distribution maps for different R's are plotted in Figure 48, 49, 50, and 51.

Table 7 Strain Results for R Values

R	PEQC4 max	PEQC4 min	PEMAG max
0.01	0.69	0.6887	0.562
0.05	0.6905	0.6885	0.5632
0.1	0.6917	0.6876	0.566
0.2	0.6959	0.6831	0.5752
0.3	0.7011	0.6759	0.5874
0.5	0.7097	0.6592	0.6195
0.7	0.7175	0.6442	0.6663
1	0.7326	0.6337	0.7687
1.2	0.7357	0.6346	0.8514
1.5	0.7407	0.6454	0.9934
1.7	0.7411	0.6513	1.096

2	0.7399	0.6577	1.254
2.2	0.7395	0.661	1.347
2.5	0.77	0.6595	1.399
2.7	0.871	0.6145	1.341

Figure 48 Plastic Strain Distribution at R=0.01

Figure 49 Plastic Strain Distribution at R=0.1

PEQC4
(Ave. Crit.: 100%)
-6.442e-01
-6.503e-01
-6.564e-01
-6.625e-01
-6.686e-01
-6.748e-01
-6.809e-01
-6.870e-01
-6.931e-01
-6.992e-01
-7.053e-01
-7.114e-01
-7.175e-01
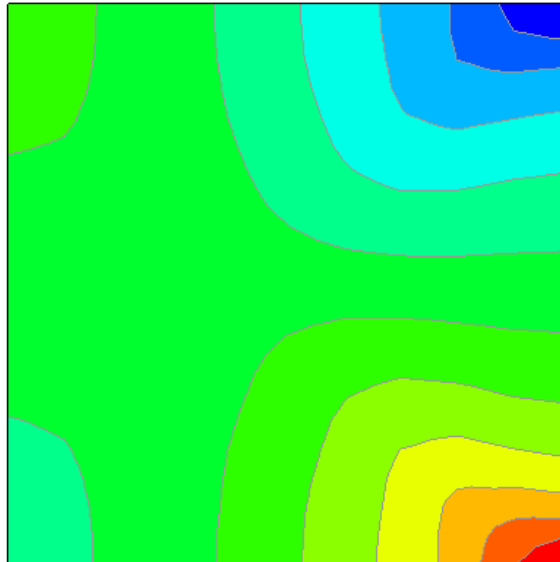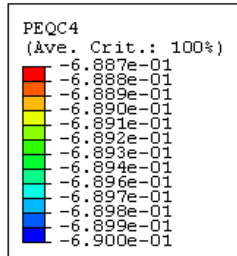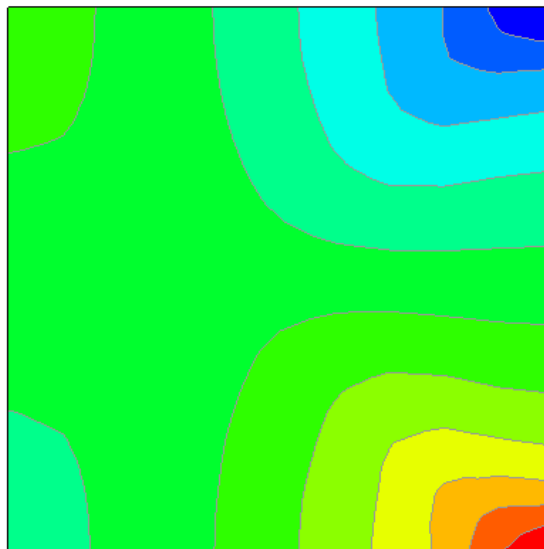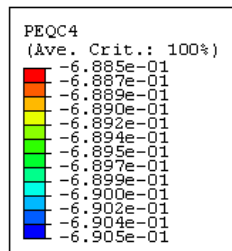
ODB: r70_f17_a01.odb   ABAQUS/Standard 6.4-1   Thu Jan 19 12:08:51 Central S
Step: Step-1
Increment   9: Step Time =   1.000
Primary Var: PEQC4
Deformed Var: U   Deformation Scale Factor: +1.000e+00
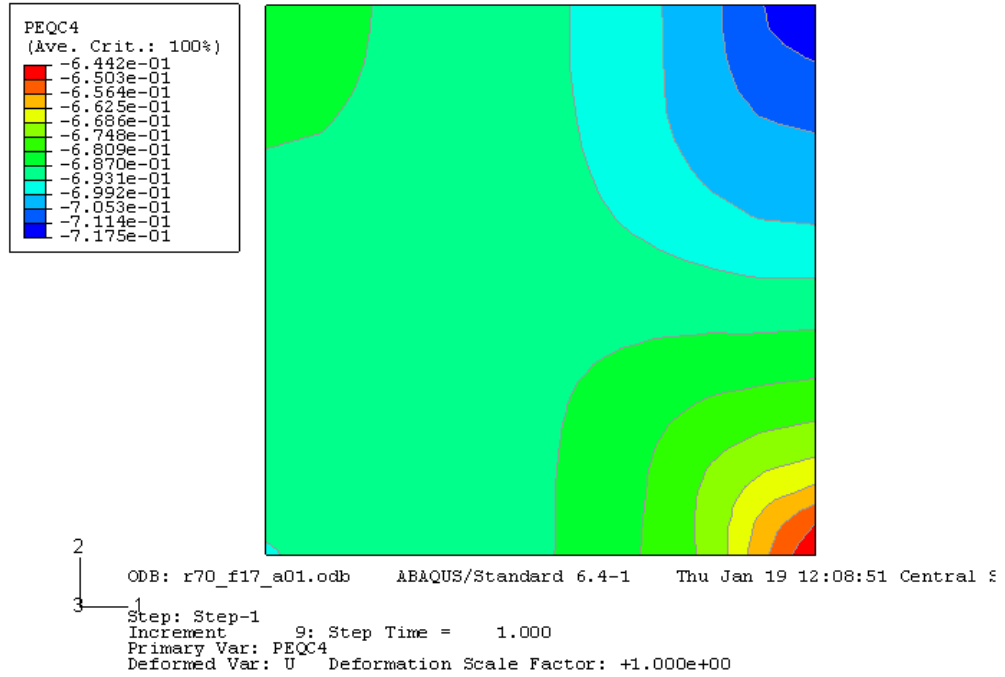
Figure 50 Plastic Strain Distribution at R=0.7

PEQC4
(Ave. Crit.: 100%)
-6.595e-01
-6.687e-01
-6.779e-01
-6.871e-01
-6.963e-01
-7.055e-01
-7.147e-01
-7.239e-01
-7.331e-01
-7.423e-01
-7.515e-01
-7.608e-01
-7.700e-01

ODB: rb5_f17_a01.odb   ABAQUS/Standard 6.4-1   Thu Jan 19 13:31:43 Central S
Step: Step-1
Increment   483: Step Time =   1.000
Primary Var: PEQC4
Deformed Var: U   Deformation Scale Factor: +1.000e+00
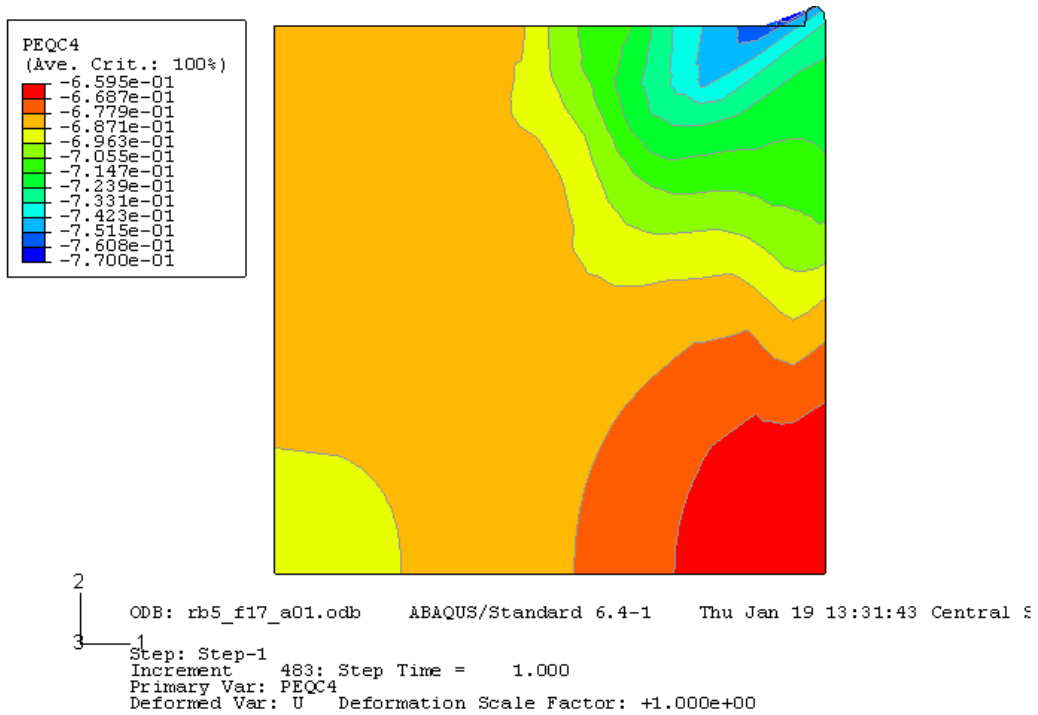
Figure 51 Plastic Strain Distribution at R=2.5

Strains are plotted in Figure 52. The difference of the plastic strains becomes greater with the increase of R until $R = 1$, at this point the difference becomes smaller. During this stage, the maximum plastic strain varies slowly, but the magnitude of strain increases rapidly. After $R = 2.0$, the strain difference becomes sharply larger again. The associated magnitude of strain of the sample keeps increasing until $R=2.5$, then it drops. At $R > 1.5$, the value of the magnitude of strain starts to become greater than 1.0, which is impossible according to the definition of true strain. So it can be concluded that the upper bound of R is 1.5, and the corresponding density for this R value is 7.2 g/cm^3 (92%). This result agrees with the fact that compressing ferrous powders to a higher density level (>90%) is very difficult by using a normal compaction technique.
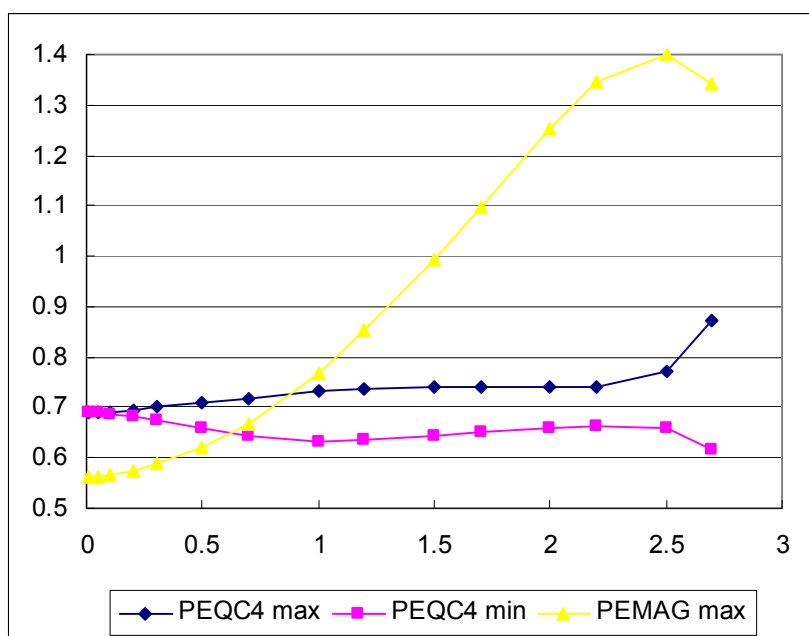
Figure 52 Strain Plots for R Values

The study of strains provides the upper bound for the search space of R for iron-based powders: the upper bound of R value is in the neighborhood of 1.5. When R is greater

than 1.5, the strain is greater than 1, and distorted elements start to appear at the right upper corner (see Figure 53).
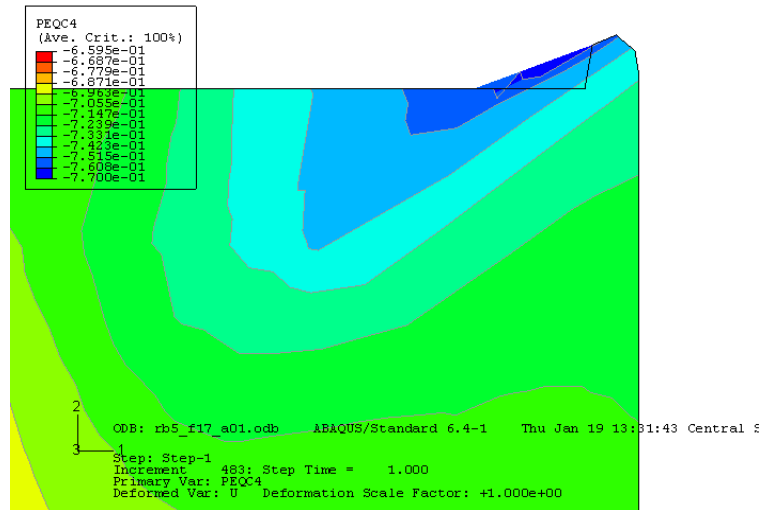
Figure 53 Distorted Elements at R=2.5

Using a similar method, the search space for α was examined. The following table and plots show the search space study results. Considering the fact that the maximum strain value increases from 0.7175 at $\alpha = 0.01$ to 0.7202 at $\alpha = 0.05$, the common selection of α (He et al. 2001; Lee and Kim 2002, ABAQUS 2003; Wagle et al. 2003 , Gunningham et al. 2004) makes a very weak contribution to the simulation. The simulation was expanded into a greater α value zone until the magnitude strain equaled to 1, when $\alpha = 0.22$. The results were plotted in Fatigue 54. Therefore, this space can be chosen as $\alpha = 0.01$ to $\alpha = 0.22$ which is different from that provided in the literature. R was chosen as 0.7 for this study. Further study of the determination of α will be beneficial to the numerical simulation method with a DPC model.

Table 8 Strain Results for α Values

α	PEQC4 max	PEQC4 min	PEMAG max
0.01	0.7175	0.6442	0.6663
0.02	0.7182	0.643	0.672
0.03	0.7188	0.6417	0.6781
0.04	0.7195	0.6405	0.6846
0.05	0.7202	0.6393	0.6916
0.07	0.7226	0.6378	0.7074
0.1	0.7281	0.6354	0.7391
0.15	0.7345	0.6337	0.808
0.2	0.7381	0.638	0.9135
0.25	0.74	0.6505	1.087
0.3	0.7383	0.6611	1.361
0.35	0.6246	0.4471	1.257
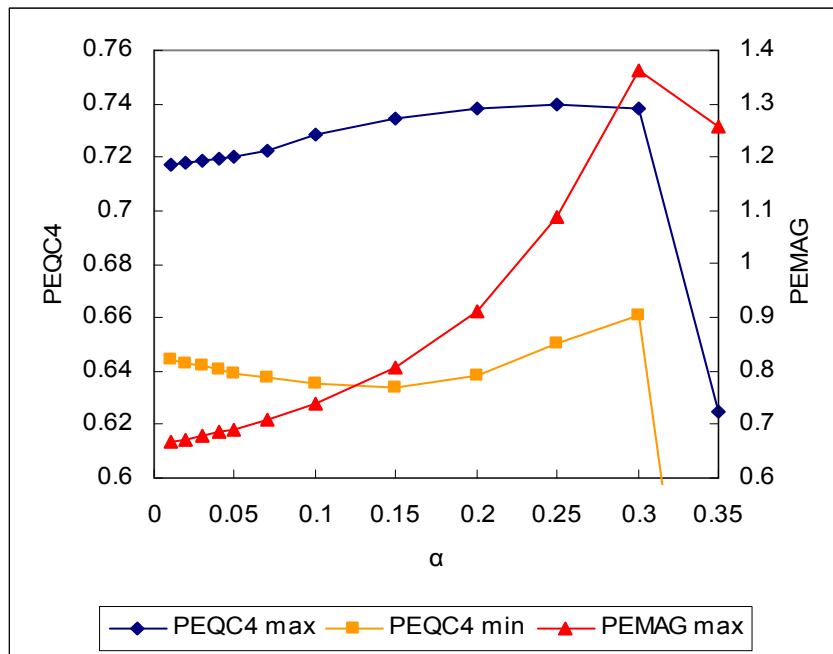
Figure 54 Strain Plots for α Values
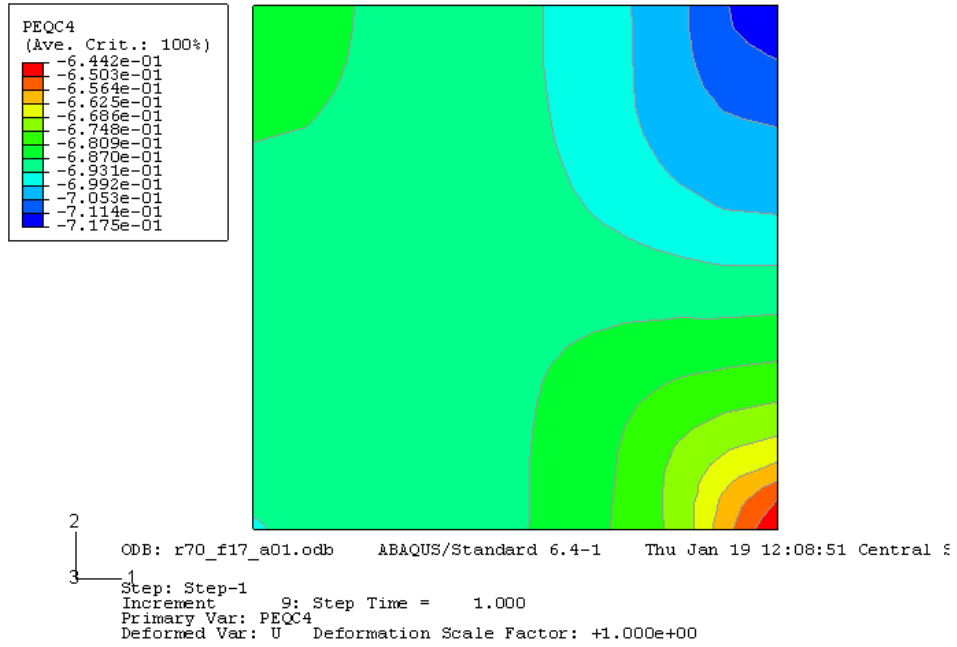
Figure 55 Plastic Strain Distribution at α=0.01
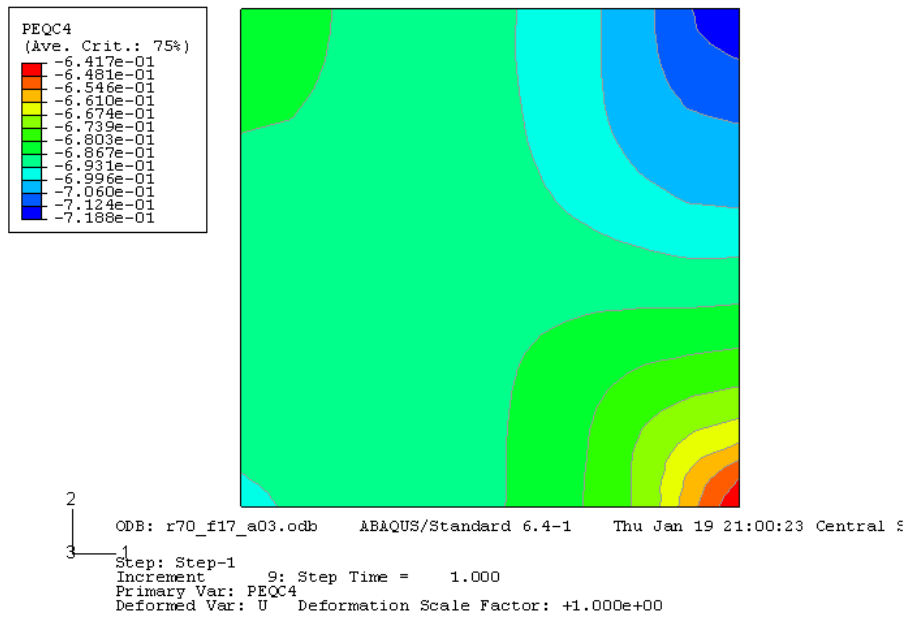
Figure 56 Plastic Strain Distribution at α=0.05

```
PEQC4
(Ave. Crit.: 75%)
  -4.471e-01
  -4.619e-01
  -4.767e-01
  -4.915e-01
  -5.063e-01
  -5.210e-01
  -5.358e-01
  -5.506e-01
  -5.654e-01
  -5.802e-01
  -5.950e-01
  -6.098e-01
  -6.246e-01
```

```
ODB: r70_f17_ac5.odb      ABAQUS/Standard 6.4-1      Thu Jan 19 22:19:22 Central S

Step: Step-1
Increment      658: Step Time =    0.8592
Primary Var: PEQC4
Deformed Var: U   Deformation Scale Factor: +1.000e+00
```
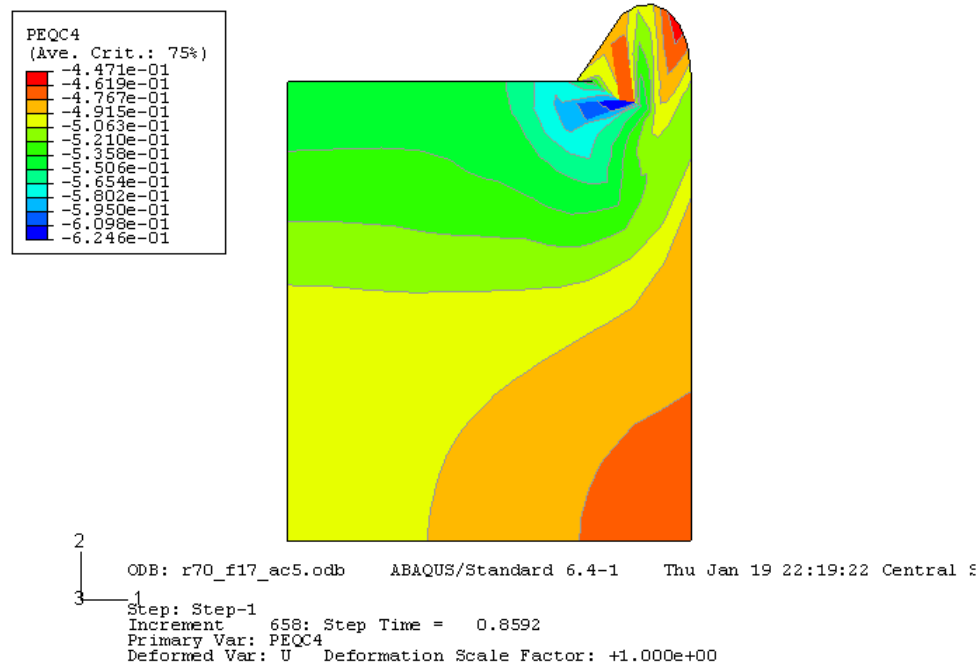
Figure 57 Plastic Strain Distribution at α=0.3

In summary, the searching space of *R* and *α* in this research will be defined as (0.01, 1.5) and (0.01, 0.22) respectively.

3.9   Response Surface Methodology

3.9.1   Overview

In this research, an unknown non-random function exists in the space of metal powder DPC parameters presenting the difference between the actual density map and the simulated density maps. The goal of this numerical optimization research for R and α can be classified as a maximization problem. One of the best known techniques to solve this kind of problem is response surface methodology (Meketon 1987).

Response Surface Methodology (also known as RSM) is an optimization tool that was introduced in the early 1950´s by Box and Wilson (Box and Wilson 1951). The RSM is a collection of statistical and mathematical techniques useful for developing, improving, and optimizing processes. The most extensive applications of the RSM are in the situations where several input variables potentially influence quality characteristic of the process, such as the experimental strategy to explore the space of the process, empirical statistical modeling to develop an approximating relationship between the yield and the input, and optimization methods to find values of the process variables that produce desirable values of the response (Nicolai et al. 2004). The input variables are called independent variables. The quality characteristic is called the response surface. Metamodeling techniques have attracted intensive attention in the RSM implementation. Due to computation-intensive processes for numerical simulation, this approach approximates complexities with simple analytical models (Wang and Shan, 2007). The simple model is often called a metamodel; and the process of constructing a metamodel is called metamodeling. The response surface is used to determine a search strategy (e.g., moving in the estimated gradient direction) and the process is repeated until an optimum is reached. The following sketch illustrates this algorithm.
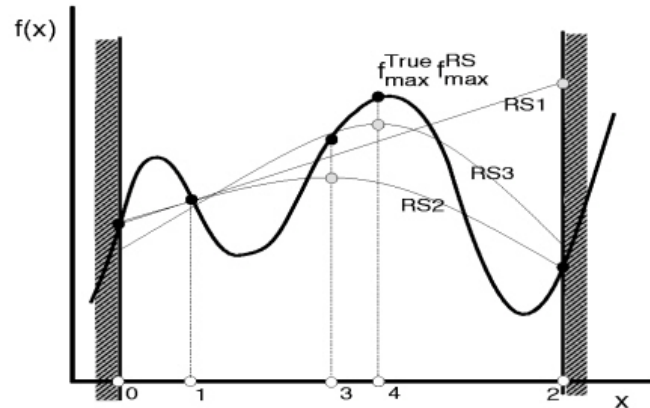
Figure 58 Schematic Overview of Response Surface Methodology

Figure 59 graphically shows a response surface between the density measure (correlation coefficient) and cap model parameters (R and α).
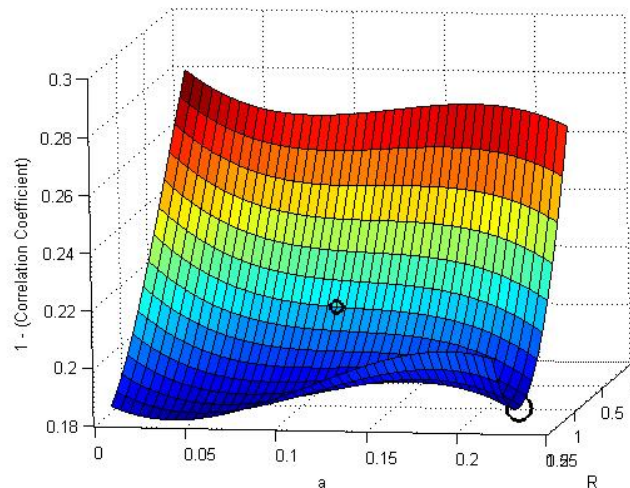
Figure 59 Response Surface

A maximization task aims to find the input parameters that produce the maximum output value. For this research, the aim is to find a set of the metal powder DPC material properties that lead to the maximum correlation coefficient between the actual density map and the simulated density maps. Mathematically, response surface methodology for a maximization problem within space $\Re$ can be described by the following equation:

$$\max f : D \to \Re, D \subseteq \Re^{k} \qquad \text{Equation 28}$$

where e $f(\xi 1,...,\xi k)$ is equal to $E(F((\xi 1,...,\xi k))$. Here, $F((\xi 1,...,\xi k)$ is output for given input $\{\xi 1,...,\xi k\}$, and $E(F((\xi 1,...,\xi k))$ denotes its expected value. This situation is typical in numerical simulation studies, where the objective function can be seen as a black box. Simulation models do not assume a function form and are subject to an unknown stochastic error(Joshi et al. 1998, Nicolai et al. 2004).

In general, a RSM procedure includes two phases. In the first phase, the objective function is locally approximated by first-order polynomials; in the second phase, the objective function is approximated by a second-order polynomial (Dean 1999). In both phases a sub-region of the search domain is defined. In the approximation procedure, the objective function is evaluated a number of times. The evaluations produce a specific arrangement of the points that usually lie on the borders of the region of interest. When the first-order model is found to be adequate a steepest descent procedure is applied to find a new region of interest. Otherwise the RSM moves to the second phase. When a second-order model is approximated and found to be adequate a stationary point needs to be found and classified and an appropriate action should be taken. Usually the algorithm is terminated and the stationary point is returned.

A number of strategies need to be implemented in an automated RSM procedure using a consistent decision rule. These strategies can be divided into building blocks, strategic moves and stopping rules of the algorithm. The building blocks consist of well-defined procedures that can be used to determine the next move of the algorithm.

Strategic moves determine the action taken when a building block returns a result. The

stopping rules for the first and second phase are normally the same. The following flow

chart shows the response surface methodology.
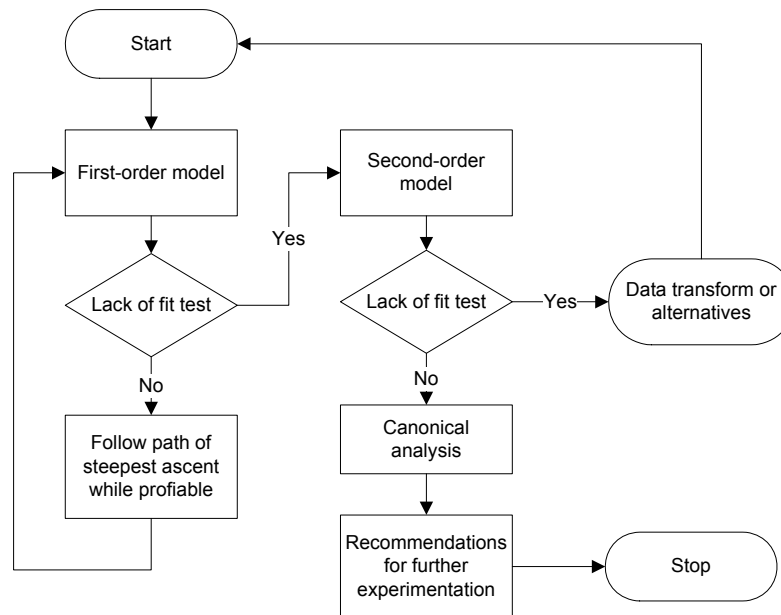
Figure 60 Flow chart for Response Surface methodology

3.9.2 Building Blocks (First-order and Second-order Model Design)

The general response surface model is of the form

$$Y(x) = \eta(x) + \varepsilon(x)$$

Equation 29

where $x = (x_1, x_2, \ldots, x_n)$ presents independent variables, $\eta(x)$ is the mean response,

and $\varepsilon(x)$ is a random error variable.

The goal of obtaining a response surface is to locate x for which the mean response is

maximized. Before the peak of the response is reached, a small local experiment is

normally conducted to detect if it is in the vicinity of the peak. A first-order polynomial

regression model is created if a negative result is returned. Also, the analysis of variance

(ANOVA) normally conducted to identify which variable is significant to the output. A

standard first-order model can be presented as

$$Y(x) = \beta_0 + \beta_1 x_1 + ... + \beta_n x_n + \varepsilon_x \qquad \text{Equation 30}$$

where β_i is a measure of the local linear effect of the ith factor x_i, and the error

variable is assumed to be independent with $N(0, \sigma^2)$ distributions (Myers and

Montgomery 1995, Dean 1999). The least square estimation can be used to establish a

first-order model. The response surface can be fitted in the least square format

$$\hat{y}_x = \hat{\beta} + \hat{\beta}_1 x_1 + ... + \hat{\beta}_n x_n \qquad \text{Equation 31}$$

where $\hat{y}$ is the predicted values.

A successful first-order design should allow an efficient estimation of linear effect β_i

and Y(x) and be expandable to a second-order design. There exist several kinds of

designs to build the first-order model for a RSM procedure, for instance, fractional or full

factorial, and two-level or three-level designs (Myers and Montgomery 1995). All

designs can be augmented by the center point of the region of interest (Sacks et. al. 1989,

Dean 1999).

Usually, a test for lack of fit and a test for significance of regression are performed to

test the adequacy of the first-order model. There are a number of different measures of

model accuracy (Jin et. al. 2001). The first three are the root mean square error, RMSE,

the maximum absolute error, MAX, and the R square value defined as

$$RMSE = \sqrt{\frac{\sum\limits_{i=1}^{m}\left(y_i - \hat{y}_i\right)^2}{m}}$$ Equation 32

$$MAX = \max\left|y_i - \hat{y}_i\right|, i = 1,...,m$$ Equation 33

$$R^2 = 1 - \frac{\sum\limits_{i=1}^{m}\left(y_i - \hat{y}_i\right)^2}{\sum\limits_{i=1}^{m}\left(y_i - \bar{y}_i\right)^2}$$ Equation 34

where is the mean of the observed values at the validation points.

If all of these two tests are passed, the line search will be performed. Otherwise, a second order model is needed. A line search starts from the center point of the current interest region in the steepest descent direction to find a point of improved response (Neddermeijer et al. 1999, Kleijnen et al. 2002). In automated optimization, a stopping rule determining the lack of improvement in response is required.

Second-order designs and analysis are required when the lack of fit test of the first-order model indicates the vicinity of peak response is reached and a second-order model should be fitted. The general format of a second-order model is

$$Y(x) = \beta_0 + \sum_{i=1}^{n}\beta_i x_i + \sum_{i=1}^{n}\beta_{ii} x_i^2 + \sum_{i<j}^{n}\beta_{ij} x_i x_j + \varepsilon_x$$ Equation 35

The central composite design (CCD) is one of most popular second-order model designs (Sacks et. al. 1989). The CCD is applied when the full or fractional factorial design is

augmented by the first-order design with $2k$ axial points (Dean 1999, Neddermeijer et al. 1999). Similar to the first-order model, a lack of fit test is necessary.

One additional analysis for a second-order design is the canonical analysis to determine the location of the stationary point (section 3.9.3). If the combination of x = (x_1, x_2, …, x_n) is treated as a point, in the n-dimension x space, the stationary point x_s = (x_{s1}, x_{s2}, …, x_{sn}) is the origin of a new coordinate system. In terms of each of these coordinate systems, the fitted model has the following equivalent representations,

$$\hat{y}_x = \hat{\beta}_0 + \sum_{i=1}^{n} \hat{\beta}_i x_i + \sum_{i=1}^{n} \hat{\beta}_{ii} x_i^2 + \sum_{i\langle j}^{n} \hat{\beta}_{ij} x_i x_j$$

$$\hat{y}_v = \hat{y}_{vs} + \sum_{i=1}^{n} \hat{\beta}_{ii} v_i^2 + \sum_{i\langle j}^{n} \hat{\beta}_{ij} v_i v_j$$

$$\hat{y}_w = \hat{y}_{ws} + \sum_{i=1}^{n} \hat{\lambda}_{ii} w_i^2 \qquad\qquad \text{Equation 36}$$

Equation 36 is called in canonical form. To obtain it, two transforms are required. The first one is to move the coordinate system origin to the stationary point by applying v = x - x_s. This eliminates the linear terms in the fitted model. The second transform is to rotate the coordinate system to eliminate the cross product terms.

The canonical analysis determines if the stationary point is a maximum, minimum, or saddle point for the strategic move rules.

3.9.3 Strategic Moves

If the first-order model is found adequate, a steepest descent procedure will be applied from the current center to find a new center point (Joshi et al. 1998). This new point is then used as the center point of the next region of interest. And the new objective function will be a first-order model again. If the first-order model is not accepted, literature (Sacks et. al. 1989, Myers and Montgomery 1995, Dean 1999) suggests the response surface function will be a second-order model since a first-order model with a higher precision is time consuming and does not guarantee the adequacy of the model.

For an acceptable second-order approximation, Greenwood et al. determined that the first stationary point is not likely to be the best point in the domain of interest (Greenwood et al. 1998). If a minimum is found inside the region of interest, this point can be used as the center of a new design and a new second order approximation can be performed. If the stationary point of the second-order polynomial is a maximum, a saddle point or a minimum outside the current region of interest is required to find a new stationary point.

The most common reason that a second-order model is found to be inadequate is the region of interest is too broad (Greenwood et al. 1998). By increasing the precision used in evaluating a design point, the variance of the response will be reduced and therefore the second-order polynomial will model the objective function better.

3.9.4   Stopping Rules

Generally, in an automated optimization procedure, the RSM algorithm needs to be ended by consistent stopping rules. Based upon the literature, the optimization ends when either the estimated response value does not improve sufficiently, or when a fixed maximum number of evaluations have been reached (Meketon 1987, Greenwood et al. 1998, Kleijnen et al. 2002, Nicolai et al. 2004).

3.10 Searching for R and α using HyperStudy

The density difference was used to describe the similarity between the actual density map and the simulated density maps in terms of R and α in this study. Each simulated density map has an overall density difference measure. Since the relative density is playing a more important role than the absolute density value in this research, the correlation coefficient between the two density maps will be a good measure of the density difference. Two density vectors, one from the simulated density map and another from the actual density map, containing local densities at certain spots will be needed to calculate the correlation coefficient between these two maps. After the density difference measures were established, the proper numerical optimization methods, such as the sequence response surface method, can be applied to this function in order to obtain a set of R and α for a minimum difference value between the simulated density map and the measured density map. This optimization process was implemented by HyperStudy (HyperStudy 2006).

3.10.1 Brief Introduction to HyperStudy

HyperWorks by Altair Engineering integrates modeling, assembly, robust design, optimization, design analysis, visualization, reporting, virtual manufacturing, automation, and data management into an engineering framework for maximizing product performance, automating processes and improving profitability.
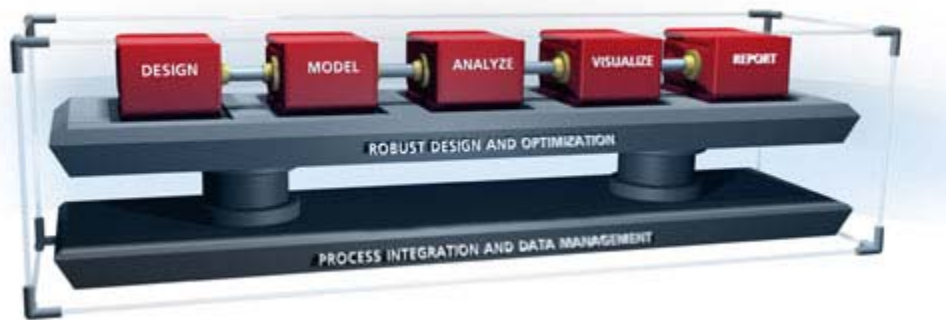
Figure 61 Engineering Framework of HyperWorks

HyperStudy is among the most important components of HyperWork. Parameter searching is one of the three numerical optimization built-in algorithms. HyperStudy utilizes the response surface methodology to complete a parameter searching task (HyperStudy 2006). HyperStudy provides interfaces to most common commercial FE software including ABAQUS for optimization tasks. A script file (*.TPL file) defines the parameters to be optimized and a particular portion of FEA results to transfer into HyperStudy. After the original FEA is run, the numerical optimization process starts automatically. The new value of parameters generated by HyperStudy is then passed to

ABAQUS for a new run of FEA. This process repeats until the optimized parameters are found.

Design Analysis
(ABAQUS)

Analysis Results
(nodal, elemental results, etc.)

Built-in Interface

Design Update
Optimization

Response Surface
Computation
(HyperStudy)

Update Parameters
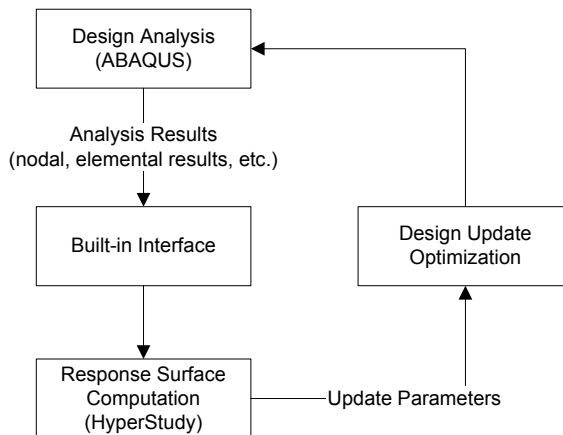
Figure 62 Flowchart of Data between ABAQUS and HyperStudy

3.10.2 User-defined ABAQUS Interface

Data flows between ABAQUS and HyperStudy to accomplish a parameter search through an interface provided by HyperStudy. The built-in interface handles most of the ABAQUS results, such as the geometry, the nodal and elemental information, the stress, the strain, and the displacement (HyperStudy 2006). But the HyperStudy interface does not allow a user to access the PEQC information. The only way to make the automation process happen is to generate a text file containing the PEQC information for HyperStudy parameter search procedures outside HyperStudy. Therefore, a user-defined interface is required.

The interface was programmed in Microsoft Visual C++. It is an executable file and is able to be referenced by HyperStudy. The interface provides two main functions: to

read the PEQC information from the ABAQUS output files for the specified nodes and elements; and to calculate the correlation coefficient between the measured density map and the current FEA density map for the HyperStudy parameter research process to read.

In ABAQUS, the PEQC output presents equivalent plastic strains for the Drucker-Prager cap model in the format: the shear failure surface - PEQC1, the cap surface - PEQC2, the transition surface - PEQC3, and the total volumetric plastic strain - PEQC4. When PEQCs are requested as one of the outputs in the database, the active yield flags for each component are named AC YIELD1, AC YIELD2, etc. The PEQC results are written in a *.ODB file as well as a *.DAT file with the element number and the coordinates of the element center. The *.DAT is an ASCII file and is convenient to read. The format of the PEQC strain is listed below. The section requesting PEQC output in the ABAQUS input file and a portion of PEQC results in the *.DAT file for one of the compaction simulation can be found below (ABAQUS 2003).

Table 9 Section Requesting PEQC Output

```
** FIELD OUTPUT: F-Output-2
**
*Output, field, frequency=99999
*Element Output
PEQC,
*El Print, elset=powder, FREQUENCY=99999
COORD, PEQC4,
```

Table 10 Example of PEQC Results

ELEMENT	PT FOOT-NOTE	COORD1	COORD2	PEQC4
122	1	0.5899	-0.2744	-0.9277
123	1	0.6172	-0.2899	-0.7662
124	1	0.6455	-0.3024	-0.7239

The *.DAT file was accessed by the user-defined interface program so that the PEQC4 plastic strain information for the elements inside the cross section of the metal powder compact was compared with the information from the corresponding location in the measured density map. So by creating two arrays containing the local density information from the FEA density map and the measured density map respectively for the same location, the correlation coefficient between the two density maps can be calculated.

3.10.3 Density Measure (Correlation Coefficient)

In statistics, the correlation coefficient, also know as the product-moment coefficient of correlation or Pearson's correlation, is a quantity indicating the strength and direction of a linear relationship between two random variables (Wilcox 2003). For a series of n measurements of X and Y written as x_i and y_i, the correlation coefficient is defined as

$$r = \frac{\sum \left(x_i - \bar{x} \right) \left(y_i - \bar{y} \right)}{(n-1)\sigma_x \sigma_y} = \frac{n \sum xy - \left(\sum x \right)\left(\sum y \right)}{\sqrt{\left[n \sum x^2 - \left(\sum x \right)^2 \right]}\sqrt{\left[n \sum y^2 - \left(\sum y \right)^2 \right]}} \qquad \text{Equation 37}$$

where $\bar{x}$ and $\bar{y}$ are the means of x and y, σ_x and σ_y are the standard deviations of x and y.

The correlation coefficient, donated by r, is a dimensionless quantity, and ranges from −1 to +1. A positive value of r indicates the variable y has the same trend with the variable x when it varies, while a negative values indicates an opposite direction exists when x and y change. A perfect correlation of +1 occurs when all data points of x and y

lies exactly on a straight line, and a value near zero means that there is a random or non

relationship between the two variables. The correlation coefficient reflects the strength of

the linear relationship. Generally, a correlation coefficient greater than 0.8 is considered

as strong, while the one less than 0.5 is described as weak (Lomax 2007). The following

pictures visualize the correlation coefficient and the responding variables.
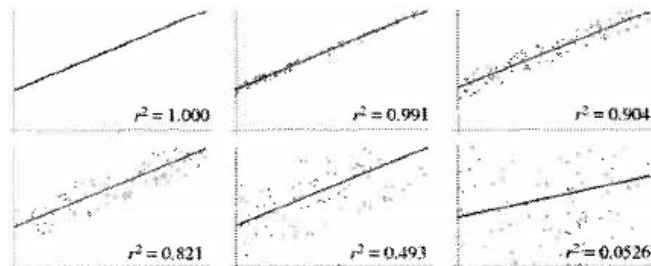
Figure 63 Correlation Coefficient Visualization

In this research, the correlation coefficient between the measured density map and the

simulated density map was calculated and used as the stopping rule for the optimization

process.

3.10.4 Defining Optimization Task

To perform a HyperStudy optimization process, a templex file needs to be generated

according to the ABAQUS input file to specify the parameters for the particular

optimization task (HyperStudy 2006). The file extension is *.TPL. This can be done

either through the HyperStudy GUI or by editing the ABAQUS input file manually. The

following screenshot shows the dialog to define search parameters.
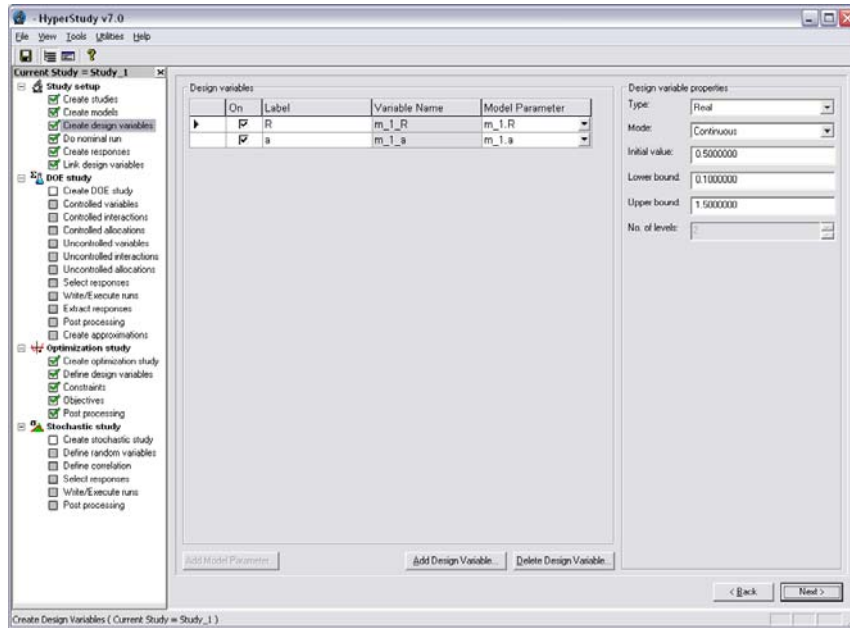
Figure 64 Defining Search Parameters

Two changes are made by HyperStudy in the ABAQUS input file: the header and the section where the value of the search parameters are defined. The templex file contains a file header in front of the ABAQUS file describing the searching parameter information. For defining R and α as the parameter to search, the search space and the initial value for each parameter are required. The initial value for R was set to 0.1 and the initial α was 0.05. The search space for R and α was (0.01, 1.5) and (0.01, 0.22) respectively as described in the previous chapter. The header of the template file for this research and the modification of the ABAQUS input file are shown below.

```
{parameter(R,"R", 0.5, 0.1, 1.5)}
{parameter(a,"a", 0.05, 0.01, 0.22)}
```

The following lines shows the original section of the ABAQUS input file defining the cap shape parameter and the transition parameter,

```
*Cap Plasticity
 2.5,  72.,  0.5,  0.1, 0.05,   0.
```

And the following lines show the other modification by HyperStudy when the

parameters are called:

```
*Cap Plasticity
 2.5,  72., {R, %8.5f},  0.1, {a, %8.5f},   0.
```

The ABAQUS running environment was setup in HyperStudy for the automated

parameter search process. Before the numerical optimization started, ABAQUS was

referenced for a nominal run which provides the original response by initial values of the

search parameters. The purpose of this research is to find a set of parameters minimizing

the difference between the actual density map and the FEA density map. So the search

target for this HyperStudy task was defined as to maximize the correlation coefficient,

and the constraint condition was defined as to minimize the residuals sum of square that

was calculated by the user-defined interface as well as the correlation coefficient.
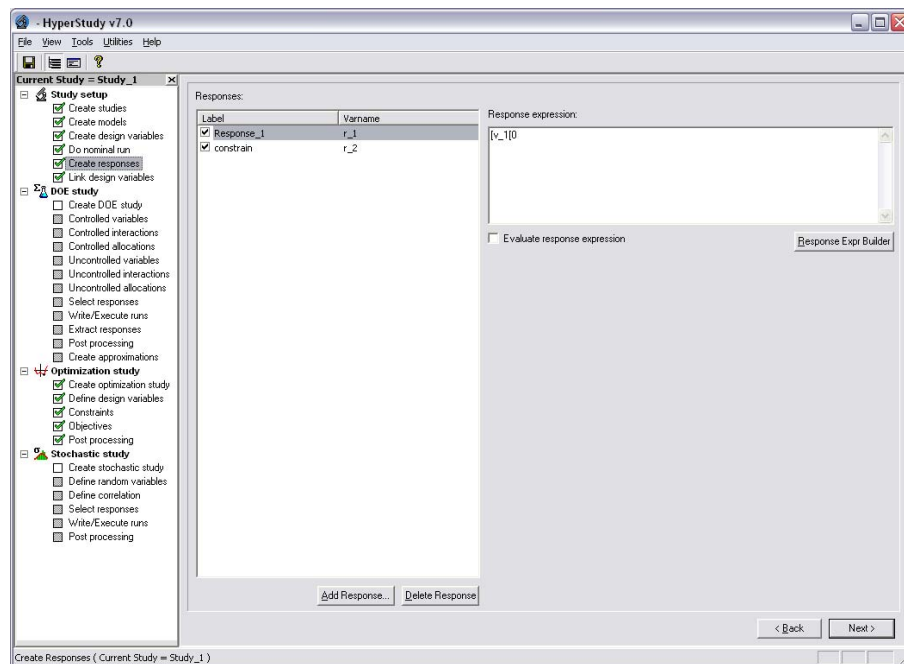
Figure 65 Defining Responds and Constraint

The input file, file extension *.STDY, for a HyperStudy optimization task is a set of

macros defining the characteristics of the research: the working directory; the

HyperStudy templex file; the ABAQUS input file; the search parameters; the search

space of the parameters; the stopping rule of the search(targets and constrain conditions);

and the optimization algorithm applied. The example of the HyperStudy input file is

listed in Appendix D.

The optimization starts with the initial values of the searching parameters defined in

the HyperStudy input file. In HyperStudy, this is called a nominal run which provides an

original response for the optimization process. This is a parameter search then determined

the search path by selecting the next set of values of the parameters based on the response

from the nominal run by the built-in numerical optimization algorithms. The process was

repeated until the maximum correlation coefficient was reached. This process was

automated by the use of the batch files described in the next chapter.

3.10.5 Batch File for Automated Parameter Search Procedure

Three batch files were created to perform the optimization task in HyperStudy for the

DPC parameter search. The files were Abaqus_Running.bat, Abaqus_txt.bat, and

Abaqus_Batchrun.bat respectively.

Abaqus_Batchrun.bat

Call c:\cong\hyperStudy\Abaqus_Running.bat
call c:\cong\hyperStudy\Abaqus_txt.bat

Abaqus_Running.bat

call dfvars.bat
abaqus job=ringfinal user=c:\cong\hyperstudy\strain int

Abaqus_txt.bat

"c:\cong\hyperStudy\peqc.exe"

The purpose of these three files can be summarized below:

Table 11 Purpose of Batch Files

File Name	Purpose
Abaqus_Batchrun.bat	Call other batch files
Abaqus_Running.bat	Set up the environment variables for HyperStudy and create the ABAQUS input file for irritations of the parameter search
Abaqus_txt.bat	Call the user-defined interface to obtain the PEQCs and compare the latest FEA density map and the actual density map

In general, a typical HyperStudy optimization task only requires the second batch. The third batch file was utilized in this research because HyperStudy does not provide a method to acquire the PEQC information from an ABQUS output file. So a user-defined ABAQUS interface transferring the PEQCs into ABAQUS was invoked as discussed in the previous sections. By running all three batch files, an automatic numerical optimization procedure is developed. Four steps were invoked: the creation of the simulated density map by ABAQUS, the transportation of the PEQC information by the user-defined interface, the comparison of the simulated density map and the actual

density map, and the numerical optimization by HyperStudy. The procedure will keep running until the optimum set of the parameters is found.

3.10.6 Results of (R, α) Search for FLC2-4808 Powders

Figure 66 visualizes the numerical optimization process:

1. The correlation coefficient was low with the initial guess of the parameters;

2. The built-in HyperStudy numerical optimization algorithm adjusted the values of the parameters to determine a global search path;

3. Along with the determined search path, the correlation coefficient reached its peak value quickly with a parameter increment calculated by HyperStudy;

4. HyperStudy reduced the increment interval of the parameters to refine the search in the adjacent area;

5. The refined search showed a close correlation coefficient with the peak value, so according to the stop criteria defined in the input file, the numerical optimization stopped with an optimized set of the R and α.
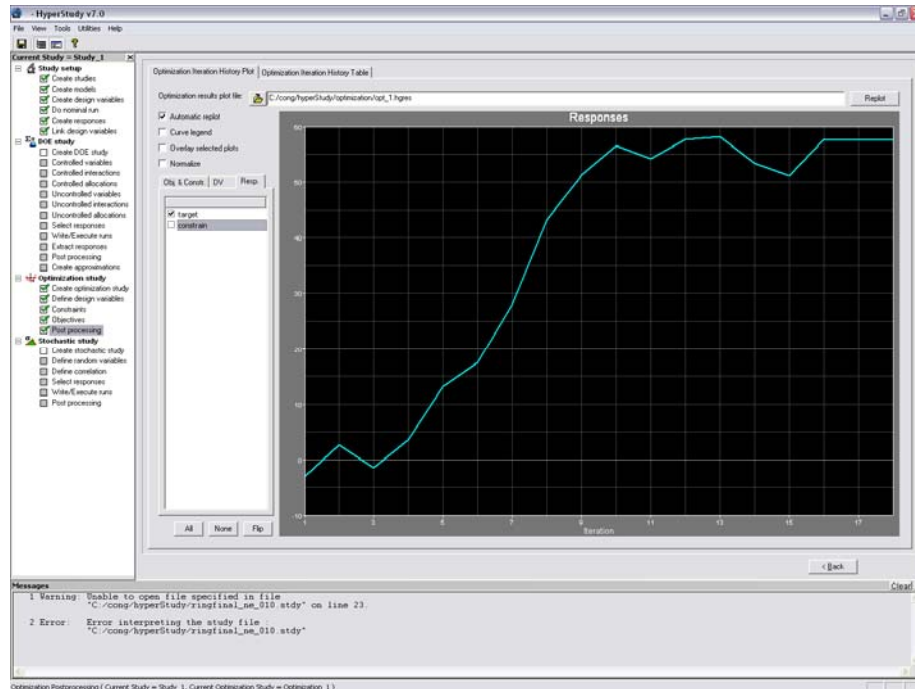
Figure 66 Visualization of Parameter Search

By following the procedure described above, the parameter search for R and α converged after 16 iterations. The initial value of R and α was 0.3 and 0.05, the search space was (0.01, 1.5) and (0.01, 0.22). The optimum R and α were determined as (0.88, 0.09) to provide the maximum correlation coefficient and the minimum SSR between the actual density map and the FEA density map. The correlation coefficient varied from 40.98% to 77.91% while the SSR decreased from 0.275 to 0.167 during the search. Utilizing this set of R and α in the FEA model, the FEA density map is obtained as shown below. The map delivered the local densities in the zone discussed in section 3.7.2 and was compared to the measured density map.
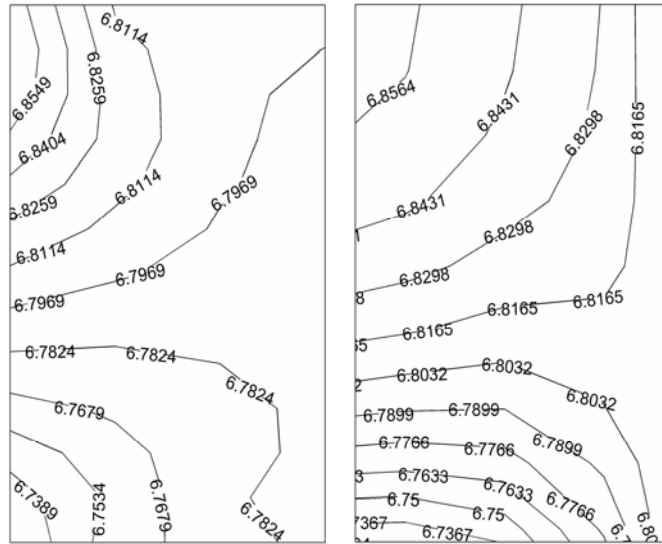
Figure 67 FEA and Actual Density Maps

By applying optimized R and α, the FEA density map shows a good similarity to the actual density map. This is indicated by the correlation coefficient between these two maps. The eccentricity parameter R presents an agreement with the values for ferrous powders in the prior literature. As mentioned in previous chapter, the transition parameter α is selected as 0.01 in previous publications. The value of α by this research is seen to be larger than that which is typically used. The larger value of α implies that the transition between powder shear surface and plastic deformation surface in the cap model may play a larger role in densification modeling than recorded by previous research.

The measured density map is presented as a curve fit of a 4th order polynomial. Higher order curves did not increase the accuracy of the procedure as mentioned before.

Chapter 4   VERIFICATION OF R AND α

To confirm the independency of the DPC model parameters predict by the proposed method, verification was done by applying the value of R and α obtained from the simple ring specimen to a green compact with a more complex geometry.

4.1   Sample Preparation

This multistage green compact was made from the same ferrous powders (FLC2-4808) as the ring sample used before. Figure 68, 69, and 70 present the dimensions of the part and the 3D view of the part before and after compression. The part was pressed by uniaxial compression, and was pre-sintered at 1350˚F for ten minutes in a furnace for the purpose of the local density measurement. The filling density of the part is 3.2 g/cm^3, and the green density is roughly 6.8 g/cm^3.

Figure 68 Dimensions of Main Body

Figure 69 3D View of Powders before Compaction
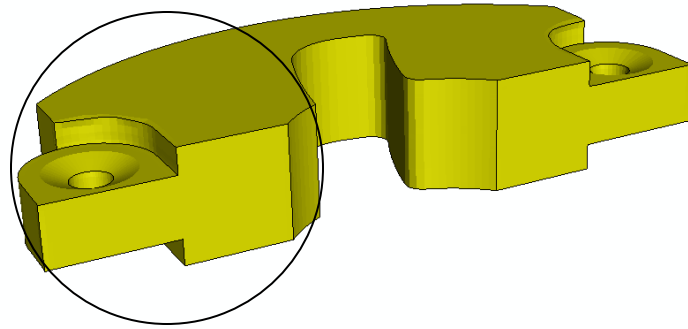
Figure 70 3D View of Sample after Compaction

To produce a part like this, four punches were utilized due to the multiple levels the product has. The lower punch set contains 3 punches and the upper punch set contains one. The punches contour the main body and the two "ears" of the part. The height of the "ear" portion powders and the vertical travel distance of the punches were designed carefully to ensure a relative uniform density distribution in the green part. The overall compression ratio is 2.1, which means the initial height of powders in both the body portion and the ear portions are 2.1 times of the finial height of these portions. So, the travel distances of each individual punch were not identical to complete the final dimensions for a relatively uniform density distribution. In the FEA calculations, the punches and the die were modeled as rigid bodies by defining "constraints" in ABAQUS, and these movements were applied as the boundary conditions. The punches and the die are shown below.
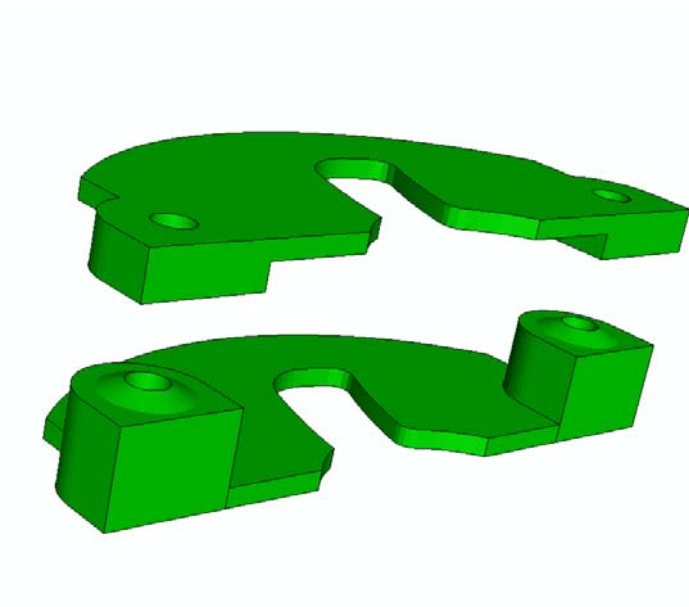
Figure 71 3D View of Punches

Figure 72 3D View of Die

4.2   Green Density Measurement

The specimen preparation process for this specimen was almost identical with the process for the ring sample. The only issue that needs to be mentioned is the cutting process. Due to the non-symmetric and complex geometry, a more accurate cutting procedure was required. So a Struers Accutom-50 automatic precision cut-off machine was applied. A thorough cut was made along the line connecting the centers of the hole in "ear" parts. The left-hand section (circled area in Figure 70) was used to measure the local density map and was compared to the simulated density map. A 3D view and a photo illustrating the measured crossed section are shown below. The specimen was edge enforced using the Buehler EdgeMet Kit before being mounted by the Buehler Epo-Thin epoxy solution. 0.1μm and 0.05μm Aluminum polishing powders were used for 30 seconds each to polish the specimen.

Figure 73 Struers Accutom-50 Accurate Cutting Saw
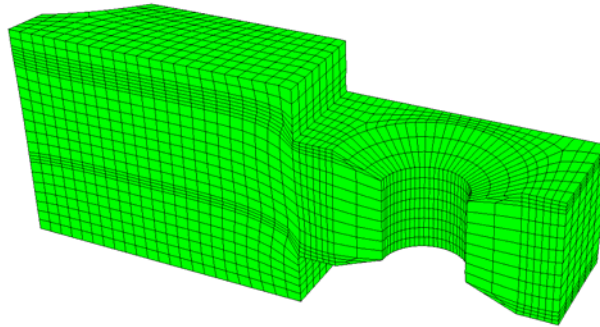
Figure 74 Measured Cross-Section

4.3   Actual Density Map

The setup of the photography acquisition equipment detailed in section 3.7 was used to take pictures for image analysis. The local density map was measured over the cross section of the part. The edge enforcement process was confirmed to be successful by the photos, as shown below. The metal coating is visible along the edges of the specimen in the images.
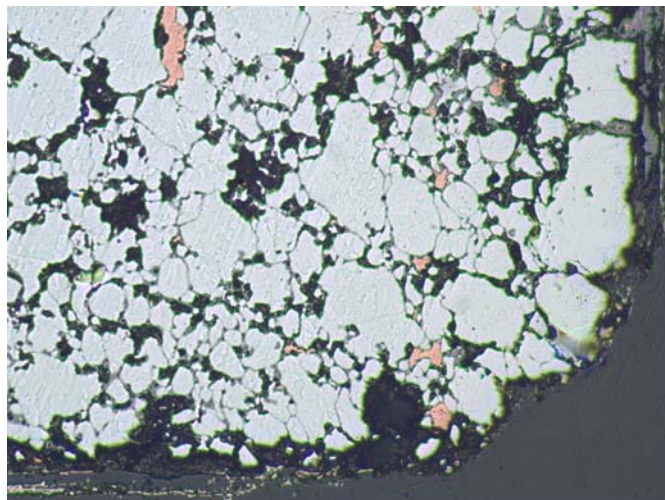
Figure 75 Metal Coating by Edge Enforcement

The edge and corner areas still produced a less quality measurement, like the ring sample due to the physical damage of the part. From the above picture, it was noticed that the metal coating was apart from the sample body. This picture represents a corner of the compact. The low strength of the sample results in much damage during the grinding and polishing process. Transportation of the specimen from the factory to the laboratory before the sintering process could contribute to the damage as well. To obtain an accurate density map without the effect of the edge damage, the photos adjacent to the edges, one column of photos from the vertical edges and two rows of photos form the horizontal edges, were excluded in the procedure of the density map measurement. The dimensions of each photo are 0.50mm x 0.65mm (0.02in. x 0.026in.). Totally, 100 photos were used to create the actual density map.

Three specimens were measured using the image analysis method. The contrast for red, yellow, and blue was set as 180, 255, and 255 in simplePCI since this configuration had been adopted in the density measurement for the ring sample in this research. The actual density map was generated according to the image analysis method data. The density map data came from the average of three specimens. A MatLab program was written to analyze the raw data and plot the actual density map over the three zones. The 4th order polynomial equation was adopted to perform the linear regression. This order polynomial equation had been used in the density measurement for the ring sample. The details of the program can be found in the appendix. The actual density map is plotted below.
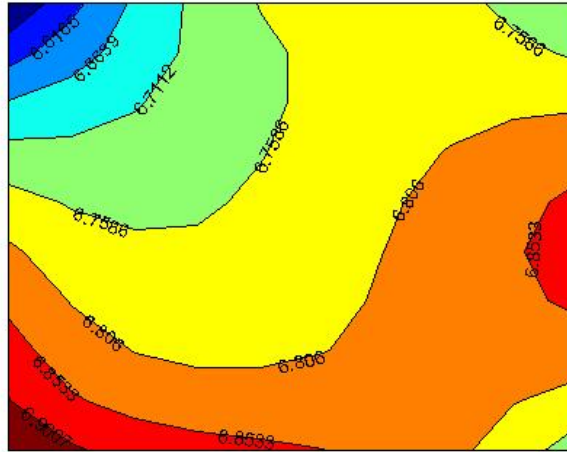
Figure 76 Actual Density Map, Verification

4.4   Simulated Density Map

Due to the non-symmetric geometry, the whole compact was modeled by solid

elements. To observe principal stress flows inside the green parts, the brick element was

selected. So the green compact was meshed by 3D stress solid elements (C3D8R). This is

a hex element with 8 nodes for finite element analysis. The total number of elements in

the model was 58358. The meshing technique was a mixture of "sweep" and "structured"

to ensure the use of the hex element for the visualization of local stresses. The typical

element size of the mesh was 0.5 mm (0.02 inches) according to dimensions of the

sample and the photo. But in some certain areas, for instance the joint area of the wings

and the main body, the mesh was finer to allow a larger displacement, and therefore, a

more accurate FEA result. The following screenshot shows the reduced elements size.
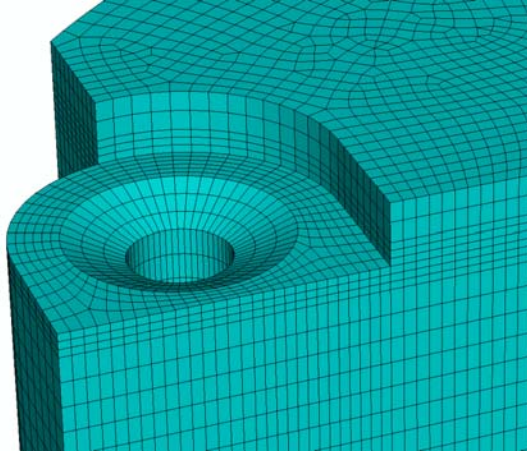
Figure 77 Areas with Fine Meshes

The ABAQUS "Interaction" defines how adjacent surfaces behave. In order to do so, the surfaces are defined in ABAQUS. This can be achieved by picking the desired face/faces of the solid model and make them a surface. In this simulation, 18 surfaces and 9 interactions were created. For instance, Figure 78 shows the interactions at "ear" section. This interaction defined that the "ear" surface of the sample part (in pink) moves along with the surface of the upper punch (in red). All of the interactions are defined as "Surface-to-Surface" (Explicit) type, which means the deformation of the one surface (slave surface) will be controlled by the deformation of the other (master surface). The first surface (master surface) was always the surface on the rigid bodies, while the second surface (slave surface) was the surface interacting with the die and punches on the part. This means, the powder was forced to follow the movements of the punches and was ensured a desired shape during compression. The section of the ABAQUS input file details these interactions can be found in Appendix.
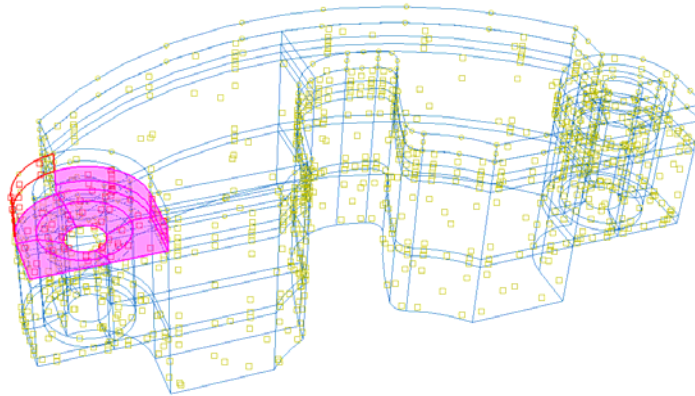
Figure 78 Defining an Interaction

Friction occurs between the powders and the surrounding die and punches. This was modeled by creating the "Interactions Properties" in ABAQUS. The friction coefficient was 0.17 according to prior research (Kwon et al. 1997, Coube and Riedel 2000). The property function was called by the "Interactions" while ABAQUS couples the corresponding surfaces.

The die was fixed during the simulation while various movements were imposed on the punches in order to simulate the actual pressing. Boundary conditions caused by the movements were defined by the boundary section in the ABAQUS input file. Details are referred in Appendix B.

By applying the DCP parameters described in Chapter 3 plus the values of R and α predicted from the proposed method based on the ring sample in Chapter 3, the finite

element analysis was done. The hardening law defined in section 3.4 was adopted. A summary of the parameters can be found.

Table 12 DCP Parameters

Young's modulus	12 GPa at 3.2 g/cm^3, 200 GPa at 7.2 g/cm^3.
Poisson's ratio	0.29
Material cohesion	26.2 MPa
Angle of friction	77.1°
Eccentricity parameter	0.88
Transition parameter	0.09
Initial volumetric inelastic-strain-hardening	0.01
K	1.0

An explicit, dynamic analysis is computationally efficient for the analysis of large models with relatively short dynamic response times. This type of analysis allows the definition of general contact conditions and allows a consistent large-deformation. To run a dynamic explicit analysis, "step" configurations need to be set. This includes the time period for the step, the maximum time increment, the increment size, mass scaling definitions, and bulk viscosity parameters.

Bulk viscosity introduces damping associated with volumetric straining. In ABAQUS/Explicit, a small amount of damping is introduced in the form of bulk viscosity to control high frequency oscillations. It improves the modeling of high-speed

dynamic events (ABAQUS 2003). ABAQUS/Explicit contains two types of bulk

viscosity: linear and quadratic. Linear bulk viscosity is introduced by default in an

ABAQUS/Explicit analysis. It generates a bulk viscosity pressure that is linear in the

volumetric strain rate. Quadratic bulk viscosity parameter is found only in solid

continuum element and only if the volumetric strain rate is compressive. For the ferrous

powders used in this research, the linear bulk viscosity parameter was set to 0.2 and the

quadratic bulk viscosity parameter was set to 1.2 according to the DEFORM-3D user's

manual (DEFORM-3D 2003). More details can be found in ABAQUS user's manual and

DEFORM-3D user's manual.

Mass scaling is often used in ABAQUS/Explicit for computational efficiency. To

achieve an economical solution, it is helpful to increase the mass of the model artificially,

which is called "mass scaling". During the calculation of this analysis, elements near the

compact zone experience a large deformation. The reduced characteristic lengths of these

elements result in a smaller global time increment. Scaling the mass of these elements

throughout the simulation can significantly decrease the computation time. In this

simulation, this parameter was defined as 100000 to reduce the computational time from

8 hours to 20 minutes. The overall PEQC (plastic strain) results were examined to be

identical when the mass scaling parameter equals to 1 and when the scaling parameter

equals to 1000000. The following picture presents the PEQC distribution from the FEA

with the initial shape and deformation of the powders.
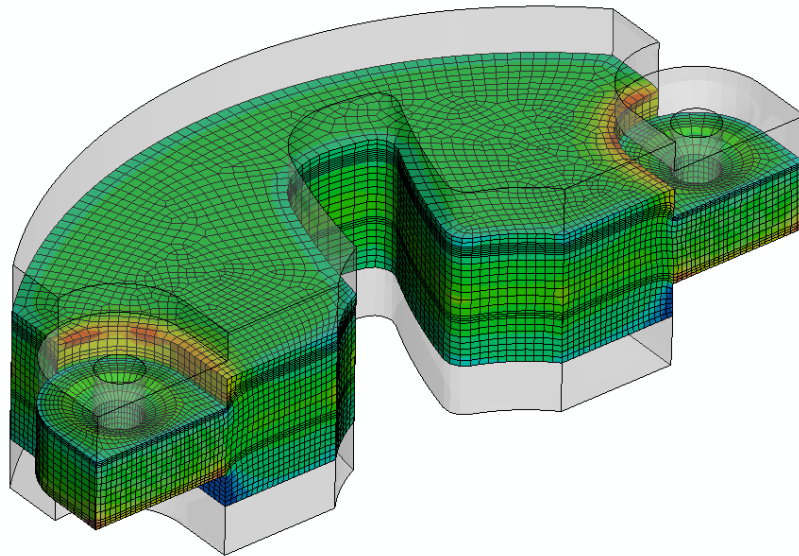
Figure 79 Overall PEQC Distribution, Verification

The elements adjacent to the edges were excluded in the generation of the simulated density map for the correlation to the actual density map since the local density inside this area could not be measured with enough accuracy due to the physical deflection of the part. This was detailed in the previous chapter.

The following simulated density map was compared to the actual density map. The PEQC value of each element inside the areas was read by a MatLab program for plotting and further comparison purposes. The simulated density map is plotted below.
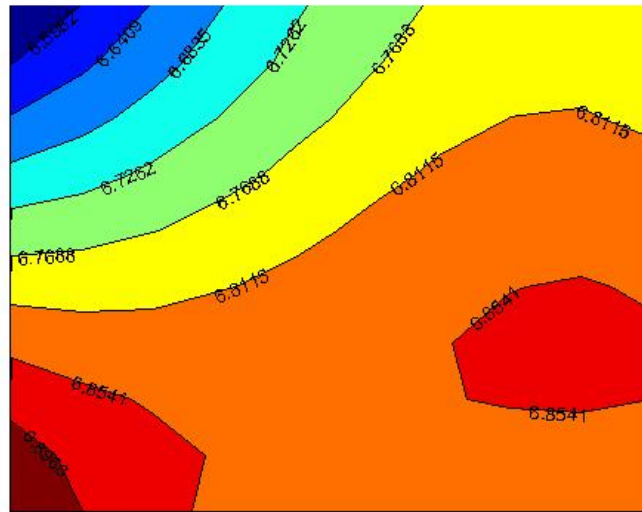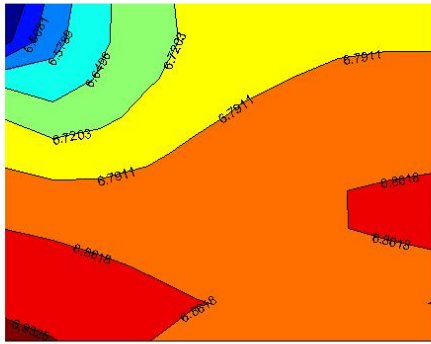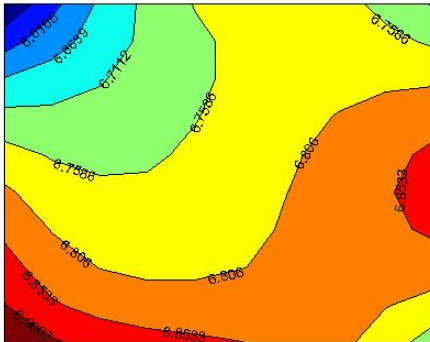
Figure 80 Simulated Density Map, Verification

4.5   Comparison of Density Maps

The actual density map was obtained by the simplePCI photos while the simulated

density maps were created by the finite element analysis using the values of R and α from

the ring compact using the proposed numerical optimization method. A MatLab program

was written to compute the correlation coefficients between the actual and simulated

density maps for all three zones respectively. The program read the local density map

data from the image analysis process then applied a 4th order polynomial regression to

represent the actual density map. The FEA density map data was also read by the

program and was fitted in a 4th order polynomial model. The local density information

from both density maps was compared side by side at the corresponding locations. As

described in Chapter 3, the correlation coefficient between two vectors can be calculated.

Table 13 Density Map Comparison

Density Map		C.C.
FEA map		61.19%
Measured map		

The comparison zone has 100 photos in an arrangement of 10 x 10 (covered area is 5 mm x 6.25 mm, or 0.2 in x 0.25 in) for the comparison. The correlation coefficient was found as 0.61.

The similarity on this multi-stage compact between the simulated density map and the measured density map appears lower than the one on the ring specimen described in Chapter 3. Some possible reasons can be classified below:

1. The more complex geometry created difficulties to measure the local density map precisely;

2. The larger measured metal surface made it more difficult to control a consistent contrast of images. This may distort the measured density map;

3. The specimen presented less delicate edges due to the more complex production procedure (multi compression rates, etc.) and the absence of pre-sintering. This damaged the accuracy of measurement at edge and corner areas where a steeper density gradient often occurs.

4. The multi-stage geometry leveraged the lack of accurate estimation of friction forces during compaction. This may produce poorly defined boundary conditions for the finite element analysis, consequently, leads to a inaccurate simulation density map;

In conclusion, the proposed method predicted the cap eccentricity parameter R and the transition parameter α using a near cylindrical green compact with a simple geometry. The predicted parameters were applied to a multistage specimen with a more complex geometry. The measured density map and the simulated density map were compared to obtain the similarity. The comparison presented an acceptable result; the correlation coefficient was computed as 0.61.

Chapter 5   CONCLUSIONS AND CONTRIBUTIONS

5.1   Conclusions

A universal calibration method was proposed to determine the Drucker-Prager cap model parameters for the density/strength distribution prediction for uniaxial compacted metal powders. This method combines an image analysis technique, the finite element method, and a numerical optimization algorithm. This method is also distinguished from current Drucker-Prager cap model calibration methods through the elimination of the expensive and hard-to-access triaxial compression test for hard metal powders.

The essential objective of this research is to establish a more feasible Drucker-Prager cap model calibration procedure. To do so, a near cylindrical pressed green compact was utilized. The actual local density map of this compact was measured. The map was then compared to a simulated density map by the numerical simulation with an initial parameter guess. A numerical optimization algorithm was applied. The function of this algorithm is to select new cap model parameters according to the density map comparison. Another numerical simulation was conducted to generate a new simulated density map using the new generated cap parameters. The process iterated until the optimized parameters delivering the highest similarity between the actual maps and FEA map were achieved. By this means, the expensive triaxial compression test was eliminated and only common material test techniques and equipments were needed for

the new calibration method. Commercial software packages, ABAQUS and HyperStudy, and in-house programs were utilized to create the framework of this automated procedure.

In this research two of the Drucker-Prager cap model parameters, the cap eccentricity parameter R, which defines the cap shape, and the transition parameter α, which defines the transition surface, were determined by the proposed calibration method using a cylindrical ferrous-based green part produced in the working condition by powder compaction. The value of R determined by the proposed method is 0.88. It is close to values of iron-based powders in literature, which are in the range of 0.74 to 0.87 (Coube and Riedel 2000). The predicted value of α is 0.09, which is greater than the common selection of 0.01 to 0.05 (He et al. 2001; Lee and Kim 2002, Wagle et al. 2003, ABAQUS 2003; Gunningham et al. 2004;). The larger value of α implies that the transition between powder shear and plastic deformation in the cap may play a larger role in densification modeling than recorded by previous research. This agrees with what Simo et al. (Simo et al. 1985) and Zeuch et al. (Zeuch et al. 2001) concluded.

The FEA density map using the predicted parameters presented a similarity to the measured density map by showing a correlation coefficient of 77.91% on the cylindrical compact. The predicted parameters were applied to a more complex multistage compact to validate the independency of the proposed method to an arbitrary geometry. The density map comparison was carried out and the correlation coefficient was calculated as 61.19%. The lower correlation coefficient indicates improvement is needed in either the

measurement of an accurate local density map or the numerical simulation of powder compaction on a more complicated geometry.

5.2   Contributions

This research created a novel universal standard procedure to calibrate the Drucker-Prager cap model for prediction of the density distribution of a green compact formed by metal powder compaction. This new method is distinguished from current methods by replacing the triaxial compression test with numerical simulation and optimization methods and common material tests. This is the most significant contribution of this research. By removing the triaxial test from the experiment list, the DPC parameter determination will be faster and less expensive and in turn, it will make the finite element analysis using a Drucker-Prager cap model in the P/M industry much easier and more common.

This research established a standard procedure for estimating the cap shape parameter R, one of the most important DPC parameters. This work is expandable. Although starting with R and α, this "reverse engineering" procedure may be expanded to include other Dracker-Prager cap model parameters. Therefore, a DPC model will be calibrated numerically to save the time and cost caused by experimental work. The prediction accuracy improvement by reducing operator error is another benefit of the new numerical calibration procedure.

5.3   Future Work

Some promising topics related to this research were recognized. These topics will improve the proposed DPC calibration method, sequentially, improve the accuracy of the numerical simulation of powder compaction.

5.3.1   Local Density Measurement

The proposed method compares the actual density map with simulated density maps to determine the Drucker-Prager cap model parameters. How to obtain an accurate measurement of the local density is fundamental.

Although more advanced tomography methods, such as X-ray CT, ultrasonic, and Electrons, are available, the traditional image analysis method is still a common way to measure the local density of metal compacts by taking the photos by an optical telescope. The benefit of this method is the simplicity and the low cost. Due to the high porosity and the relatively large size of the ferrous specimen applied in this research, the cost of the more advanced methods will be expansive. For instance, a computed tomography (CT) system with the capability to capture photos of a ferrous compact needs a 225 KV to 450 KV X-ray source, and costs from 1.5 million to 3 million dollars, while the service charge for taking pictures only could be thousands of dollars (by communicating with BIR service engineers, http://www.bio-imaging.com, September 2008).

It was found that consistency of contrast of the photos plays a crucial role in local density determination. The reason is the local density is calculated based on the ratio of solid pixels (white) to void pixels (black) in a photo. While relatively simple in application, this procedure can distort results if used inconsistently between measurements. In this research, before a photo was taking, the contrast was re-calibrated for a consistent contrast among these photos.

An alternative to the image analysis method to measure the local density is the surface hardness method. Previous researches reported the correlation between surface hardness, including Vickers hardness (Guillot et al. 1995, Kim et al. 2002) and Rockwell hardness (Lee and Kim, 2002), and the local density. The basic concept of this method is to divide a surface into small areas, measure the surface hardness in these areas then convert the hardness to local density based upon a relationship for the certain material. To do so, different locations inside one small area need to be measured and the average surface hardness will be applied.

Comparing to the image analysis method, the surface hardness method has two potential issues. The first issue is, when the testing probe stands on a void area in the surface, it is measuring the out-of-plane surface hardness and the void is not properly represented. Thus the local density could be distorted. For a porous material, this scenario could happen frequently. The second issue of the surface hardness method is that the establishment of the function mentioned above will be extra work for each material

whose DPC parameters need to be predicted. This requires an extensive experimental work in practice.

X-ray CT is becoming more popular for local density measurement despite the expensive cost. The CT method provides a 3D microstructure characterization of the sample. The advantage of this technique is obvious: it is a nondestructive estimation; it eliminates the artifacts due to specimen preparation; it is precise if a good calibration is made, etc.
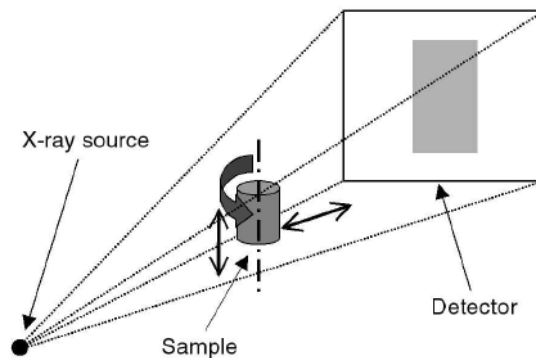
Figure 81 Principle of X-ray CT Method

The principle of the X-ray CT method is illustrated in Fatigue 81. The specimen is placed on a precision turntable in a divergent bean of X-ray and rotates in an angular increment. A detector is utilized to scan the local intensity distribution of a diverging X-ray bean transmitted through the sample. The scanned data is used to reconstruct, also known as a tomogram, a 3D representation of the sample by using the Beer-Lambert law of absorption (Burch, 2002, Sinka et al., 2004). According to the Beer-Lambert law, the dependence of the intensity $I(t)$ of the X-ray beam after its crossing through a layer of homogeneous material of thickness t is related to the initial intensity I_0 and the linear attenuation coefficient μ through

$$I(t) = I = I_0 e^{-\mu t} \text{ or } -\ln\left(\frac{I}{I_0}\right) = \mu t \qquad \text{Equation 38}$$

where µ is a local coefficient which characterizes the material,

$$\mu = \rho_i \left(\frac{\mu_{i0}}{\rho_{i0}}\right) \qquad \text{Equation 39}$$

Where ρ is the real local density of material, is μ_0 the normal absorption coefficient, and is ρ_0 the normal density. When material compounds are mixed, Equation 39 can be written as

$$\mu = \sum_i \rho_i \left(\frac{\mu_{i0}}{\rho_{i0}}\right) \qquad \text{Equation 40}$$

This leads to the general Beer-Lambert law for X-ray beam

$$\ln\left(\frac{I}{I_0}\right) = -\int \mu(l) dl \qquad \text{Equation 41}$$

where dl is the infinitesimal length along the trajectory of X-ray beam in the material, and the summation runs over the whole path.

When X-ray beam is non-monochromatic, the result will be distorted. Since the coefficients μ_{i0} depend on X-ray wavelength λ and a sum of exponentials is not an exponential. This is called the beam hardening effect and is the most common artifact of the X-ray CT method. The X-ray tomography technique generates additional artifacts, such as the ring artifacts due to the sample rotation, and pronounced edges and false density gradients due to the reconstruction process. The distortions can be partially corrected using mathematical algorithms (Miguelez-Moran et. al. 2009).

In summary, various methods are available to measure the local density for a green compact. Besides the image analysis method, the surface hardness method is also straightforward, less expensive, and only requires common laboratory equipments. Although some issues exist, it is still a promising topic to do a further investigation.

5.3.2 Estimation of Friction Forces

To simulate the density distribution in a green compact precisely, friction forces between powders and tools, including dies and punches, must be defined correctly. Friction forces contribute considerably to the powder compaction procedure. At some particular areas, for instance, edges and corners, the friction force could dominate the powder density behavior.

To quantify friction forces during powder compaction is difficult. In most recent researches, the friction force coefficient is taken into account as a constant during the compaction (Kwon et al. 1997, He et al. 2001; Lee and Kim 2002, Wagle et al. 2003). The actual friction forces are controlled by various factors, such as the compression force, the local density of powders, the geometry of the green part, the use of lubricant, and temperature, etc. Most of these parameters vary during the compaction process. As a consequence, the friction forces will change time to time as well.

Kwon et al. adopted a numerical trial-and-error method to determine the friction coefficient for 316L stainless steel powders (Kwon et al. 1997). They compared the

actual density map of a green compact by unaxial compression to FEA density maps. No general formula between friction forces and compaction parameters has been formulated.

Experimental methods also have been recorded in literature (Mallender et al. 1972, Tabata et al. 1981, Ernst et al. 1991, Gethin et al. 1994). This kind of methods utilizes proper apparatus to measure the friction force when powders are compressed in dies. In general, a simple cylindrical part was applied. A schematic section view to measure the friction force can be found below. The stress imbalance between the top and bottom of the compact is caused by the presence of friction. Gethin et al. (Gethin et al. 1994) measured friction coefficients for different settings of powder compaction, including compact length, compaction ratio, etc., on four particular powders, iron powder mix, bronze powder mix, ceramic powder mix, and carbon powder mix. The experimental setup is illustrated in Figure 82, while some of the results are listed in Table 14. As mentioned, a cylindrical sample is utilized in this method. So, how to apply this method to a complex geometry needs further studies.
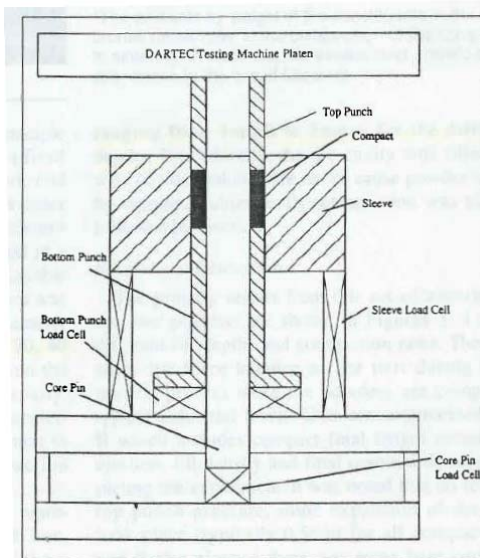
Figure 82 Schematic Section View to Measure Friction

Table 14 Friction Coefficients Measured by Gethin et al.

Table II. Powder Compact Length, Fill and Final Density				
	Final Compact Length (mm)	Fill Relative Density	Final Relative Density	Wall Friction
Fill Depth 20mm				
Iron	9.87	0.403	0.817	0.08
Bronze	10.07	0.383	0.761	0.10
Ceramic	7.76	0.238	0.615	0.18
Carbon	8.85	0.425	0.961	0.25
Fill Depth 80mm				
Iron	40.09	0.383	0.764	0.12
Bronze	37.47	0.345	0.736	0.10
Ceramic	34.68	0.237	0.546	0.18
Carbon	38.57	0.433	0.897	0.20

The latter method requires extensive laboratory work but produce a function describing friction forces during powder compaction process. It will give more confidence to powder compaction simulation if friction forces can be accurately predicted during powder compaction procedure.

5.3.3 Transition Surface Parameter, α

Currently, regardless of materials, it is common to select a small value for the transition surface parameter, α, from the range of 0.01 to 0.05 during building up the Drager-Prager cap model (He et al. 2001; Lee and Kim 2002, ABAQUS 2003; Wagle et al. 2003 , Gunningham et al. 2004) although researches (Simo et al. 1985) indicated that this space might not define this parameter well and larger α was determined by experiments (Zeuch et al. 2001). The majority of researches on this parameter have been focusing on how to retrieve a smoother transition surface between the shear failure surface and the cap surface in respect of computational algorithms, while the study of the

physical mechanism of this parameter is hard to find in literature. How this transition surface corresponds to the three compaction stages is still not fully understood.

The transition surface parameter of an iron-based powder was determined as 0.09 in this research. This supports the ideas that the physical meaning of α is necessary to draw attentions. Further investigations will correlate this parameter to the physical phenomena during the powder compaction in order to understand the procedure better, and will build up more precise constitutive models applied to powder metallurgy industry.

BIBLIOGRAPHY

ABAQUS. (2003). *User's manual (Version 6.4)*.

Aravas, N. (1987). "On the Numerical Integration of a Class of Pressure-Dependent Plasticity Models." *International Journal for Numerical Methods in Engineering*, 24, 1395-1416.

ASTM. (2001). Standard C1198-01, Standard Test Method for Dynamic Young's Modulus, Shear Modulus, and Poisson's Ratio for Advanced Ceramics by Sonic Resonance.

ASTM (2001), Standard E11-01, Standard Specification for Wire Cloth and Sieves for Testing Purposes.

ASTM. (2003). "Standard D2850-03a, Standard Test Method for Unconsolidated-Undrained Triaxial Compression Test on Cohesive Soils."

ASTM. (2004). "Designation: D3967-95a, Standard test method for splitting tensile strength of intact rock core specimens."

ASTM. (2008). "B922 - 02(2008) Standard Test Method for Metal Powder Specific Surface Area by Physical Adsorption."

Aydin, I., Briscoe, B. J., and Sanliturk, K. Y. (1996). "The Internal Form of Compacted Ceramic Components: a Comparison of Finite Element Modelling with Experiments." *Powder Tech.*, 89(3), 239-54.

Bažant, Z. P., (1985), Mechanics of Geomaterials, Rocks, Concrete, Soils, John Wiley & Sons Ltd.

Box, G. E. P., and Wilson, K. B. (1951). "On the Experimental Attainment of Optimum Conditions." *Journal of the Royal Statistical Society*, B13, 1-45.

Brown, S., and Abou-Chedid, G. (1993). "Evaluation of yield functions due to powder characteristics." *Advances in Powder Metallurgy and Particulate Materials(3),* 245-255.

Brunauer, S., Emmett, P. H., and Teller, E. (1938), "Adsorption of Gases in Multimolecular Layers", *Journal of the American Chemical Society*, 60, 309.

Burch, S. (2002), "Measurement of Density Variations in Compacted Parts Using X-ray Computerised Tomography", MPR, 24-28.

Chtourou, H., Guillot, M., and Gakwaya, A. (2002). "Modeling of the Metal Powder Compaction Process Using the Cap Model. Part I." *International Journal of Solids and Structures*, 1059-1075.

Coube, O., and Riedel, H. (2000). "Numerical Simulation of Metal Powder Die Compaction with Special Consideration of Cracking." *Powder Metallurgy*, 43, 123 - 131.

Crawford, J., and Lindskog, P. (1983). "Constitutive Equations and Their Role in the Modeling of the Cold Pressing Process." *Scandinavian Journal of Metallurgy*(12), 271-281.

Cunningham, J. C., Sinka, I. C., and Zavaliangos, A. (2004). "Analysis of Tablet Compaction. I. Characterization of Mechanical Behavior of Powder and Powder/Tooling Friction." *Journal of Pharmaceutical Sciences*, 93(8), 2022-2039.

Dean, A, Voss D. (1999), *Design and Analysis of Experiments*, Springer-Verlag New York Inc.

DEFORM-3D (2003). *User's manual (Version 8.0)*

Donachie, M. J., and Burr, M. F. (1963). "Effects of Pressing on Metal Powders." *Journal of Metallurgy*, 15(2), 849-854.

Doremus, P., Geindrean, C., Martin, A., Debove, L., Lecot, R., and Dao, M. (1995). "High Pressure Triaxial Cell for Metal Powder." *Powder Metallurgy*, 38(44), 284-287.

Drucker, D. C. and Prager, W. (1952). "Soild mechanics and plastic analysis for limit design." *Quarterly of Applied Mathematics*, 10(2), 157-165.

Drucker, D.C., Gibson, R.E. and Henkel, D.J. (1957), "Soil Mechanics and Work hardening Theories of Plasticity." *Transactions, ASCE*, 122, 338-346.

Ernst, E., Thummler, F, Beiss, P, Wahlung, R., and Arnhold, V (1991). "Friction measurements during powder compaction." *Powder Metallurgy International*, 22, 77.

Fischmeister, H. F., and Arzt, E. (1983). "Densification of Powders by Particle Deformation." *Powder Metallurgy*, 26(2), 82-88.

Fischmeister, H. F., Arzt, E., and Olsson, L. R. (1978). "Particle Deformation and Sliding During Compaction of Spherical Powders: a Study by Quantitative Metallography." *Powder Metal.*, 21, 179.

Fleck, N. A., Kuhn, L. T., and McMeeking, R. M. (1992). "Yielding of metal powder bounded by isolated contacts." *Journal of the Mechanics and Physics of Solids*, 40(5), 1139-1162.

German, R. M. (1997). *Powder Metallurgy Science (Second Edition)*, Metal Powder Industries Federation.

Gethin, D. T., Tran, V. D., Lewis, R. W., and Ariffin, A. K. (1994). "An investigation of powder compaction process." *The International Journal of Powder Metallurgy*, 30(4), 385-398.

Greenwood, A. G., Rees, L. P., and Siochi, F. C. (1998). "An Investigation of the Behavior of Simulation Response Surface." *European Journal of Operational Research*, 110, 282-313.

Groover, M. P. (2001). *Fundamentals of Modern Manufacturing (Second Edition)*, John Wiley & Sons, Inc.

Guillot, M., Chtourou, H., and Parent, S. (1995). "Local Density Measurements in Green and Sintered 316L Stainless Steel Powder Compacts." *Advances in Powder Metallurgy and Particulate Materials*(1(2)), 169-183.

Gunningham, J. C., Sinka, I. C., and Zavaliangos, A. (2004). "Analysis of Tablet Compaction. I. Characterization of Mechanical Bechavior of Powder and Powder/Toolong Friction." *Journal of Pharmaceutical Sciences*, 93(8), 2022-39

Gurson, A. L. (1977). "Continuum theory of ductile rupture by void growth: part I—yield criteria and flow rules for porous ductile media." *ASME Journal of Engineering Materials and Technology*, 99, 2-15.

Haggbald, H. A., Doremus, P., and Bouvard, D. (1996). "An International Research Program on the Mechanics. of Metal Powder Forming." *Advances In Powder Metallurgy & Particulate Materials*, 7, 178-192.

He, Y., Engel, R. S., Salamon, N. J., Lindner, S., and Lu, P. "Numerical Simulation for 316L Stainless Steel Powder Die Compaction Process." *Proceedings of the International Conference on Fine Powder Processing Forming*, University Park, PA, 153-166.

Heckel, R. W. (1961). "An Analysis of Powder Compaction Phenomenon." *Trans. Metall. Soc. AIME*, 221, 671-4.

HyperStudy. (2006). "User's manual, Version 7.0."

James, P. J. (1977). "Particle deformation during cold isostatic pressing of metal powders." *Powder Metallurgy*, 20, 21-25.

Jin, R., Chen, W., and Simpson, T. W. (2001), "Comparative Studies of Metamodeling Techniques Under Multiple Modeling Criteria", *Structural and Multidisciplinary Optimization*, 23(1), 1–13.

Joshi, S., Sherali, H. D., and Tew, J. D. (1998). "An Enhanced Response Surface Methodology (RSM) Algorithm Using Gradient Deflection and Second-order Search Strategies." *Computers and Operations Research*, 25(7), 531-541.

Kim, K. T., Choi, S. W., and Park, H. (2000). "Densification Behavior of Ceramic Powder Under Cold Compaction." *ASME Journal of Engineering Materials and Technology*, 122(2), 238-244.

Kim, H.G., Gillia, O., Doremus, P., and Bouvard, D. (2002). "Near net shape processing of a sintered alumina component: adjustment of pressing parameters through finite element simulation." *International Journal of Mechanical Sciences*, 44, 2523-2539.

Kleijnen, J. P. C., Hertog, D. D., and Angün, E. (2002). "Response Surface Methodology's Steepest Ascent and Step Size Revisited." CentER Working Paper.

Koopman, M. G., Rachakonda, V. B. S., Gurson, A. L., and McCabe, T. (1992). "Material Models for the Finite Element Simulation of Compaction of Metal Powder." TMS Fall meeting, Chiacago.

Kuhn, H. A., and Downey, C. L. (1971). "Deformation characteristics and plasticity theory of sintered powder materials." *International Journal of Powder Metallurgy*, 7(11), 15-25.

Kwon, Y. S., Chung, S. H., Sanderow, H. I., Kim, K. T., and German, R. M. "Numerical Analysis and Optimization of Die Compaction Process." *Proceedings of the 2003 International Conference on Powder Metallurgy & Particulate Materials*, 24-36.

Kwon, Y. S., Lee, H. T., and Kim, K. T. (1997). "Analysis for cold die compaction of stainless-steel powder." *ASME Journal of Engineering Materials and Technology*, 119, 366-373.

Lee, S. C., and Kim, K. T. (2002). "Densification behavior of Aluminum Alloy Powder under Cold Compaction." *International Journal of Mechanical Sciences*, 44, 1295-1308.

Lomax, R. G. (2007). *An introduction to statistical concepts (second edition)*, Lawrence Erlbaum Associates, Inc.

Mallender, R. F., Dangerfield, C. J., and Coleman, D. S. (1974). "The variation of coefficient of friction with temperature and compaction variables for iron powder stearate-lubricated system." *Powder Metallurgy*, 17, 288.

Meerman, W. C. P. M., and Knaapen, A. C. (1979). "A High-Pressure Triaxial Testing Cell." *Powder Technology*, 22, 271-278.

Meketon, S. "Optimization Simulation: A Survey of Recent Results." *Proceedings of the 1987 Winter Simulation Conference*, 58-67.

Miguelez-Moran, A. M., Wu, C.Y., Dong, H.S., and Seville, J. P.K. (2009), "Characterisation of density distributions in roller-conpacted ribbons using micro-indentation and X-ray micro-computed tomography", *European Journal of Pharmaceutics and Biopharmaceutics*, 72, 173-182

MPIF. (1998). "Standard 35, Materials Standards for P/M Self-Lubricating Bearings."

Myers, R. H., and Montgomery, D. (1995). *Response Surface Methodology: Process and Product Optimization Using Designed Experiments*, Wiley, Toronto.

Neddermeijer, H. G., Piersma, N., Oortmarssen, G. J. v., Habbema, J. D. F., and Dekker, R. (1999). "Comparison of Response Surface Methodology and the Nelder and Mead Simplex Method for Optimization in Microsimulation Models." Erasmus University, Rotterdam, The Netherlands.

Nicolai, R. P., Dekker, R., and Piersma, N. "Automated Response Surface Methodology for Stochastic Optimization Models with Unknown Variance." *Proceedings of the 2004 Winter Simulation Conference*, 491-499.

Phillips, D.H., Lannutti, J.J. (1997), "Measuring Physical Density with X-ray Computed Tomography", *NDT&E International*, 30(6), 339-350.

PM MODNET, (1999). "Comparison of Computer Models Representing Powder Compaction Process." *Powder Metallurgy*, 42(4), 301-311.

Riera, M. D., and Prado, J. M. "Modeling of Cold Compaction Process of Metal Powders." *PM94*, 685-688.

Resende, L., and Martin, J.B., (1985), Formulation of Drucker-Prager Cap Model, *Journal of Engineering Mechanics*, 111(7), 855-881.

Sacks, J., Welch, W. J., Mitchell, T. J., and Wynn, H. P. (1989), "Design and Analysis of Computer Experiments", *Statistical Science*, 4(4), 409–435

Sandler, I. S., and Rubin, D. (1979). "An Algorithm and a Modular Subroutine for the Cap Model." *International Journal for Numerical and Analytical Methods in Geomechanics*(3), 173-86.

Shima, S., and Oyane, M. (1976). "Plasticity Theory for Porous Metals." *International Journal of Mechanical Sciences*, 18, 258.

Shima, S., and Saleh, M. A. E. (1993). "Variation of Density Distribution in Compacts in Closed Die Compaction with Powder Characteristics." *Advances in Powder Metallurgy and Particulate Materials*(3), 175-189.

Simo, J. C., Ju, J. W., Pister, K. S., and Taylor, R. L. (1988). "Assessment of Cap model: Consistent Return Algorithms and Rate Dependent Extension." *ASCE Journal of Engineering Materials*, 114(2), 191-218.

Sinka, I.C., Burch, S.F., Tweed, J.H., Cunningham, J.C. (2004), "Measurement of Density Variations in Tablets Using X-ray Computed Tomography", *International Journal of Pharmaceutics*, 271(1-2), 215-224;

Sinka, I. C., Cocks, A. C. F., Morrison, C. J., and Lightfoot, A. (2000). "High pressure triaxial facility for powder compaction." *Powder Metallurgy*, 43(3), 253-262.

Spinner, S., and Tefft, W. E. (1961). "A Method for Determining Mechanical Resonance Frequencies and for Calculating Elastic Moduli from These Frequencies." *ASTM proceedings, Engineering*, 1221-1239.

Sun, X. K., Chen, S. J., Xu, J. Z., Zhen, L. D., and Kim, K. T. (1999). "Analysis of cold compaction densification behaviour of metal powders." *Materials Science and Engineering A*, 267(1), 43-49.

Tabata, T., Masaki, S. and Kamata, K. (1981). "Coeffiient of Friction Between Metal Powder and Die Wall During Compaction." *Powder Metallurgy International*, 21, 773.

Timoshenko, S. P., and Goodier, J. N. (1987). *Theory of Elasticity, Third Edition*, McGraw-Hill Book Company.

Tszeng, T.C. and Wu, T. (1995). "A study of the coefficients in yield functions modeling metal powder deformation." *Acta Materialia*, 44(9), 3543-3552

Wagle, G. S., Engel, R. S., Bollina, R., and German, R. M. (2003). "Statistical Analysis of Modified Drucker-Prager Cap Model Parameters for Applications to Modeling Die Compaction." *Proceedings of the 2003 International Conference on Powder Metallurgy & Particulate Materials*, Las Vegas, NV, 24-36.

Wang, G. G., Shan, S. (2007). "Review of Metamodeling Techniques in Support of Engineering Design Optimization", *Journal of Mechanical Design*, 129, 370-380.

Watson, T. J., and Wert, J. A. (1993). "On the Development of Constitutive Relations for Metallic Powders." *Metallurgical Transactions A*, 24A, 2071-81.

Weber, G. G., and Brown, S. B. (1989). "Simulation of the Compaction of Powder Components." *Advances in Powder Metallurgy and Particulate Materials (1)*, 105-118.

Website. (Retrieved on Jan. 14, 2005).

Website. (Retrieved on Jan. 29, 2005).

Wilcox, R. R. (2003), Applying Contemporary Statistical Techniques, Academic Press, Amsterdam, Boston, 2003.

Yu, C. J., Henry, R. J., Parthasarathi, T., and S. Jo J. "Resonant Frequency Measurements for the Determination of Elastic Properties of PM Components." *Proceedings of the P/M'92 World Congress*, San Francisco, CA, 319-32.

Zeuch, D. H., Grazier, J. M., Argüello, J. G., and Ewsuk, K. G. (2001). "Mechanical Properties and Shear Failure Surfaces for Two Alumina Powders in Triaxial Compression." *Journal of Materials Science*, 36, 2911-24.

Zipse, H. (1997). "Finite-element Simulation of the Die Pressing and Sintering of a Ceramic Component." *Journal of the European Ceramic Society*, 17, 1707 - 1713.

Appendix A Definition of Young's Modulus in ABAQUS

```fortran
      subroutine usdfld(field,statev,pnewdt,direct,t,celent,time,dtime,
1 cmname,orname,nfield,nstatv,noel,npt,layer,kspt,kstep,kinc,
2 ndi,nshr,coord,jmac,jmtyp,matlayo,laccflg)
c
       include 'aba_param.inc'
c
      character*80 cmname,orname
      character*8  flgray(15)
      dimension field(nfield),statev(nstatv),direct(3,3),t(3,3),time(2),
     * coord(*),jmac(*),jmtyp(*)
      dimension array(15),jarray(15)
c
c Get temperatures from previous increment
c     call getvrm('SOAREA',array,jarray,flgray,jrcd,
      call getvrm('PEQC',array,jarray,flgray,jrcd,
c     call getvrm('E',array,jarray,flgray,jrcd,
     $    jmac, jmtyp, matlayo, laccflg)

      field(1) = abs(array(4))
         statev(1) = field(1)
c     field(1) = abs(array(2))

c     open (2, FILE = "c:\temp\out.out", status = 'OLD',
c    * ACCESS = 'APPEND')

c        write (2,*) "PEQC(2) = ", field(1)
c        write (2,*) "E(2) = ", array(2)
c        write (2,*) "E(1) = ", array(1), " E(2) = ", array(2),
c    $  "E(3) = ", array(3)
c        close(2)

c        write (2,*) "E = ", field(1)
c        close(2)

      return
      end
```

Appendix B Definition of Surface Interactions in ABAQUS

```
**
**  INTERACTIONS
**
** Interaction: pd-hole-01
*Contact Pair, interaction=friction, mechanical
constraint=KINEMATIC, weight=1., small sliding, cpset=pd-hole-01
die-hole-01, powder-hole-01
** Interaction: pd-hole-02
*Contact Pair, interaction=friction, mechanical
constraint=KINEMATIC, weight=1., small sliding, cpset=pd-hole-02
die-hole-02, powder-hole-02
** Interaction: pd-side-01
*Contact Pair, interaction=friction, mechanical
constraint=KINEMATIC, weight=1., small sliding, cpset=pd-side-01
die-side, powder-side
** Interaction: pl-01
*Contact Pair, interaction=friction, mechanical
constraint=KINEMATIC, weight=1., small sliding, cpset=pl-01
lP-top-01, powder-bottom-01
** Interaction: pl-02
*Contact Pair, interaction=friction, mechanical
constraint=KINEMATIC, weight=1., small sliding, cpset=pl-02
lP-top-02, powder-bottom-02
** Interaction: pl-03
*Contact Pair, interaction=friction, mechanical
constraint=KINEMATIC, weight=1., small sliding, cpset=pl-03
lP-top-03, powder-bottom-03
** Interaction: pu-01
*Contact Pair, interaction=friction, mechanical
constraint=KINEMATIC, weight=1., small sliding, cpset=pu-01
uP-bottom-01, powder-top-01
** Interaction: pu-02
*Contact Pair, interaction=friction, mechanical
constraint=KINEMATIC, weight=1., small sliding, cpset=pu-02
uP-bottom-02, powder-top-02
** Interaction: pu-03
*Contact Pair, interaction=friction, mechanical
constraint=KINEMATIC, weight=1., small sliding, cpset=pu-03
uP-bottom-03, powder-top-03
```

Appendix C Definition of Boundary Conditions in ABAQUS

```
** Name: fix Type: Displacement/Rotation
*Boundary
_PickedSet626, 1, 1
_PickedSet626, 2, 2
_PickedSet626, 3, 3
_PickedSet626, 4, 4
_PickedSet626, 5, 5
_PickedSet626, 6, 6
** Name: BC-6 Type: Displacement/Rotation
*Boundary
_PickedSet1059, 1, 1
_PickedSet1059, 2, 2
_PickedSet1059, 4, 4
_PickedSet1059, 5, 5
_PickedSet1059, 6, 6
** Name: BC-7 Type: Displacement/Rotation
*Boundary
_PickedSet1060, 1, 1
_PickedSet1060, 2, 2
_PickedSet1060, 3, 3
_PickedSet1060, 4, 4
_PickedSet1060, 5, 5
_PickedSet1060, 6, 6
** Name: down Type: Displacement/Rotation
*Boundary, amplitude=press
_PickedSet625, 1, 1
_PickedSet625, 2, 2
_PickedSet625, 3, 3, -0.128
_PickedSet625, 4, 4
_PickedSet625, 5, 5
_PickedSet625, 6, 6
** Name: up1 Type: Displacement/Rotation
*Boundary, amplitude=press
_PickedSet627, 1, 1
_PickedSet627, 2, 2
_PickedSet627, 3, 3, 0.145
_PickedSet627, 4, 4
_PickedSet627, 5, 5
_PickedSet627, 6, 6
** Name: up2 Type: Displacement/Rotation
*Boundary, amplitude=press
_PickedSet1025, 1, 1
_PickedSet1025, 2, 2
_PickedSet1025, 3, 3
_PickedSet1025, 4, 4
_PickedSet1025, 5, 5
_PickedSet1025, 6, 6
** Name: up3 Type: Displacement/Rotation
*Boundary, amplitude=press
_PickedSet629, 1, 1
_PickedSet629, 2, 2
_PickedSet629, 3, 3
_PickedSet629, 4, 4
```

```
_PickedSet629, 5, 5
_PickedSet629, 6, 6
```

Appendix D HyperStudy Input File

Altair HyperStudy v7.0-100

Study : Study_1

```
*Id(HyperStudy v7.0-100)

*BeginStudy( s_1, "Study_1" )

    >>>>>>>>>>>>>>>>>>>>>>>>>>>>>>>>>>>>>>>>>>>>>>>>>>>>>>>>>>>>>>>>>>>>>>>>

    *BeginStudyDefinition( s_1 )

        *SetStudyDir( "C:/cong/hyperStudy" )
        *SetStudyNote( "Created on Thursday, September 21, 2006 at
11:51 AM" )


        *SetModelReference( m_1, "Model_1", TPL,
"C:/cong/hyperStudy/new_01.tpl" )
        *SetModelFile( m_1, "ringfinal.inp" )
        *SetModelRunScript( m_1, "scr_5", "" )



        *DesignVar( m_1_R, "R" , m_1.R )
        *SetDesignVarType( m_1_R, CONTINUOUS )
        *SetDesignVarRange( m_1_R, 0.1, 1.5 )
        *SetDesignVarNominalValue( m_1_R, 0.3 )

        *DesignVar( m_1_a, "a" , m_1.a )
        *SetDesignVarType( m_1_a, CONTINUOUS )
        *SetDesignVarRange( m_1_a, 0.01, 0.22 )
        *SetDesignVarNominalValue( m_1_a, 0.05 )



        *VectorSource( v_1, "Vector 1", SOLVEROUT )
        *SetVectorSource( v_1, "nom_run/ringfinal.txt", "Unknown",
"Block 2", "Column 1" )
        *VectorSource( v_2, "Vector 2", SOLVEROUT )
        *SetVectorSource( v_2, "nom_run/ringfinal.txt", "Unknown",
"Block 3", "Column 1" )


        *Response( r_1, "target")
        *SetResponse( r_1, v_1[0] )

        *Response( r_2, "constrain")
```

```
        *SetResponse( r_2, v_2[0] )


    *EndStudyDefinition()


    >>>>>>>>>>>>>>>>>>>>>>>>>>>>>>>>>>>>>>>>>>>>>>>>>>>>>>>>>>>>>>>>>>>>>

    *BeginOptimizationStudyDefinition( s_1 )

        *BeginOptimizationStudy( opt_1, "Optimization_1", SOLVER,
HYPEROPT )


            *SetDesignVarRange( m_1_R, 0.1, 1.5 )
            *SetDesignVarNominalValue( m_1_R, 0.3 )

            *SetDesignVarRange( m_1_a, 0.01, 0.22 )
            *SetDesignVarNominalValue( m_1_a, 0.05 )


            *OptConstraint( c_1, "Constraint_1", r_2, UPPER, 0.5 )
            *OptObjective( obj_1, "Objective_1", r_1, MAXIMIZE,  )
            *SetOptParameter( MAXDES, 25 )
            *SetOptParameter( GMAX, 0.5 )
            *SetOptParameter( RELOBJ, 1 )
            *SetOptParameter( ABSOBJ, 0.001 )
            *SetOptParameter( DVCONV, 0.001 )
            *SetJobManagementParam(FALSE)

            *RunOptimization()


        *EndOptimizationStudy()


    *EndOptimizationStudyDefinition()


 *EndStudy()
```